

# NAVAL POSTGRADUATE SCHOOL

## Monterey, California



## THESIS

**SIMULATIONS OF THE TJNAF FREE  
ELECTRON LASER WITH A NEGATIVE TAPER AND  
LASER DAMAGE STUDIES**

by

Adamantios Christodoulou

December 2000

Thesis Advisor:  
Co-Advisor:

William B. Colson  
Robert L. Armstead

**Approved for public release; distribution is unlimited.**

20010124 065

# REPORT DOCUMENTATION PAGE

Form Approved  
OMB No. 0704-0188

Public reporting burden for this collection of information is estimated to average 1 hour per response, including the time for reviewing instruction, searching existing data sources, gathering and maintaining the data needed, and completing and reviewing the collection of information. Send comments regarding this burden estimate or any other aspect of this collection of information, including suggestions for reducing this burden, to Washington headquarters Services, Directorate for Information Operations and Reports, 1215 Jefferson Davis Highway, Suite 1204, Arlington, VA 22202-4302, and to the Office of Management and Budget, Paperwork Reduction Project (0704-0188) Washington DC 20503.

1. AGENCY USE ONLY (Leave blank)

2. REPORT DATE

December 2000

3. REPORT TYPE AND DATES COVERED

Master's Thesis

4. TITLE AND SUBTITLE

Simulations of the TJNAF Free Electron Laser with a Negative Taper and Laser Damage Studies

5. FUNDING NUMBERS

6. AUTHOR(S)

Christodoulou, Adamantios

7. PERFORMING ORGANIZATION NAME(S) AND ADDRESS(ES)

Naval Postgraduate School  
Monterey, CA 93943-5000

8. PERFORMING ORGANIZATION REPORT NUMBER

9. SPONSORING / MONITORING AGENCY NAME(S) AND ADDRESS(ES)

10. SPONSORING / MONITORING AGENCY REPORT NUMBER

11. SUPPLEMENTARY NOTES

The views expressed in this thesis are those of the author and do not reflect the official policy or position of the Department of Defense or the U.S. Government.

12a. DISTRIBUTION / AVAILABILITY STATEMENT

Approved for public release; distribution is unlimited.

12b. DISTRIBUTION CODE

13. ABSTRACT (maximum 200 words)

The Free Electron Laser (FEL) is a candidate for a future close-in weapon system that will provide a longer protective range for missile destruction. The FEL is also tunable to wavelengths that would give good atmospheric transmission and optimal target absorption characteristics at the target. This thesis describes single-mode and multimode simulation results of the Thomas Jefferson National Accelerator Facility (TJNAF) FEL operating at far infrared wavelengths. The TJNAF FEL uses inverse tapering and is driven by 34.5 MeV and 47.5 MeV energy electron pulses. Steady-state power, weak-field steady state gain, electron beam energy spread and optical spectrum widths were explored as a function of the desynchronism and tapering rate. The simulations described FEL pulse evolution and short pulse effects. The simulation results have been presented at an International Conference held at Duke University, Durham, NC in August 2000. In addition, the results of damage to Slip-cast Fused Silica samples by the TJNAF FEL, with and without the effect of airflow are analyzed. A comparison with older damage experiments was done in order to develop scaling rules in the future.

14. SUBJECT TERMS

Free Electron Laser, Undulator, Negative Taper, Close-in Weapon Systems

15. NUMBER OF PAGES

114

16. PRICE CODE

17. SECURITY CLASSIFICATION OF REPORT

Unclassified

18. SECURITY CLASSIFICATION OF THIS PAGE

Unclassified

19. SECURITY CLASSIFICATION OF ABSTRACT

Unclassified

20. LIMITATION OF ABSTRACT

UL

**THIS PAGE INTENTIONALLY LEFT BLANK**

Approved for public release; distribution is unlimited

**SIMULATIONS OF THE TJNAF FREE ELECTRON LASER WITH A  
NEGATIVE TAPER AND LASER DAMAGE STUDIES**

Adamantios Christodoulou  
Lieutenant, Hellenic Navy  
B.S., Hellenic Naval Academy, 1990

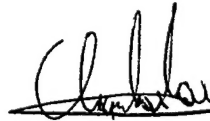
Submitted in partial fulfillment of the  
requirements for the degree of

**MASTER OF SCIENCE IN APPLIED PHYSICS**

from the

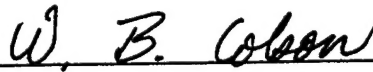
**NAVAL POSTGRADUATE SCHOOL  
December 2000**

Author:

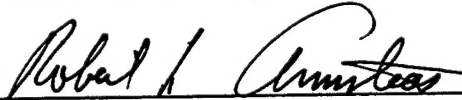


Adamantios Christodoulou

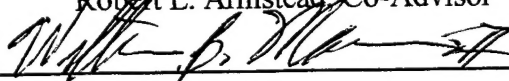
Approved by:



William B. Colson, Thesis Advisor



Robert L. Armstead, Co-Advisor



William Maier, Chairman  
Department of Physics



**THIS PAGE INTENTIONALLY LEFT BLANK**

## ABSTRACT

The Free Electron Laser (FEL) is a candidate for a future close-in weapon system that will provide a longer protective range for missile destruction. The FEL is also tunable to wavelengths that would give good atmospheric transmission and optimal target absorption characteristics at the target. This thesis describes single-mode and multimode simulation results of the Thomas Jefferson National Accelerator Facility (TJNAF) FEL operating at far infrared wavelengths. The TJNAF FEL uses inverse tapering and is driven by 34.5 MeV and 47.5 MeV energy electron pulses. Steady-state power, weak-field steady state gain, electron beam energy spread and optical spectrum widths were explored as a function of the desynchronism and tapering rate. The simulations described FEL pulse evolution and short pulse effects. The simulation results have been presented at an International Conference held at Duke University, Durham, NC in August 2000. In addition, the results of damage to Slip-cast Fused Silica samples by the TJNAF FEL, with and without the effect of airflow are analyzed. A comparison with older damage experiments was done in order to develop scaling rules in the future.

**THIS PAGE INTENTIONALLY LEFT BLANK**

## TABLE OF CONTENTS

I. INTRODUCTION.....	1
A. THE PHALANX CLOSE IN WEAPON SYSTEM.....	2
1. Description.....	2
2. Phalanx Simulations.....	3
B. HIGH ENERGY LASERS .....	7
C. THE FREE ELECTRON LASER.....	9
D. PURPOSE OF THIS THESIS .....	11
II. THE FREE ELECTRON LASER THEORY.....	13
A. THE PENDULUM EQUATION.....	13
B. THE WAVE EQUATION.....	17
C. THE FEL PHASE-SPACE EVOLUTION .....	20
D. THE TAPERED UNDULATOR.....	23
E. THE SHORT PULSE EVOLUTION .....	29
F. THE TRAPPED PARTICLE INSTABILITY .....	33
G. LIMIT CYCLE BEHAVIOR .....	34
III. THE TJNAF FEL SIMULATIONS .....	37
A. INTRODUCTION.....	37
B. SINGLE MODE SIMULATION RESULTS.....	40
C. MULTI MODE SIMULATION RESULTS.....	44
1. TJNAF FEL Simulation Results Using 34.5 MeV Energy Electron Pulses .....	45
2. TJNAF FEL Simulation Results Using 47.5 MeV Energy Electron Pulses .....	59
IV. LASER PROPAGATION IN ATMOSPHERE AND INTERACTION WITH MATTER.....	69
A. ATMOSPHERIC COMPONENTS .....	69
B. ATMOSPHERIC TRANSMISSION.....	69
C. THERMAL DIFFUSION LENGTH .....	72
D. SCALING.....	73
V. FEL DAMAGE EXPERIMENTS .....	75
A. EXPERIMENTAL PROCEDURE.....	75
B. DESCRIPTION OF RESULTS.....	76
1. Slip-cast Fused Silica Sample #1 .....	76
2. Slip-cast Fused Silica Sample #2 .....	78
3. Slip-cast Fused Silica Sample #3 .....	82
VI. CONCLUSIONS .....	89
LIST OF REFERENCES.....	93
INITIAL DISTRIBUTION LIST .....	95

**THIS PAGE INTENTIONALLY LEFT BLANK**

## LIST OF SYMBOLS

$\vec{A}$	Vector potential
$a$	Dimensionless optical field
$\vec{B}$	Undulator magnetic field
$\vec{B}_s$	Magnetic optical field
$\vec{\beta}$	Dimensionless electron relativistic velocity
$c$	Speed of light
$C$	Specific heat
$\gamma$	Lorentz factor
$d$	Desynchronism
$D$	Diffusion length
$\Delta v$	Dimensionless optical spectrum width
$\Delta\gamma/\gamma$	Fractional induced electron energy spread
$\delta$	Tapering rate (torque)
$\delta\zeta$	Standard deviation of fluctuations in initial electron phases
$\Delta v_e$	Electron spectrum width
$\vec{E}_s$	Electric optical field
$e$	Electron charge
$\varepsilon$	Absorption coefficient
$F$	Thermal conductivity
$f(v,n)$	Electron distribution
$G$	Gain
$G(v)$	Gain spectrum
$G(n)$	Gain developed over number of passes
$j$	Dimensionless current
$\vec{J}$	Current density
$\zeta$	Electron phase
$\eta$	Efficiency
$K$	Undulator parameter
$k$	Optical wave number
$k_0$	Undulator wave number
$L$	Undulator length
$\lambda$	Optical wavelength
$\lambda_0$	Undulator wavelength
$m$	Electron mass
$\mu$	Extinction coefficient
$N$	Number of undulator periods
$n$	Number of passes
$v$	Dimensionless electron phase velocity
$v_s$	Sideband frequency

$\nu_0$	Initial electron phase velocity
$\xi$	Scattering coefficient
$P$	Total optical power
$P(\nu, n)$	Optical power spectrum
$\rho_{FS}$	Material density
$\rho$	Electron density
$Q$	Quality factor
$R$	Radius
$S$	Distance between resonator mirrors
$\sigma_G, \sigma$	Gaussian velocity spread
$\sigma_z$	Pulse length
$T$	Atmospheric transmittance
$t_D$	Diffusion time
$T$	Temperature
$t$	Time
$\tau$	Dimensionless time
$V$	Volume
$\phi$	Optical phase angle
$\omega$	Optical angular frequency
$\omega_0$	Undulator angular frequency
$\Phi$	Radiation flux

## EXECUTIVE SUMMARY

Anti-ship missiles (ASM) continue to proliferate and the number of missiles that come to production using highly sophisticated technology has increased dramatically. In Chapter I, through a series of Phalanx simulations, I show that even though a hard kill is achieved, the distance is too short to survive the missile debris that finally hits the ship causing severe damage. Thus, we came to the conclusion that the current close-in weapon systems (CIWS) are inadequate and new means are required to face effectively the modern ASM threat.

A high-energy laser CIWS might be a solution because it provides an almost instantaneous reaction at the speed of light and a large missile destruction range, rapid re-engagement, a large and renewable magazine, line of sight accuracy, precision aim pointing and single shot cost-effectiveness. The Free Electron Laser (FEL) is also a candidate for CIWS, because it is tunable to various wavelengths. The FEL can be tuned to a wavelength that would give good atmospheric transmission, or is appropriate to specific target absorption characteristics.

In Chapter II the FEL theory used in this thesis is reviewed in detail. This theory includes the pendulum and wave equation derivations, the phase-space evolution, undulator tapering, short pulse evolution, and short pulse effects such as the trapped-particle instability and limit-cycle behavior.

Chapter III presents new single mode and multimode simulation results of the TJNAF FEL operation at far infrared wavelengths, using inverse tapering and driven by 34.5 and 47.5 MeV energy electron pulses. Steady-state power, weak-field steady-state gain, electron energy spread and optical spectrum width were determined as a function of



the desynchronism  $d$  and tapering rate  $\delta$ , using FEL pulse evolution simulations and short pulse effects described in detail for each case. These results are new.

In Chapter IV, laser propagation through the atmosphere was reviewed showing that laser transmission is highly dependent on wavelength. Then, we describe the thermal diffusion length and showed that in order to minimize thermal diffusion and damage sample materials, the laser spot size on the target must have diameter larger than the thermal diffusion length.

Chapter V presents the experimental procedure and the results of irradiations induced on Slip-Cast Fused Silica samples, with or without the presence of airflow. A comparison with older experiments was done in order to develop scaling rules in the future. The first sample analyzed was irradiated at a wavelength  $\lambda = 3.10 \mu\text{m}$  with pulse repetition frequency (PRF) of 18.7 MHz, an average power of 105 W, with an average flux intensity of  $490 \text{ W/cm}^2$ . The second sample analyzed had the same irradiation data with the first except that the average flux intensity was increased to  $10 \text{ kW/cm}^2$ . Finally, the third sample analyzed at the same wavelength with the PRF shifted to 37.425 MHz and the average power increased to 500W for an average flux intensity of  $10 \text{ kW/cm}^2$ .

Chapter V includes the conclusions resulting from analysis of the new research regarding the single mode and multimode simulations of the TJNAF FEL operation, and the damage induced from the irradiations on the Slip-cast Fused Silica samples.

For FEL operation driven by the 34.5 MeV energy electron pulses, it was found that even though the maximum power is obtained for no taper  $\delta = 0$ , negative taper of  $\delta = -4\pi$  provides higher power at desynchronism values where the operation is more

stable. Additionally, the maximum power with energy spread less than 6% is  $P = 165$  for taper  $\delta = -4\pi$  at desynchronism  $d = 0.01$ .

For FEL operation driven by the 47.5 MeV energy electron pulses, it was found that negative tapering of  $\delta = -4\pi$  gives the highest power and stability in the high power operation area up to  $d = 0.16$ . The maximum power with energy spread less than 6% is  $P = 180$  for taper  $\delta = -4\pi$  at desynchronism  $d = 0.0075$ . Keeping  $\Delta\gamma/\gamma$  less than 6% is a goal effective recirculation of the TJNAF electron beam.

In the damage studies, comparing our experimental results with older experiments on the same material, we found that shifting the wavelength from  $\lambda = 4.825$   $\mu\text{m}$  to  $\lambda = 3.10$   $\mu\text{m}$  and the PRF from 37.4 MHz to 18.7 MHz gave an improvement in penetration rate of 15.4% without airflow and 25.4% with airflow. In both experiments the average power was 100Watts and the intensity was 10 kW/cm<sup>2</sup>. Shifting the wavelength from  $\lambda = 4.825$   $\mu\text{m}$  to  $\lambda = 3.10$   $\mu\text{m}$ , increasing the power from 100 Watts to 500 Watts, and keeping the PRF constant at 37.4 MHz with 10 kW/cm<sup>2</sup> irradiation intensity, improved the penetration rate by 1530% with the presence of airflow and by 9160% without airflow. The volume of total damage increases by 8.7% with the presence of airflow and by 14.1% without it, and the volume of the damage hole is increased by 525% with the presence of airflow and by 59% without it.

**THIS PAGE INTENTIONALLY LEFT BLANK**

## I. INTRODUCTION

"Zippo one! Missiles inbound bearing two seven five." A Principal Warfare Officer or Tactical Action Officer has little time to react to the threat of an incoming anti-ship cruise missile. He has to decide within seconds about ship maneuvers, and hard or soft kill weapon deployment. He must act taking under consideration other factors such as threat type, wind conditions and his own ship characteristics (weapon blind arcs and mutual interference). There is really little time for a human operator to evaluate the threat and respond accordingly. Any error can be fatal. Anti-ship missiles continue to proliferate and constitute a growing threat to warships. Advanced production technology makes missiles faster, stealthier, lower flying, less susceptible to countermeasures and more agile in the terminal phase.

Thus, we understand the importance of a highly sophisticated close-in weapon system that provides quick reaction and a last-ditch inner layer protection, against threats that have penetrated through area and point defenses. Close-in weapons systems can be autonomous and automated. They have their own radar sensors and a multi-barrel gun capable of very high rates of fire, which can tear apart the body of an incoming missile at ranges of about 0.75 to 1.0 nm (1.4 to 1.8 km). The application of high-power lasers to anti-missile defense has been under consideration. Indications are that the technology will have matured to a point where production systems should be available in the 2010 time frame.

There are six established Close-in weapon systems in service: Holland's Signaal Goalkeeper, Russia's Tulamashzavod AK-630 and the Kashtan/Korita CADS-N-1; Spain's Meroka, from Bazan; the Oerlikon-Contraves Seaguard; and the Raytheon Mk 15 better known as Phalanx which is the most widely deployed CIWS in the world.

## **A. THE PHALANX CLOSE-IN WEAPON SYSTEM**

### **1. Description**

The Phalanx CIWS is a closed-loop weapon system. This means that it is tracking both the target and the stream of rounds. It is designed to provide the innermost layer of defense against anti-ship missiles. Phalanx uses a Ku-band pulse Doppler sensor with a tracking antenna at the front and a search antenna at the top. The system is capable of search, detection, threat evaluation, acquisition, track and fire modes which can be done automatically through a digital computer.

Phalanx is normally set up to scan a particular sector and will automatically engage fast air targets unless the hold fire button is pressed. Targets can be detected at 5.6 km (3.0 nm) and acquired at 4.3 km (2.3 nm). When the gun fires, the radar tracks the centroid of outgoing projectiles, predicts their point of closest approach to the target and corrects the aim of the following projectiles. This technique uses variable Pulse Repetition Frequency (PRF) with selected spectral frequency line tracking to measure the stream of projectiles' angular error. Firing usually begins at 1.85 km (1.0 nm), and system reaction time, between target acquisition and fire, is reported to be 3 seconds. Finally the gun caliber is 20 mm and the rate of fire is 3,000-4,500 rds/min.

## 2. Phalanx Simulations

A close-in weapon system has never been challenged in battle conditions.

However simulations have been used to predict its performance against real world threats.

I used these simulations [7], to explore the performance of a typical close-in weapon system, the Phalanx gun. Table 1 shows the simulations input data. It must be mentioned that the effects of gravity and air drag have been taken into account and also that the missile doesn't maneuver.

<u>Height of Gun</u>	25 m
<u>Height of target</u>	7 m
<u>Missile Radius</u>	0.2 m
<u>Missile speed</u>	500 m/s
<u>Dispersion angle</u>	0.002 rad
<u>Firing rate</u>	50 rds/s

**Table 1. Simulations Input Data**

The Phalanx gun, as in every gun system, with a high firing rate, suffers from dispersion as a result of vibrations shaking the barrel. The effect of the dispersion, although it is small (1 to 3 millirads), is that the rounds do not go precisely where they are directed. Figure 1 shows the transverse positions of 500 shots at a distance of 1200 m from the gun. As it can be seen, the area that that is covered by the shots at this distance is about 81 m<sup>2</sup> and only 5 out of 500 shots have hit the target of radius 0.2m (shown as a circle in the center).

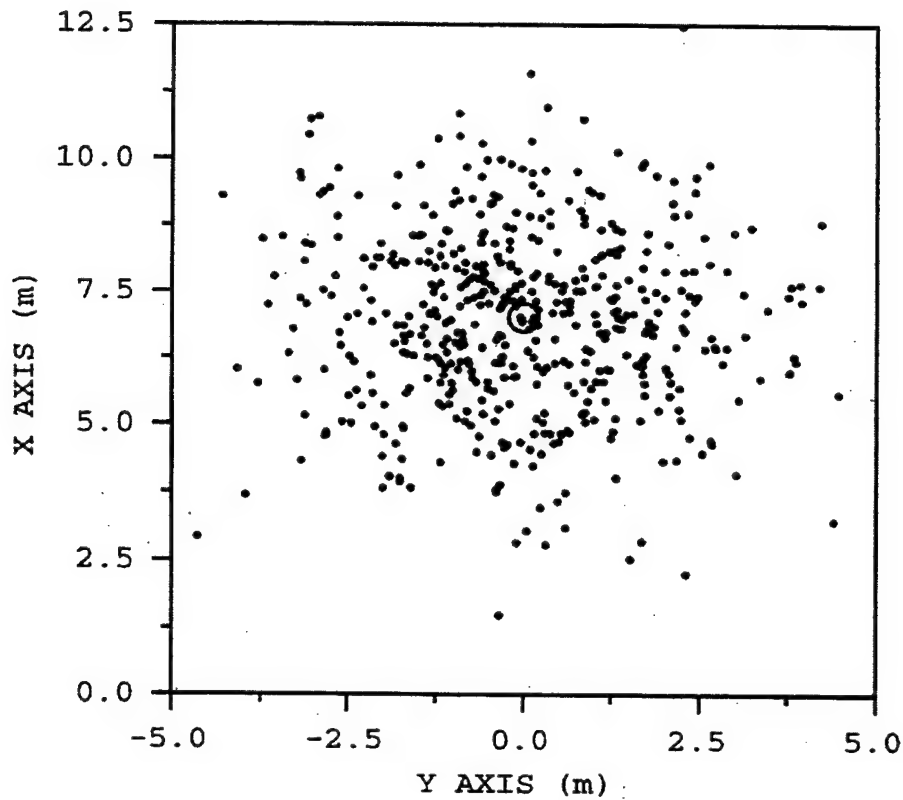


**Figure 1. Transverse Positions of 500 Shots due to Dispersion at 1200 m Range**

Figure 2 shows the probability of one shot hitting the missile vs. range. The probability reduces as range increases. The probability is 62.3% at a distance of 100 m, and drops to 15.6 % at 250 m, and eventually becomes about 0 % after 1250 m.

Unfortunately, one shot is not enough to kill the missile. It is found that six to eight shots are typically required to either destroy the missile's aerodynamics or ignite its warhead.

Figure 3 shows the number of bullets that typically hit the missile as it approaches the ship vs. range. It can be seen that the missile acquired six hits by the time it reached a distance of 150 m. Is that far enough away to say that you have a reliable and trustworthy CIWS weapon system?

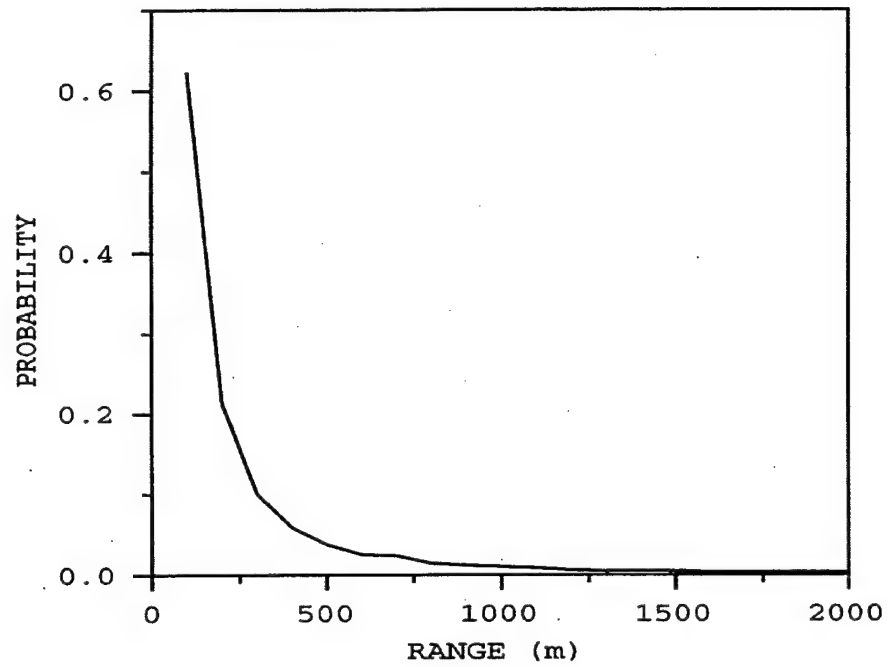


**Figure 2. Single Round Intercept Probability vs. the Range from the Ship**

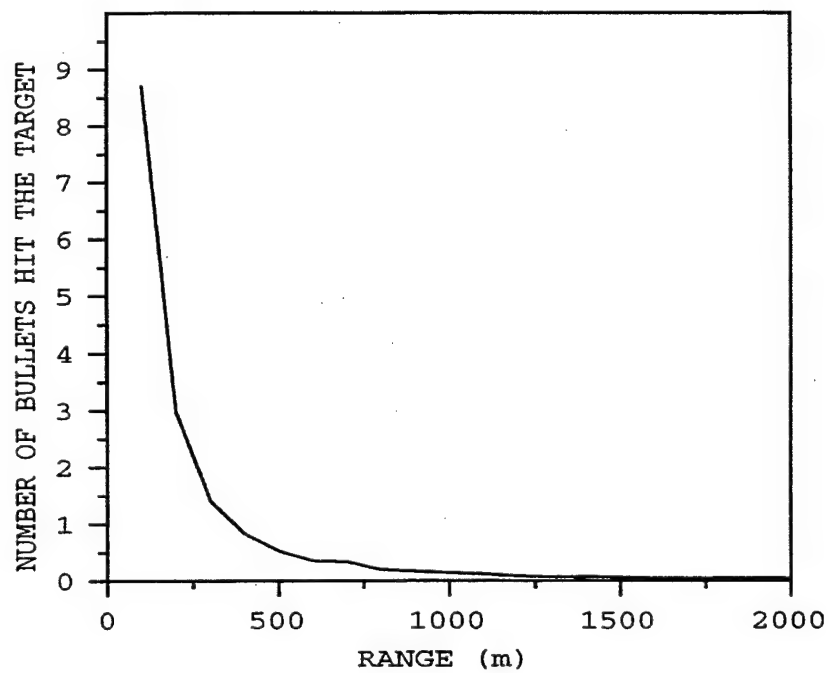


**Figure 3. Number of Accumulated Hits vs. the Range from the Ship**



The answer is "No." Because even if you kill the missile at that distance it doesn't mean that you survived the attack. The debris fuel, and warhead, from the destroyed missile can still hit the ship causing severe damage. Figure 4 shows the random trajectories of 20 random sized debris fragments coming towards the ship, from a missile explosion at 190 m from the ship. As it can be seen, 10 out of 20 sample fragments have hit the ship. Figure 5 shows the probability of a fragment hitting the ship vs. range. At the missile killing distance of 150 m found earlier 60 % of the missile debris hit the ship.

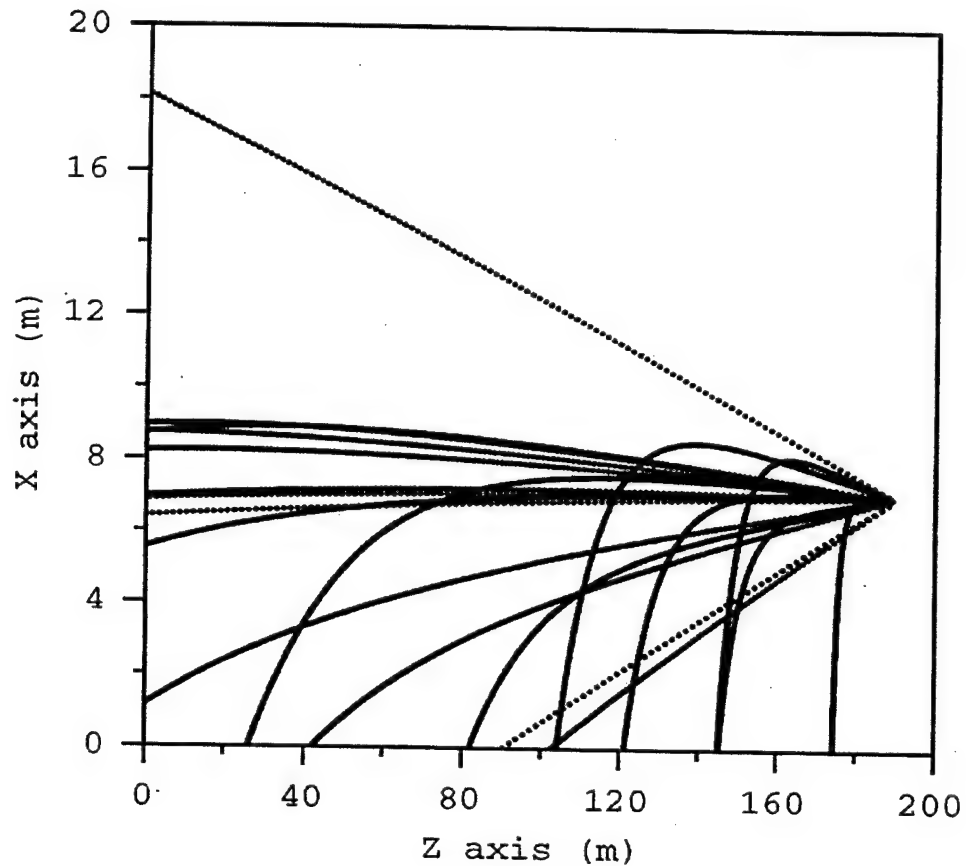


**Figure 4. Possible Debris Trajectories from a Destroyed Inbound Missile**

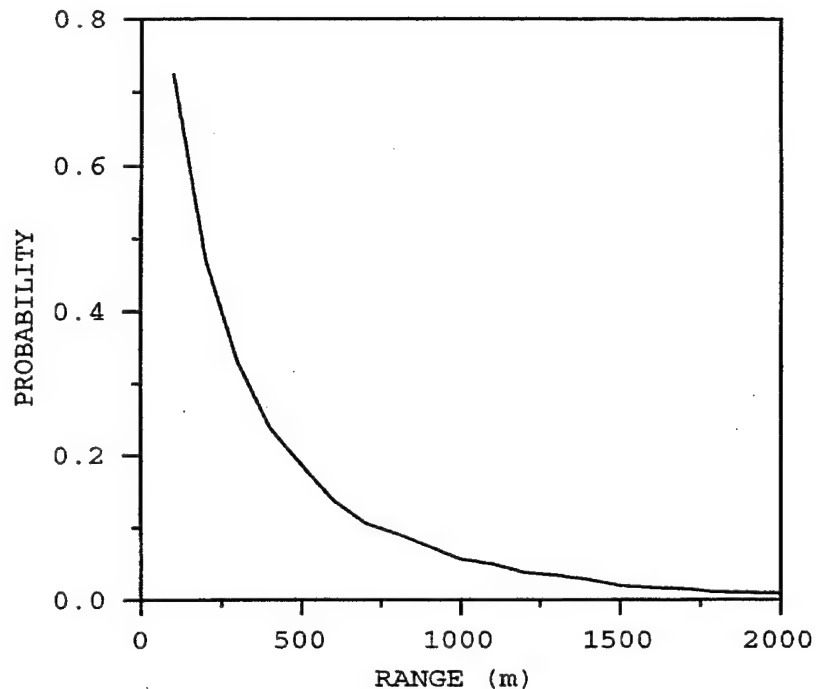


**Figure 5. Probability of a Fragment Hitting the Ship vs. Destruction Range**

The scenario explored at the previous simulations was simple. The missile was non-maneuvering, the engagement commenced at maximum range, the threat was not multiple (one missile was encountered) with perfect tracking by the CIWS radar. However, the results are very disappointing and the existing CIWS has been proven inadequate. A new CIWS system is required, and therefore research should be done on a point air defense system that is much more accurate with longer range.

## **B. HIGH ENERGY LASERS**

Lasers are distinguished by the lasing medium they use. Chemical lasers have become the laser for military directed energy applications. The lasing mediums used are usually hydrogen fluoride (HF), deuterium fluoride (DF), and oxygen iodine. For

example, the MIRACL (Mid Infrared Advanced Chemical Laser), is a 2.2 MW deuterium fluoride laser, with laser wavelength 3.800 nm, and has successfully downed several dummy missiles at a half mile range in test demonstrations at the White Sands Missile Test Range in the USA.

The laser device transforms energy from a power source into light energy of a single wavelength propagating as a highly directional beam. Every laser oscillator has four components: an amplifying medium that increases the intensity of a light beam as it passes through the medium, an energy source that pumps the electrons in the amplifying medium to higher energy levels, an optical cavity consisting of an arrangement of mirrors that feed the amplifying medium, and finally a mechanism that leaks a useful part of the beam of light from the optical cavity without significantly diminishing the amplification process that takes place in the cavity and laser medium. The effect of this mechanism is to provide a beam of coherent light energy, which means that the emitted light energy is of the same frequency and is in phase.

A laser "kills" by heating a target's surface, possibly at a vulnerable point such as a missile's solid rocket casing or liquid fuel tank. The laser must fulfill several tasks to kill a target. First it must generate a high-energy laser beam. Then, the acquisition, tracking and pointing system acquires and tracks and hands over the aim point to the beam control system and range information. Finally the beam control system focuses the beam on the target, and maintains the laser spot on the same area of the target.

Developing a HEL will give to the ship's defense a potent capability. HEL weapons will be able to deliver destructive amounts of energy to a target up to 10

kilometers away at the speed of light, with enough energy to destroy a ballistic missile in a few seconds. The accuracy needed is tens of nanoradians in angle. It will be able to kill a target in a few seconds and shift to a new one. Unlike guided missiles, the HEL's sophisticated and expensive computing and mechanical systems, which hold laser energy accurately onto the target are on the launch platform and are not destroyed during engagement.

Concluding, the laser offers many advantages over a gun and missile-based close-in weapon systems. These include almost instantaneous reaction at the speed of light and long missile destruction ranges, rapid re-engagement, a large and renewable magazine, line of sight accuracy, precision aim pointing, and high single shot cost-effectiveness.

In practice, various problems are yet to be solved, such as thermal blooming, atmospheric attenuation, beam focusing, power generation, and equipment weight and volume. However, while the technology promises much, research and development efforts to produce a trustworthy and deployable system are continuing

### **C. THE FREE ELECTRON LASER**

The free electron laser is a high-energy laser and consists of three main components: the electron accelerator, the undulator, and the optical resonator. An electron beam is accelerated in the accelerator to a relativistic speed and enters into the resonator. Inside the resonator there is the undulator. The undulator consists of a series of alternating magnets that produce a transverse, sinusoidal magnetic field along the undulator axis, which makes the relativistic electron beam wiggle. In this way, the

electrons accelerate and radiate energy in the forward direction. In the presence of light, some electrons gain kinetic energy from the optical field and move faster, while other electrons are losing energy, giving it to the field, and slowing down. This results in bunching of the electrons, leading to coherent radiation. Bunching is essential because the emission rate for the bunched electron beam is proportional to the square of the number of electrons. On the other hand, the emission rate for the beam of randomly positioned electrons is only proportional to the number of electrons. Each electron typically radiates millions of coherent photons in one pass through the undulator. Figure 6 shows a typical configuration of an FEL oscillator.

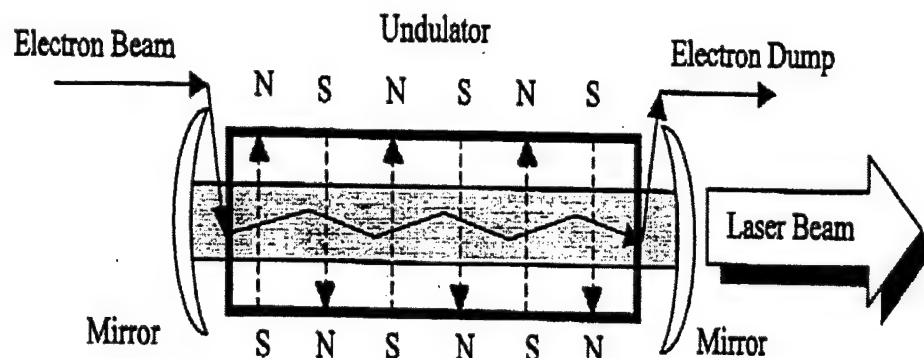


**Figure 6. Oscillating FEL Configuration, From Ref. [3]**

The FEL has potential advantages over the conventional CIWS that are in use now. The first is longer destruction range, which is essential for the ship's survivability because it prevents ship damage from debris. Also, it improves our ability, by giving us time, to engage a second and third successive incoming missile. The second is the

precision in pointing and shot accuracy because lasers don't suffer from dispersion, and can focus on an incoming missile at long ranges.

An important advantage the FEL has over the other laser weapons is that it is tunable to specific wavelengths. The irradiation wavelength of the FEL can be tuned in three ways, either by changing the undulator wavelength, or by changing the undulator's magnetic field amplitude, or by changing the accelerator's electron beam energy. The tunability gives advantage in selecting a wavelength that would give good atmospheric transmission and is appropriate to specific target absorption characteristics.

#### **D. PURPOSE OF THIS THESIS**

This thesis consists mainly of two parts. In the first part, multimode simulations are used to analyze the operation of the Tomas Jefferson National Accelerator Facility (TJNAF) FEL with a negatively tapered undulator. The evolution of short optical pulses in the far infrared are described and show the effects of taper on gain, power and desynchronization. Additionally, single-mode simulations are used to explore the effects of negative taper on gain. In the second part, the results of the TJNAF FEL irradiations on samples of Slip-cast fused Silica are described and discussed.

**THIS PAGE INTENTIONALLY LEFT BLANK**

## II. THE FREE ELECTRON LASER THEORY

### A. THE PENDULUM EQUATION

When the electron beam enters in the undulator, the interaction between the electron beam and the optical field takes place along the undulator. A Cartesian coordinate system is set at the beginning of the undulator with the  $z$  direction along the undulator axis. Assume a helical undulator magnetic field  $\vec{B}$ :

$$\vec{B} = (B_x, B_y, B_z) = B(\cos(k_0 z), \sin(k_0 z), 0) \quad (1)$$

where  $k_0 = 2\pi / \lambda_0$  is the undulator wavenumber,  $z$  is the distance down the undulator, and  $B$  is the magnetic field strength and  $B_x$ ,  $B_y$ , and  $B_z$  are the magnetic field components in the  $x$ ,  $y$  and  $z$  direction. Assume a corresponding circularly-polarized plane wave for the optical field that is generated inside the undulator

$$\vec{E}_s = E(\cos(\Psi), -\sin(\Psi), 0), \quad (2)$$

$$\vec{B}_s = E(\sin(\Psi), \cos(\Psi), 0), \quad (3)$$

where  $E$  is the electric and magnetic field amplitude in cgs units,  $\Psi = kz - \omega t + \phi$ ,  $\phi$  is the optical phase angle,  $\omega$  is the angular frequency,  $t$  is the time and  $k = 2\pi / \lambda$  is the optical wave number. The relativistic Lorentz force equations that govern the motion of the electron in the undulator are

$$\frac{d(\gamma\vec{\beta})}{dt} = -\frac{e}{mc}[\vec{E}_s + \vec{\beta} \times (\vec{B}_s + \vec{B})], \quad (4)$$



$$\frac{d\gamma}{dt} = -\frac{e}{mc} \vec{\beta} \cdot \vec{E}_s, \quad (5)$$

$$\gamma^{-2} = 1 - \vec{\beta} \cdot \vec{\beta}, \quad (6)$$

where  $m$  is the electron rest mass,  $e$  is the electron charge magnitude,  $\vec{\beta} = \vec{v}/c$  is the dimensionless electron velocity, and  $\gamma = (1 - \vec{\beta} \cdot \vec{\beta})^{-1/2}$  is the Lorentz factor.

Substituting the fields in Equation (1), (2) and (3) into Equation (4) and (5), and split  $\vec{\beta}$  into two components:  $\vec{\beta}_\perp = (\beta_x, \beta_y, 0)$  and  $\vec{\beta}_z = (0, 0, \beta_z)$  so that

$$\frac{d(\gamma \vec{\beta}_\perp)}{dt} = -\frac{e}{mc} [E(1 - \beta_z)(\cos(\Psi), -\sin(\Psi), 0) + B\beta_z(-\sin(k_0 z), \cos(k_0 z), 0)], \quad (7)$$

$$\frac{d(\gamma \beta_z)}{dt} = -\frac{e}{mc} [E(\beta_x \cos(\Psi) - \beta_y \sin(\Psi)) + B(\beta_x \sin(k_0 z) - \beta_y \cos(k_0 z))], \quad (8)$$

$$\text{and } \frac{d\gamma}{dt} = -\frac{e}{mc} E[\beta_x \cos(\Psi) - \beta_y \sin(\Psi)]. \quad (9)$$

For relativistic electron ( $\gamma \gg 1$ ),  $E(1 - \beta_z) \ll B\beta_z$  and Equation (7) becomes

$$\frac{d(\gamma \vec{\beta}_\perp)}{dt} = -\frac{e}{mc} B\beta_z [-\sin(k_0 z), \cos(k_0 z), 0]. \quad (10)$$

Equation (10) can now be integrated with respect to  $t$  to find that

$$\vec{\beta}_\perp = -\frac{K}{\gamma} [\cos(k_0 z), \sin(k_0 z), 0]. \quad (11)$$

where the undulator parameter is  $K = eB\lambda_0 / 2\pi mc^2$ . Inserting Equation (11) into

Equation (9) we find that

$$\frac{d\gamma}{dt} = \frac{eEK}{\gamma mc} \cos(\zeta + \phi), \quad (12)$$

where the electron phase,  $\zeta = (k + k_0)z - \omega t$ , determines the  $z$  position relative to an optical wavelength,  $\lambda$

Substituting Equation (11) in Equation (6) we obtain

$$\gamma^{-2} = 1 - \vec{\beta} \cdot \vec{\beta} = 1 - \beta_z^2 - \beta_\perp^2 = 1 - \beta_z^2 - K^2 / \gamma^2, \text{ or } (1 + K^2)\gamma^{-2} = 1 - \beta_z^2. \quad (13)$$

Differentiating both sides of Equation (13) with respect to  $t$ ,  $d\gamma/dt$  and  $d\beta_z/dt$  are related

$$\frac{\dot{\gamma}}{\gamma} = \frac{\gamma^2 \beta_z \dot{\beta}_z}{(1 + K^2)}. \quad (14)$$

Now taking the first and the second time derivative of the electron phase,  $\zeta$ , we obtain

$$\dot{\zeta} = (k + k_0)c\beta_z - \omega, \quad (15)$$

$$\ddot{\zeta} = (k + k_0)c\dot{\beta}_z. \quad (16)$$

Solving Equation (16) for  $\dot{\beta}_z$  and substituting in Equation (14), we get

$$\frac{\dot{\gamma}}{\gamma} = \frac{\gamma^2 \beta_z \ddot{\zeta}}{(1 + K^2)(k + k_0)c}. \quad (17)$$

For relativistic electrons  $\beta_z \cong 1$  and  $k \gg k_0$ , Equation (17) becomes

$$\frac{\dot{\gamma}}{\gamma} = \frac{\ddot{\zeta}}{2\omega_0} \quad (18)$$

where near resonance  $\omega_0 = \omega(1 + K^2)/2\gamma^2$ . The resonance condition is

$$\lambda = \frac{\lambda_0(1 + K^2)}{2\gamma^2}. \quad (19)$$

In order for the electrons to interact strongly with the optical field, they must satisfy the

resonance condition: namely that one wavelength of light,  $\lambda$ , passes over an electron as the electron travels through one undulator wavelength,  $\lambda_0$ .

Solving Equation (18) for  $\ddot{\zeta}$  and substituting into Equation (12) we get the Pendulum Equation of electron motion within the undulator

$$\ddot{\zeta} = \frac{2\omega_0 \dot{\gamma}}{\gamma} = \frac{2eKE\omega_0}{\gamma^2 mc} \cos(\zeta + \phi). \quad (20)$$

It is helpful when designing a FEL to use dimensionless parameters when ever possible. Therefore, we define the dimensionless time,  $\tau = ct / L$ , where  $L$  is the undulator length, so that  $\tau$  is equal to 0 at the beginning of the undulator and 1 at the end. We also define the dimensionless complex optical field  $a = |a|e^{i\phi}$  where  $|a| = 4\pi e N K L |E| / \gamma^2 mc^2$ . Thus the Pendulum Equation becomes

$$\dot{\nu} = \ddot{\zeta} = |a| \cos(\zeta + \phi). \quad (21)$$

where  $(\dot{\dots}) = d(\dots) / d\tau$ , and the dimensionless electron phase velocity is

$\nu = \dot{\zeta} = L[(k + k_0)\beta_z - k]$ ; if  $\nu=0$  the electrons are at resonance. The electron phase velocity is proportional to the electron dimensionless velocity  $\beta_z$ , so that when  $\nu$  decreases the electron slows down and gives energy up to the optical field. This is what we always want to occur for a powerful laser. In order to have optical gain, more electrons must give up energy to the optical field than take energy from it. From the Pendulum Equation, we see that the maximum energy loss from the electrons occurs when  $\cos(\zeta + \phi) = -1$  or when electrons are bunched at  $\zeta + \phi = \pi$ . This is the goal of the FEL.

## B. THE WAVE EQUATION

The development of the complex optical wave equation starts from Maxwell's wave equation acting on the vector potential  $\vec{A}$ ,

$$\left[ \vec{\nabla}^2 - \frac{1}{c^2} \frac{\partial^2}{\partial t^2} \right] \vec{A} = -\frac{4\pi}{c} \vec{J}_\perp, \quad (22)$$

where  $\vec{J}_\perp$  is the transverse current density and the vector potential corresponding to the fields in Equation (2) and (3) is

$$\vec{A}(z, t) = \frac{c}{\omega} E(z, t) [\sin(\Psi), \cos(\Psi), 0]. \quad (23)$$

where optical phase is  $\Psi = kz - \omega t + \phi(z, t)$ . Taking the second derivative of Equation (23) with respect to  $z$  gives

$$\begin{aligned} \frac{\partial^2 \vec{A}}{\partial z^2} &= \frac{1}{k} \frac{\partial E}{\partial z} \left[ k + \frac{\partial \phi}{\partial z} \right] [\cos(\Psi), -\sin(\Psi), 0] \\ &+ \frac{1}{k} \frac{\partial^2 E}{\partial z^2} [\sin(\Psi), \cos(\Psi), 0] + \frac{1}{k} \frac{\partial E}{\partial z} \left[ k + \frac{\partial \phi}{\partial z} \right] [\cos(\Psi), -\sin(\Psi), 0] \\ &+ \frac{E}{k} \frac{\partial^2 \phi}{\partial z^2} [\cos(\Psi), -\sin(\Psi), 0] + \frac{E}{k} \left[ k + \frac{\partial \phi}{\partial z} \right]^2 [-\sin(\Psi), -\cos(\Psi), 0] \end{aligned} \quad (24)$$

Now taking the second derivative of Equation (23) with respect to  $t$  gives

$$\begin{aligned} \frac{\omega}{c} \frac{\partial^2 \vec{A}}{\partial t^2} &= \frac{\partial E}{\partial t} \left[ \frac{\partial \phi}{\partial t} - \omega \right] [\cos(\Psi), -\sin(\Psi), 0] + \frac{\partial^2 E}{\partial t^2} [\sin(\Psi), \cos(\Psi), 0] \\ &+ \frac{\partial E}{\partial t} \left[ \frac{\partial \phi}{\partial t} - \omega \right] [\cos(\Psi), -\sin(\Psi), 0] + E \frac{\partial^2 \phi}{\partial t^2} [\cos(\Psi), -\sin(\Psi), 0] \end{aligned}$$

$$+ E \left[ \frac{\partial \phi}{\partial t} - \omega \right]^2 [-\sin(\Psi), -\cos(\Psi), 0] \quad (25)$$

Next, assume the optical amplitudes and phases varying slowly in time and space so that  $\partial E / \partial z \ll kE$ ,  $\partial \phi / \partial z \ll k\phi$ ,  $\partial E / \partial t \ll \omega E$ ,  $\partial \phi / \partial t \ll \omega \phi$ , and  $\omega = kc$ . This allows us to use only the first-order derivatives because the second order derivatives are small. Applying this approximation to Equations (24) and (25) and inserting the results into Equation (22) we obtain

$$\begin{aligned} \left[ \bar{\nabla}^2 - \frac{1}{c^2} \frac{\partial^2}{\partial t^2} \right] \bar{A} \cong & 2 \left[ \frac{\partial E}{\partial z} + \frac{1}{c} \frac{\partial \phi}{\partial t} \right] [\cos(\Psi), \sin(\Psi), 0] \\ & + 2E \left[ \frac{\partial \phi}{\partial z} + \frac{1}{c} \frac{\partial \phi}{\partial t} \right] [-\sin(\Psi), -\cos(\Psi), 0] \cong -\frac{4\pi}{c} \bar{J}_\perp. \end{aligned} \quad (26)$$

The current density for a single electron is  $\bar{J}_\perp = -ec\bar{\beta}_\perp$ . Substituting Equation (11) for  $\bar{\beta}_\perp$ , we get

$$\bar{J}_\perp = \frac{ecK}{\gamma} [\cos(k_0 z), \sin(k_0 z), 0] \quad (27)$$

We introduce the dimensionless time  $\tau = ct / L$  again so that  $\tau$  is equal to 0 at the beginning of the undulator and 1 at the end. Substituting  $\tau$  and Equation (27) in Equation (26), we obtain

$$2 \left[ \frac{1}{L} \frac{\partial E}{\partial \tau} \right] [\cos(\Psi), \sin(\Psi), 0] + 2E \left[ \frac{1}{L} \frac{\partial \phi}{\partial \tau} \right] [-\sin(\Psi), -\cos(\Psi), 0] \cong$$

$$-\frac{4\pi eK}{\gamma}[\cos(k_0 z), \sin(k_0 z), 0]. \quad (28)$$

Equation (28) can be separated using two expressions representing change in  $E$  and change in  $\phi$ . Thus Equation (28) becomes

$$\frac{\partial E}{\partial \tau} = -\frac{2\pi eLK}{\gamma} \cos(\zeta + \phi), \quad (29)$$

and

$$\frac{\partial \phi}{\partial \tau} = \frac{2\pi eLK}{\gamma} \sin(\zeta + \phi), \quad (30)$$

where  $\zeta = (k + k_0)z - \omega t$  is the electron phase. Equations (29) and (30) are the wave equations driven by a single electron, but we need to evaluate the result from a beam of electrons using a sum over many electrons in the FEL beam. This can be done by taking the average  $\langle \dots \rangle$  and multiplying it by electron density,  $\rho$ , resulting in

$$\frac{\partial E}{\partial \tau} = -\frac{2\pi e\rho LK}{\gamma} \langle \cos(\zeta + \phi) \rangle, \quad (31)$$

and

$$\frac{\partial \phi}{\partial \tau} = \frac{2\pi e\rho LK}{\gamma} \langle \sin(\zeta + \phi) \rangle. \quad (32)$$

Taking the derivative of the complex electric field  $E = |E|e^{i\phi}$  with respect to  $\tau$  and inserting Equations (31) and (32) we obtain

$$\frac{\partial E}{\partial \tau} = -\frac{2\pi e\rho LK}{\gamma} [\langle \cos(\zeta + \phi) \rangle - i \langle \sin(\zeta + \phi) \rangle] e^{i\phi}, \quad (33)$$

which can be simplified to

$$\frac{\partial E}{\partial \tau} = -\frac{2\pi e \rho L K}{\gamma} \langle e^{-i\zeta} \rangle. \quad (34)$$

From the pendulum equation we know that the dimensionless optical field is  $a = |a|e^{i\phi}$ ,

where  $|a| = 4\pi e N K L |E| / \gamma^2 m c^2$ . Therefore the final form of the wave equation is

$$\frac{\partial a}{\partial \tau} = \dot{a} = -j \langle e^{-i\zeta} \rangle, \quad (35)$$

where  $j = 8\pi^2 e^2 \rho N K^2 L^2 / \gamma^3 m c^2$  is the dimensionless current.

The growth of the optical field and therefore the development of the laser energy depend on both the dimensionless current and the average electron phase. If there is no current or no electron bunching, there is no growth of the optical field.

### C. THE FEL PHASE-SPACE EVOLUTION

The pendulum equation motivates a discussion of the FEL electron phase-space evolution. The phase-space evolution describes the microscopic motion of the electrons on the scale of the optical wavelength. The phase-space simulations that will be shown are at the upper limit of the weak-field regime ( $a_0 = 3$ ) and low current ( $j = 1$ ).

Figure 7 shows the FEL phase-space evolution of twenty sample electrons at resonance. There are typically many millions of electrons in each optical wavelength, but the evolution of only twenty sample electrons are shown. The vertical axis in phase-space is proportional to the electron energy while the horizontal axis is the electron's phase within a section of the electron beam one wavelength of light long. Figure 7 also shows the "separatrix." The separatrix is given by the formula  $\nu = 2|a|[1 + \sin(\zeta + \phi)]$  [8].

It separates the open and closed phase-space paths and passes through the critical points  $(-\pi/2, 0)$  and  $(3\pi/2, 0)$ . The peak-to-peak height of the separatix is  $4|a|^{1/2}$  [8]. On the top right of the phase-space evolution the gain in optical energy is plotted, and on the right bottom the change of the optical field phase. Starting at resonance leads to no gain. This happens because the half of the electrons gain energy from the optical field, while the other half give away the same amount of energy to it. It can also be seen that at resonance the optical phase shift is relatively large and the electrons become bunched at  $\zeta = \pi/2$ .

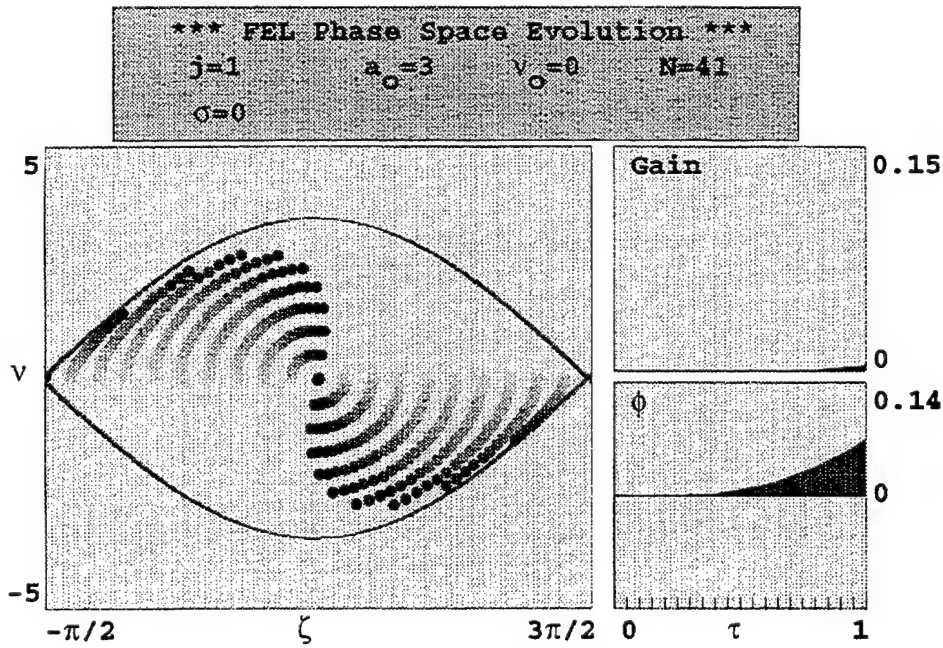


Figure 7. The FEL Phase-Space Evolution at Resonance

Figure 8 shows the gain and phase curves with respect to the initial electron phase velocity  $v_0$ . The gain spectrum is anti-symmetric in  $v_0$  with a peak gain of  $G = 0.125$  at  $v_0 = 2.7$ . At resonance,  $v_0 = 0$ , there is no gain at any time, while for values  $0 < v_0 < 6.2$  there is net absorption of the optical power. The optical phase shift is symmetric in  $v_0$



with a peak value of  $\Delta\phi = 0.074$  at  $\nu_0 = 0$ . At the phase velocity for maximum gain  $\nu_0 = 2.7$ , the phase shift is only  $\Delta\phi = 0.015$ . Figure 9 shows the FEL phase-space evolution slightly off resonance at the optimum initial phase velocity of  $\nu_0 = 2.7$ . It can be seen that the electron bunching occurs at  $\zeta = \pi$ , the phase for which the maximum electron's energy loss occurs.

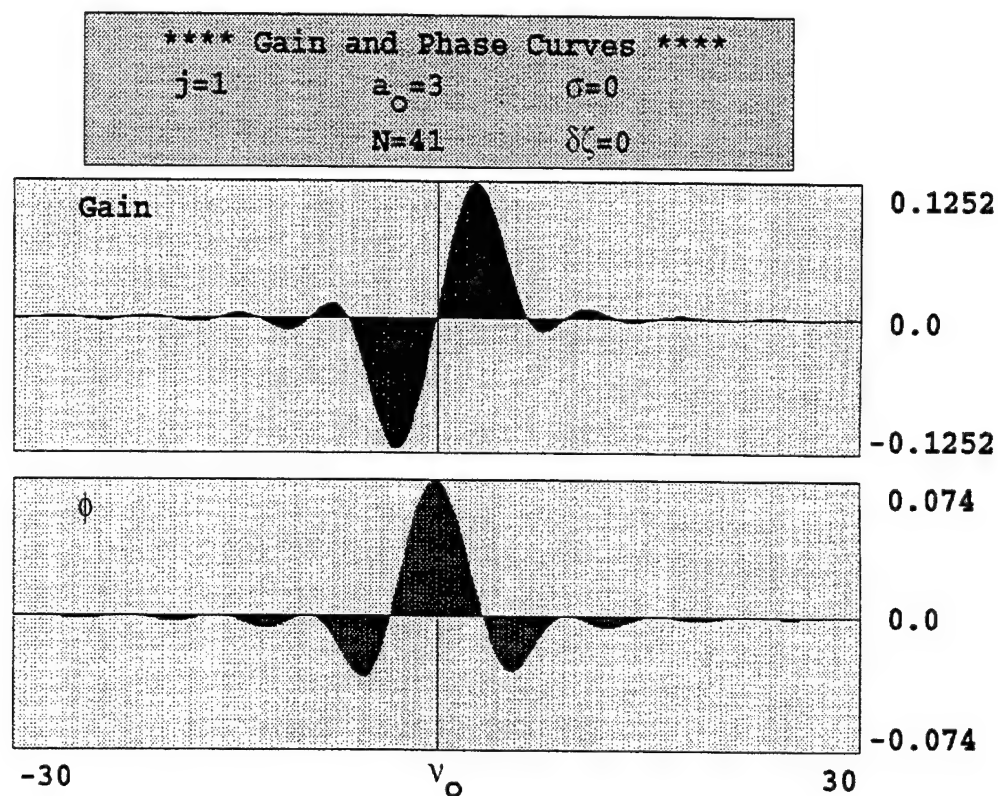


Figure 8. The FEL Gain and Phase Curves

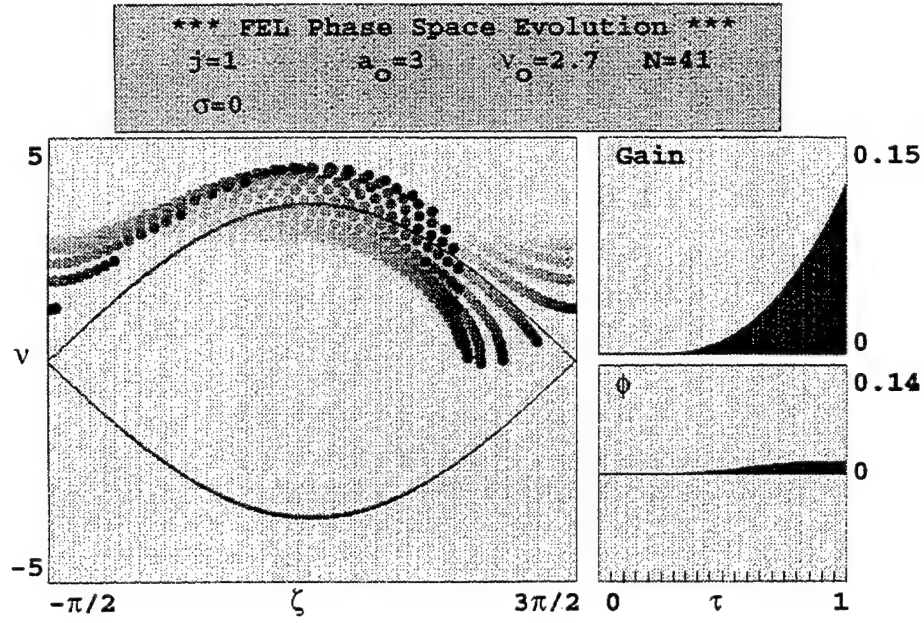


Figure 9. The FEL Phase-Space Evolution at Optimum Initial Phase Velocity

#### D. THE TAPERED UNDULATOR

The FEL resonance condition found during the derivation of the pendulum equation is

$$\lambda = \frac{\lambda_0(1 + K^2)}{2\gamma^2} \quad (36)$$

where  $\lambda$  is the optical wavelength,  $\lambda_0$  is the undulator wavelength,  $\gamma$  is the Lorentz factor and  $K = eB\lambda_0 / 2\pi mc^2$  is the dimensionless undulator parameter. At normal saturation, the electron beam loses enough energy to the laser light to shift across the gain bandwidth by  $\Delta v = 4\pi N \Delta \gamma / \gamma$  [9], moving away from the value of  $v$  for peak gain to a value of  $v$  for no gain or even loss.

Taper the undulator can be used to accelerate the electron's phase  $\dot{\nu} = \ddot{\zeta} = \delta$  so that resonance is maintained. This can be done either by increasing (negative tapering) or decreasing (positive tapering) the undulator wavelength, or the undulator magnetic field strength, or both. The phase acceleration  $\delta$  is given by  $\delta = -2\pi N \Delta \lambda_0 / \lambda_0$  when the undulator wavelength is modified, or by  $\delta \approx -4\pi N K^2 \Delta K / [(1 + K^2) K_0]$  when the undulator field strength is modified [9]. Now that the tapering is introduced, the pendulum equation includes an additional constant torque  $\delta$  and has the form

$$\ddot{\zeta} = \delta + |a| \cos(\zeta + \phi). \quad (37)$$

The desirable criteria for positive tapering are [9]:

$$|a| > \delta \geq 4|a|^{1/2} \geq 2\pi. \quad (38)$$

The condition on the left is the requirement to have trapped electrons in the tapered phase space; the middle requirement dictates that the tapered acceleration exceed the untapered deceleration; and finally, the right condition dictates that the FEL work in the strong field regime ( $a \gg \pi$ ).

In the next chapter, single-mode and short pulse multi-mode simulations on negative tapering, (increasing the undulator magnetic field), will be discussed. It is proven here that a constant torque  $\delta$  corresponds to an approximately linear increase of the magnetic field along the undulator axis. The electron Equation with tapering in weak field optical fields has the form

$$\dot{\nu} = \delta. \quad (39)$$

Integrating Equation (39) with respect to dimensionless time  $\tau$ , and substituting  $\tau = ct/L$

and  $\nu = L[(k + k_0)\beta_z - k]$ , we get

$$L[(k + k_0)\beta_z - k] = \delta\tau. \quad (40)$$

where  $L$  is the undulator length,  $k$  is the optical wavenumber,  $k_0$  is the undulator

wavenumber, and  $z$  is the distance down the undulator. Inserting  $\beta_z = 1 - (1 + K^2)/2\gamma^2$

in Equation (40) we obtain

$$L \left[ k \left( 1 - \frac{1 + K^2}{2\gamma^2} \right) + k_0 \left( 1 - \frac{1 + K^2}{2\gamma^2} \right) - k \right] = \delta\tau. \quad (41)$$

Assuming that  $k \gg k_0$  for  $\gamma \approx 70$  and solving for  $K$ , equation (41) becomes

$$K(\tau) = \sqrt{\frac{2\gamma^2}{k} \left( k_0 - \frac{\delta\tau}{L} \right) - 1}. \quad (42)$$

The resonance condition for the wavenumbers is  $k = k_0 2\gamma^2 / (1 + K_0^2)$ , where  $K_0$  is the

undulator parameter in the beginning of the undulator. Solving the resonance condition

for  $2\gamma^2/k$ , and substituting to Equation (42) we get

$$K(\tau) = \sqrt{K_0^2 - \left( \frac{1 + K_0^2}{k_0} \right) \frac{\delta\tau}{L}}. \quad (43)$$

Recall that  $k_0 = 2\pi / \lambda_0$  and  $L = N\lambda_0$ , where  $N$  is the number of undulator periods, so

that Equation (43) becomes

$$K(\tau) = K_0 \sqrt{1 - \left( \frac{1 + K_0^2}{2\pi N K_0} \right) \delta \tau}. \quad (44)$$

Figure 10 shows Equation's (44) graph for  $K_0 = 1$ ,  $N = 41$ , and  $\delta = -8\pi$ . For  $N$  large, the square-root argument can be accurately expanded to

$$K(\tau) \approx K_0 \left( 1 - \frac{1 + K_0^2}{2\pi N K_0} \delta \tau \right) \quad (45)$$

which shows that a straight line is approximately correct.

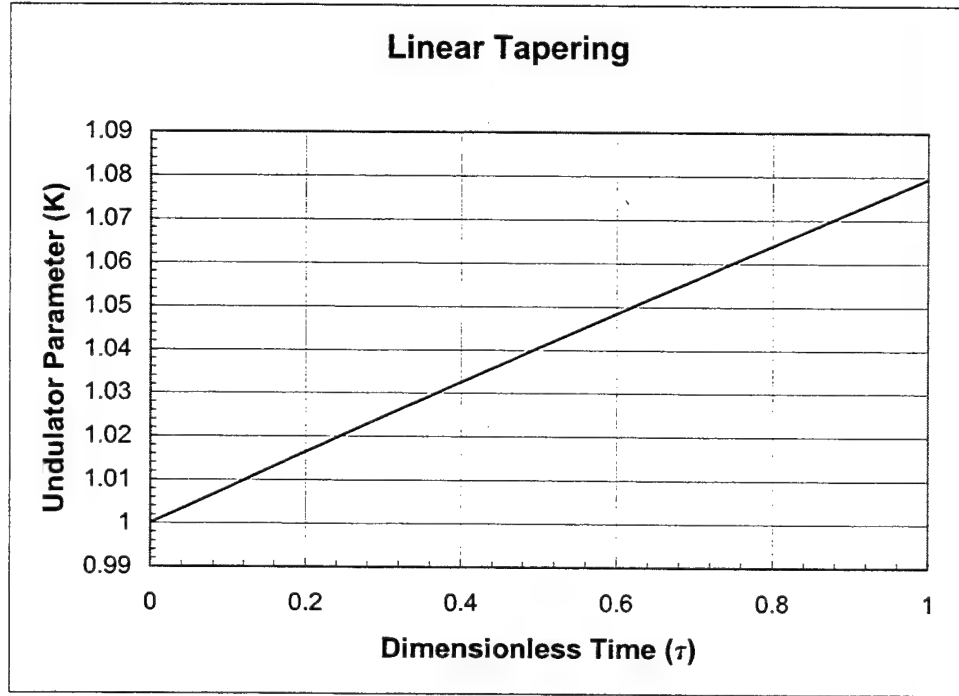


**Figure 10. Linear FEL Inverse Tapering**

Figure 11 shows the final FEL phase-space distribution for a periodic undulator ( $\delta = 0$ ), while Figures 12 and 13 show the final phase-space distribution of a positive ( $\delta = 4\pi$ ) and a negative ( $\delta = -4\pi$ ) tapered undulator, respectively.

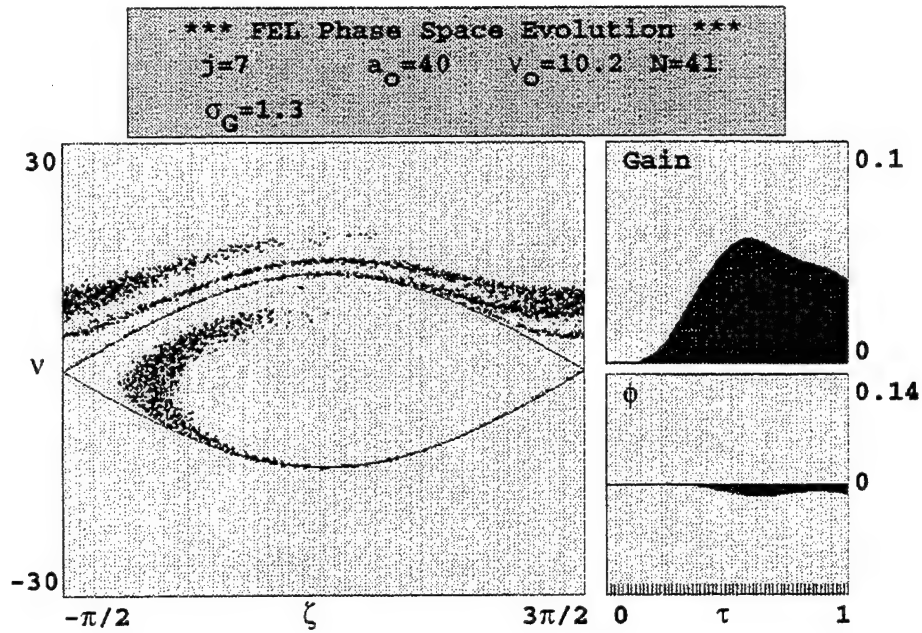


Figure 11. The FEL Phase-Space Evolution of a Periodic Undulator ( $\delta = 0$ ) in Strong Fields

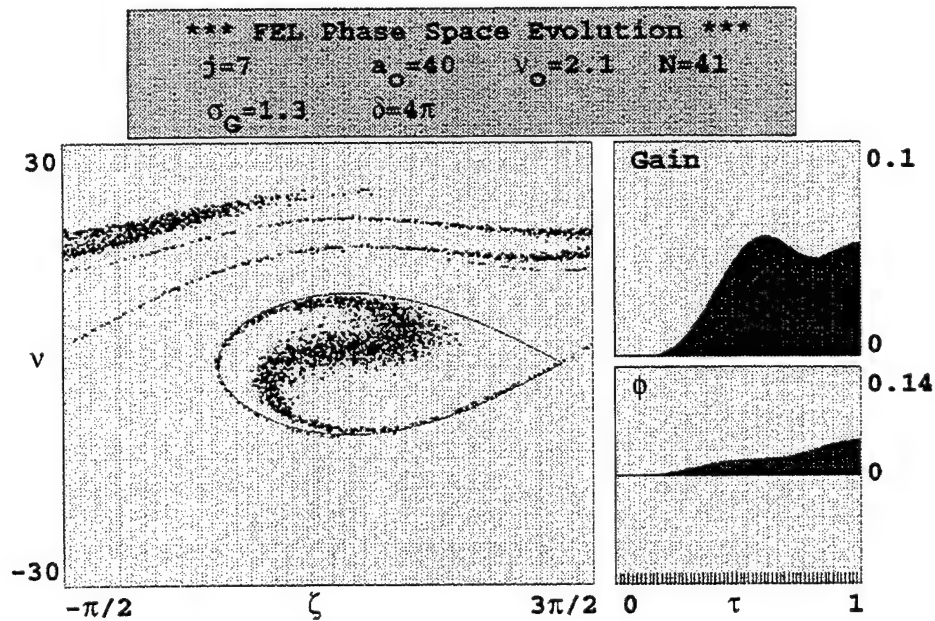
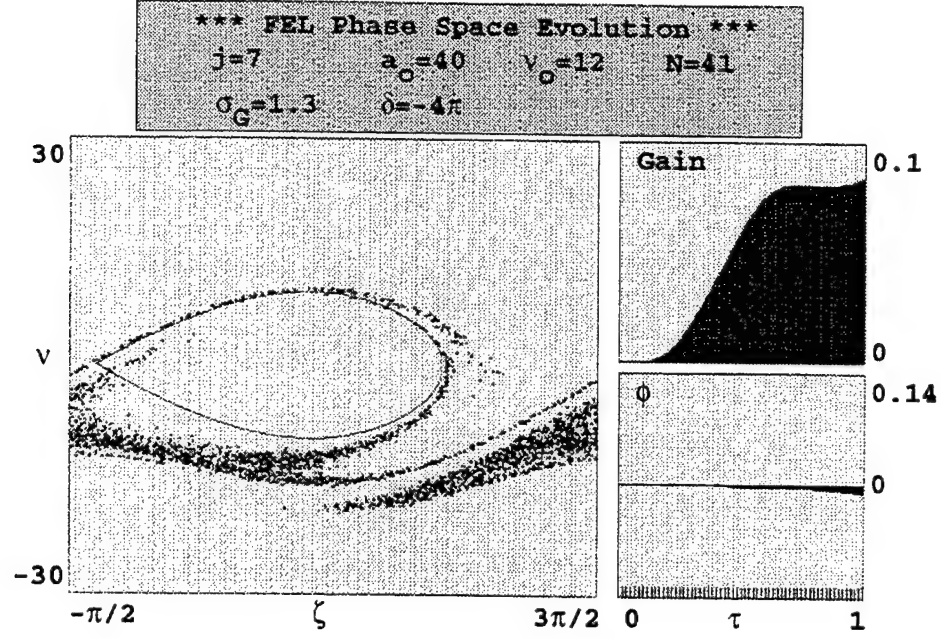


Figure 12. The FEL Phase-Space Evolution of a Positive Tapered Undulator ( $\delta = 4\pi$ ) in Strong Field



**Figure 13. The FEL Phase-Space Evolution of a Negative Tapered Undulator ( $\delta = -4\pi$ ) in Strong Field**

The electrons in the simulations started at the optimum phase velocity for each case and with a Gaussian spread of in phase velocity of  $\sigma_G = 1.3$ . The initial strong optical field  $a_0 = 40$  is amplified by a current of  $j = 7$ , in an undulator with  $N = 41$  periods. The separatix in the tapered undulators, Figures 12 and 13, surrounds a smaller area of closed orbits than does the untapered case in Figure 11, and is given by

$$v^2 = 2\delta(\zeta - \zeta_0) + 2|a|(\sin(\zeta + \phi) - \sin(\zeta_0 + \phi)), \quad (46)$$

where  $\zeta_0 = 2\pi - \cos^{-1}(-\delta/|a|) - \phi$  [9]. It must also be noted that the separatix shapes of the positive and negative taper are reversed; the area enclosed decreases as the taper phase acceleration  $\delta$  increases, and increases in stronger fields as  $a_0$  increases

In the untapered undulator of Figure 11, the electrons in the presence of strong optical field have over bunched and the gain is saturated. The gain at the end of the evolution is  $G_f = 3.74\%$ . Using a positively tapered undulator ( $\delta = 4\pi$ ) of Figure 12, there is bunching of the trapped electrons in closed orbits inside the separatrix near  $\zeta = \pi$ , and the final gain is increased to  $G_f = 5.36\%$ . For the negatively tapered undulator ( $\delta = -4\pi$ ) in Figure 13, no electrons are trapped inside the separatrix and all of them are in open orbits. The bunching occurs as electrons travel around the closed orbit region of phase space at final phase-space sites around  $\nu \approx -12$  where the electrons have lost significant energy, and the final gain is  $G_f = 8.45\%$ .

Concluding it must be mentioned that the tapered undulators, both positive or negative, are more efficient in strong optical fields, but have smaller gain than the untapered undulator in weak fields.

## E. THE SHORT PULSE EVOLUTION

The majority of the FEL oscillators are driven by short electron pulses rather than a continuous beam. Electron pulses are considered to be short when they are comparable to one slippage distance,  $N\lambda$ , where  $N$  is the number of undulator periods and  $\lambda$  is the optical wavelength.

As short electron pulses enter the FEL oscillator, short optical pulses are generated due to spontaneous emission bouncing back and forth between the resonator mirrors. The distance between the mirrors is  $S$ , and is bigger than the undulator length,  $S > L$ . The optical pulse travels a distance  $2S$ , and at time intervals of  $2S/c$  reaching



the beginning of the undulator at  $\tau = 0$ . At this time, an electron pulse also enters the undulator. The desynchronism,  $d$ , is as the displacement between the electron pulse and the optical pulse at  $\tau = 0$ , normalized to the slippage distance. If  $d = 0$ , then the optical pulse coincides with the electron pulse each pass; this is called exact synchronism. Desynchronism is easily adjusted in practice by moving the resonator mirrors by microns with a piezoelectric crystal.

Figure 14 shows a pulse evolution simulation with electrons entering in the undulator at the optimum phase velocity  $v_0$ , at exact synchronism ( $d = 0$ ). The peak current is  $j = 6$ , the pulse length is  $\sigma_z = 1.3$ , the desynchronism value is  $d = 0$ , the quality factor is  $Q = 10$  implying 10% resonator loss per pass, the tapering phase acceleration is  $\delta = -6\pi$ , the number of undulator periods is  $N = 41$ , and finally the standard deviation of a small fluctuation in the initial electron phases is  $\delta\zeta = 10^{-4}$ . The simulation plot contains six windows. At the upper left is the dimensionless optical field shape  $a(z, n)$ , as a function of  $z$  which is scaled to the slippage distance, and its evolution with the number of passes  $n$ . At the upper middle and right are the optical power spectrum  $P(\nu, n)$  and the electrons' spectrum  $f(\nu, n)$  respectively, as a function of the phase velocity  $\nu$  and their evolution with  $n$ . At the lower left, the longitudinal profile of the current density  $j$  is shown for reference at times  $\tau = 0$  and  $\tau = 1$ , as a function of  $z$  which is also scaled to the slippage distance. The electron pulse is assumed to be parabolic in shape with the form  $j(z) = j(1 - 2z^2 / \sigma_z^2)$  for  $j(z) > 0$ , and 0 otherwise [10].

At the lower middle is the weak field gain  $G(\nu)$  for reference, as a function of  $\nu$ . At the lower right is the evolution of the total power  $P(n)$  as the number of passes  $n$  increases.

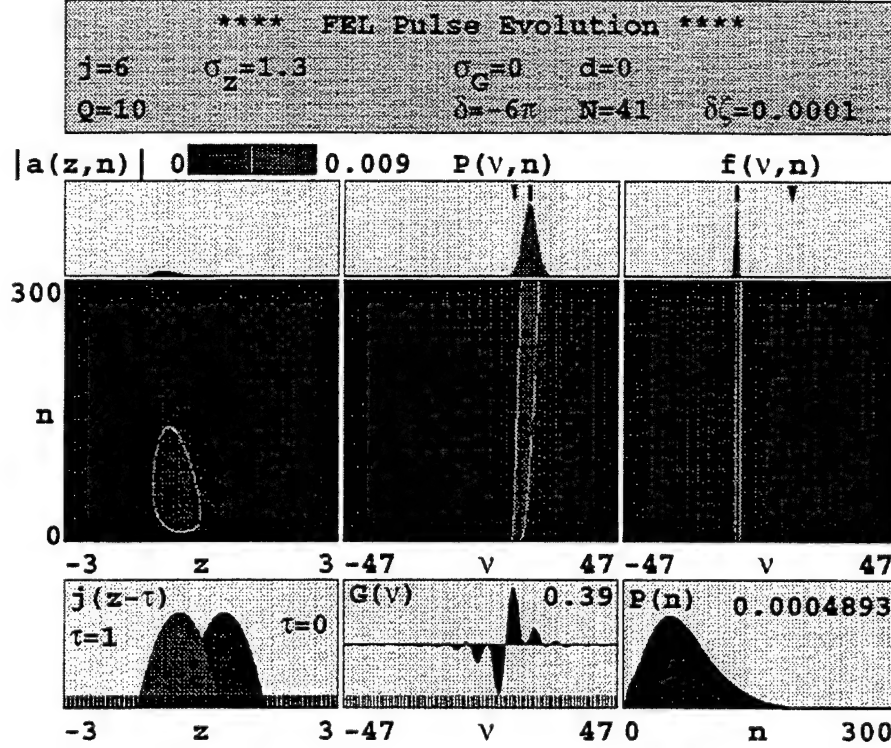


**Figure 14. The FEL Pulse Evolution at Exact Synchronism ( $d=0$ )**

Surprisingly we see in Figure 14 that exact synchronism leads to no steady state power. This result can be explained in the following way. The electron pulse and the optical pulse enter in the undulator at the same moment each pass. They begin to interact along the undulator, but in the beginning no electron bunching occurs, and therefore, there is no gain. This delay in the gain is called lethargy [10]. Then bunching occurs and gain develops. As the pulses travel together, the gain increases but since the light pulse moves slightly faster than the electron pulse, the electron pulse falls behind most of the amplification occurs at the trailing edge of the light pulse. Consequently, the light pulse

is distorted on each pass and its centroid is traveling with speed lower than  $c$  even though it is in vacuum. Eventually, over many passes the coupling between the two pulses will be lost and the resonator losses will cause the optical pulse to decay and the FEL will fail to operate. The simulation in Figure 14 has been artificially started with a coherent pulse of light and shows that peak power occurs at  $n = 50$  passes, but then the optical and electron pulses decouple so that the FEL power dies out after about  $n = 170$  passes.

In order to compensate for the slower speed of the distorting light pulse, the resonator path  $S$  must be reduced by  $\Delta S$  so that  $d = -2\Delta S / N\lambda$ . If  $d$  becomes too big, the compensation is too severe, and the pulses decouple after many passes leading again to no steady state power. Figure 15 shows the pulse evolution simulation for an FEL with exactly the same characteristics as that of Figure 14, but with desynchronism  $d = 0.015$ .

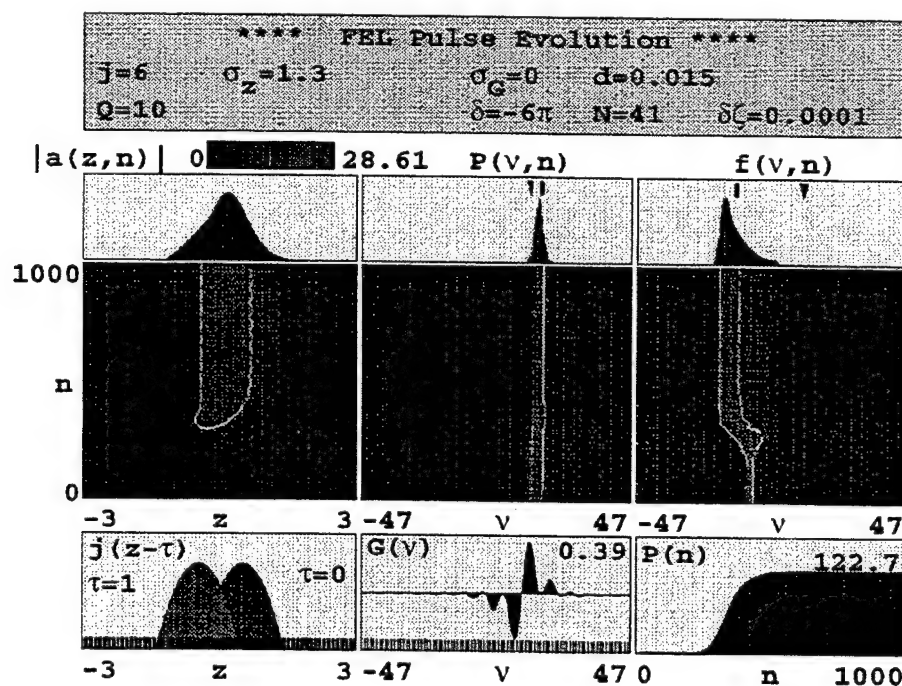


Figure 15. The FEL Pulse Evolution at  $d=0.015$

Figure 15 also shows that no power develops until  $n = 250$  passes, and that steady state power is reached after  $n = 500$  passes.

## F. THE TRAPPED PARTICLE INSTABILITY

The trapped-particle instability is an effect that occurs in strong optical fields when electrons become trapped in deep potential wells in phase-space. The height of the separatrix and area enclosed increases with the optical field amplitude  $a$ . When the FEL reaches high-power, the optical field gets longer so that many electrons become trapped on the closed orbits of phase-space. The electrons that are trapped near the stable fixed point, electron phase  $\zeta \approx \pi/2 - \phi$ , are executing a part of a synchrotron oscillation [11]. The stable fixed point for the tapered undulator is at electron phase  $\zeta \approx \cos^{-1}(-\delta/|a|) - \phi$  [11]. The synchrotron oscillation frequency for the trapped electrons is given by

$$\nu_s \approx \left(|a|^2 - \delta^2\right)^{1/4}; \text{ for the untapered where } \delta = 0 \text{ the synchrotron frequency reduces to } \nu_s \approx |a|^{1/2} \text{ [11].}$$

The synchrotron oscillation frequency mixes with the carrier wave and appears as sidebands around the fundamental at  $\nu_0 \pm \nu_s$  causing a shift from the fundamental wavelength by  $\Delta\lambda/\lambda = \nu_s/2\pi N$ . This is often undesirable for FEL operation, because the optical spectrum broadens. In weapons applications, the laser beam must propagate through a narrow window frequency in the atmosphere where there is small absorption. The trapped-particle instability may be removed by increasing the desynchronism to reduce the power so that the electrons execute one synchrotron oscillation

( $\nu_s = \sqrt{a} = 2\pi$ ). Figure 16 shows an example of trapped-particle instability. Note that the optical field is strong  $a = 39$ , and a sideband appears on the right of the fundamental frequency at the optical spectrum at  $\nu_s = 2\pi$ .

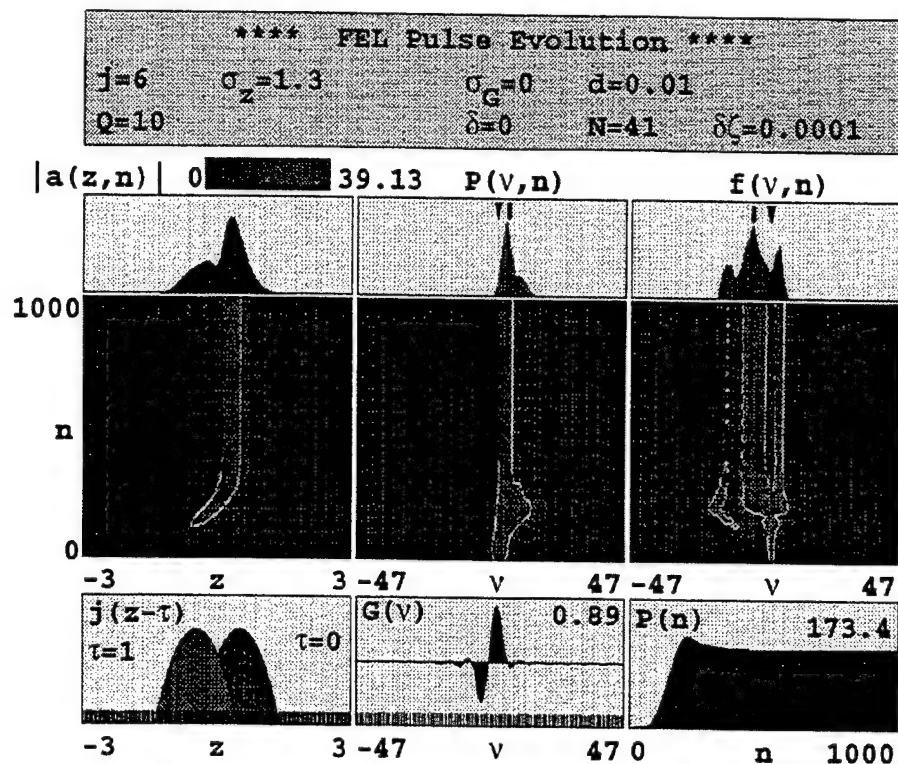


Figure 16. The Trapped-Particle Instability

## G. LIMIT CYCLE BEHAVIOR

Limit cycle behavior can occur in optical pulse structure and power evolution when the FEL is operating in strong optical fields with short pulses. In strong fields when the trapped-particle instability occurs, the oscillations at the synchrotron frequency mix with the optical carrier frequency causing modulations of the optical wave envelope and spectral sidebands at the synchrotron frequency. This modulation of the optical pulse

shape, in combination with the desynchronism effect, create an optical pulse that continually changes from one shape to the other over many passes, resulting in power oscillations. Figure 17 shows an example of limit cycle behavior.

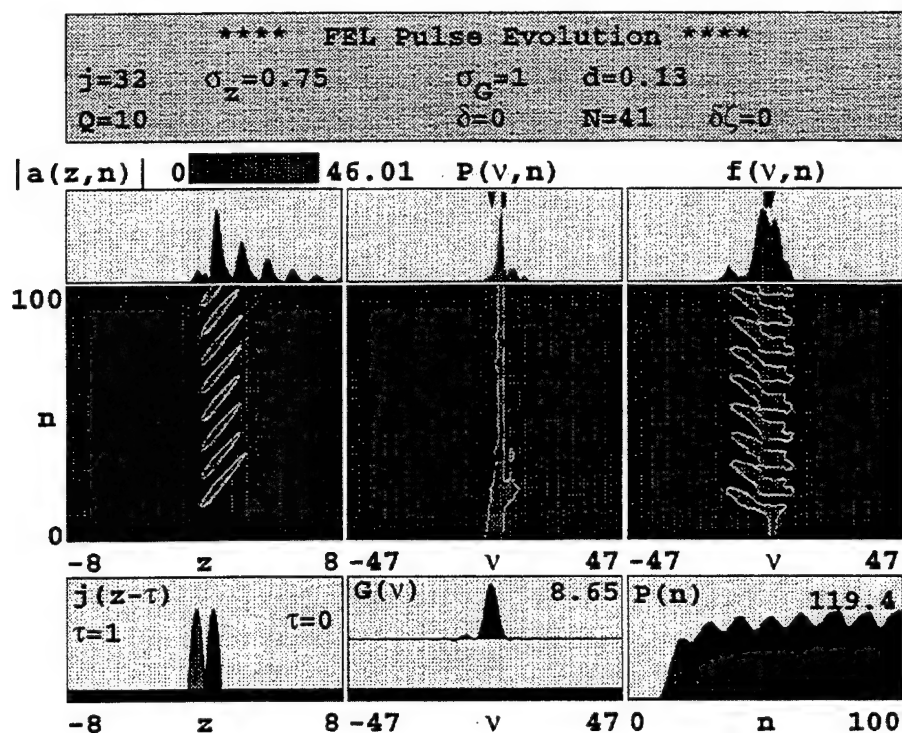


Figure 17. The Limit Cycle Behavior

As it is seen in the pulse evolution  $|a(z,n)|$ , subpulses are continually being formed at the trailing edge of the optical pulse and march forward in  $z$  over many passes due to the desynchronism mechanism. As the subpulses move forward they enter a region of higher gain, and grow, and then continue their movement and decay due to resonator losses. Limit cycle behavior occurs at moderate values of desynchronism and is usually undesirable for weapons applications because the optical spectrum is broadened by the presence of the sidebands and because steady state power is not achieved.

However, it can easily be removed by altering the desynchronism as a result of moving one resonator mirror by microns.

### III. THE TJNAF FEL SIMULATIONS

#### A. INTRODUCTION

Experiments using the TJNAF FEL have been done to explore the operation with inversely tapered undulators. In this chapter, numerical simulations will be presented using the TJNAF experimental parameters. First, single mode simulations will be used to explore the effects of negative taper on gain. Then, multimode simulations will be used to analyze the operation of the TJNAF FEL with the negatively tapered undulator, describing the evolution of short optical pulses in the far infrared and showing the effects of taper and desynchronism on gain and power. In our simulations, the TJNAF FEL will be driven by 34.5 MeV and 47.5 MeV short electron pulses. Tables 2 and 3 show the parameters for both 34.5 MeV and 47.5 MeV operation.



Optical Wavelength $\lambda$	6 $\mu\text{m}$
Undulator Wavelength $\lambda_0$	2.7 cm
Peak Undulator Magnetic Field $B$	5.5 kG
Undulator Periods $N$	41
Undulator Length $L$	1.1 m
Undulator Parameter $K$ (rms)	0.98
Taper Phase Acceleration $\delta$	$\delta = 0, -4\pi, -6\pi, -8\pi$
Electron Energy $\gamma mc^2$	34.5 Mev
Electron Pulse Length $\sigma_z$ normalized to $N\lambda$	1.0
Initial Phase Velocity $v_0$ for peak gain in weak fields	$v_0 = 2.4$ for $\delta = 0$ $v_0 = 8.7$ for $\delta = -4\pi$ $v_0 = 11.7$ for $\delta = -6\pi$ $v_0 = 14.7$ for $\delta = -8\pi$
Peak Current $I$	50 A
Current Density $j$	10
Initial Optical Field $a_0$	0.0
Cavity Losses $1/Q$	0.1

**Table 2. TJNAF 34.5 MeV Electron Pulse Energy Parameters**

Optical Wavelength $\lambda$	3 $\mu\text{m}$
Undulator Wavelength $\lambda_0$	2.7 cm
Peak Undulator Magnetic Field $B$	5.5 kG
Undulator Periods $N$	41
Undulator Length $L$	1.1 m
Undulator Parameter $K$ (rms)	0.98
Taper Phase Acceleration $\delta$	$\delta = 0, -4\pi, -6\pi, -8\pi$
Electron Energy $\gamma mc^2$	47.5 MeV
Electron Pulse Length $\sigma_z$ normalized to $N\lambda$	1.8
Initial Phase Velocity $v_0$ for peak gain in weak fields	$v_0 = 2.4$ for $\delta = 0$ $v_0 = 8.7$ for $\delta = -4\pi$ $v_0 = 11.7$ for $\delta = -6\pi$ $v_0 = 14.7$ for $\delta = -8\pi$
Peak Current $I$	50 A
Current Density $j$	7
Initial Optical Field $a_0$	0.0
Cavity Losses $1/Q$	0.1

**Table 3. TJNAF 47.5 MeV Electron Pulse Energy Parameters**

## B. SINGLE MODE SIMULATION RESULTS

Single mode behavior was explored by examining the effects of negative tapering on gain for a range of initial optical fields ( $0 < a_0 < 40$ ), and initial phase velocities ( $-30 < v_0 < 30$ ). The tapering phase acceleration has values  $\delta = 0, -4\pi, -6\pi$  and  $-8\pi$ , that correspond to linear tapering rate of the dimensionless undulator parameter  $\Delta K / K = 0\%, 5\%, 7.5\%$  and  $10\%$ .

Figure 18 shows the gain plotted as a function of the initial optical field  $a_0$  and the initial phase velocities  $v_0$  for current  $j = 7$ . For  $\delta = 0$  and weak field ( $a_0 \approx 0$ ), the maximum gain is  $G = 113\%$  and occurs at  $v_0 = 2.4$ . For strong field ( $a_0 = 40$ ), the maximum gain reduces to  $G = 4.7\%$  and shifts more off resonance at  $v_0 = 10.8$ . After introducing negative tapering, the maximum weak field gain reduces to  $G = 77\%$  at  $v_0 = 8.7$  for  $\delta = -4\pi$ ,  $G = 46\%$  at  $v_0 = 11.7$  for  $\delta = -6\pi$ , and  $G = 19\%$  at  $v_0 = 14.7$  for  $\delta = -8\pi$ . The strong field gain increases to  $G = 11\%$  at  $v_0 = 12.3$  for  $\delta = -4\pi$ ,  $G = 9.9\%$  at  $v_0 = 15$  for  $\delta = -6\pi$ , and  $G = 9.5\%$  at  $v_0 = 24$  for  $\delta = -8\pi$ . As the inverse taper increases, peak gain in weak fields is shifted to the right along the  $v_0$  axis by  $-\delta/2$  and decreases, whereas the strong field peak gain increases. As the taper increases, the gain spectrum becomes more distorted and a second peak gain develops. For  $\delta = -8\pi$ , two comparable peaks appear, one at  $v_0 = 14.7$  and the other at  $v_0 = 23$ . Figure 19 shows the gain plotted as a function of the initial optical field  $\alpha$  and the initial phase velocities  $v_0$  for current  $j = 10$ . The graphs are similar to the  $j = 7$  curve; the only difference is that the values of

gain for  $j = 10$  are bigger by approximately 52% in weak fields and by approximately 44% in strong fields.

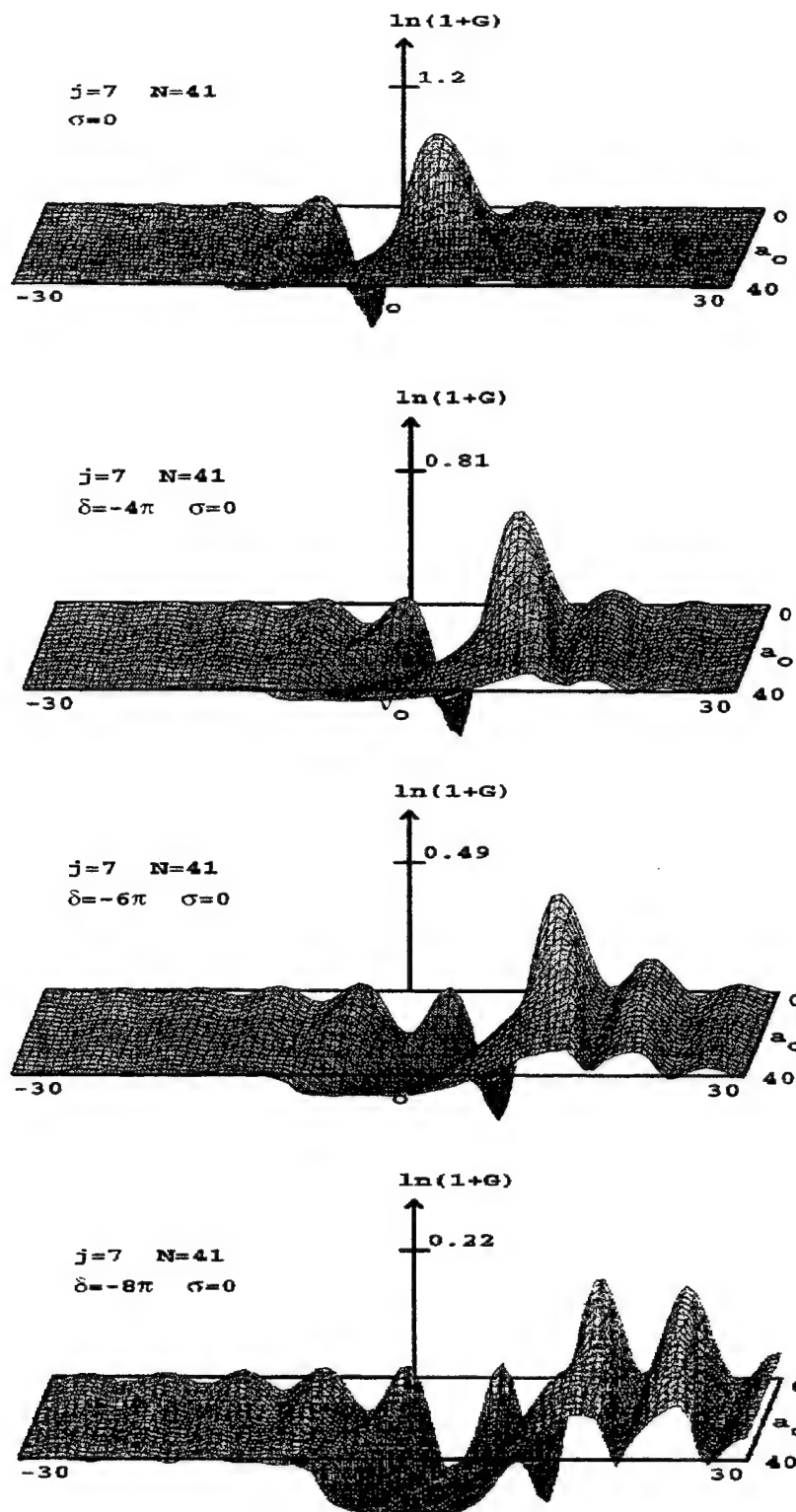


Figure 18. The FEL Gain Spectrum  $G(v_0, \alpha_0)$  for  $j=7$

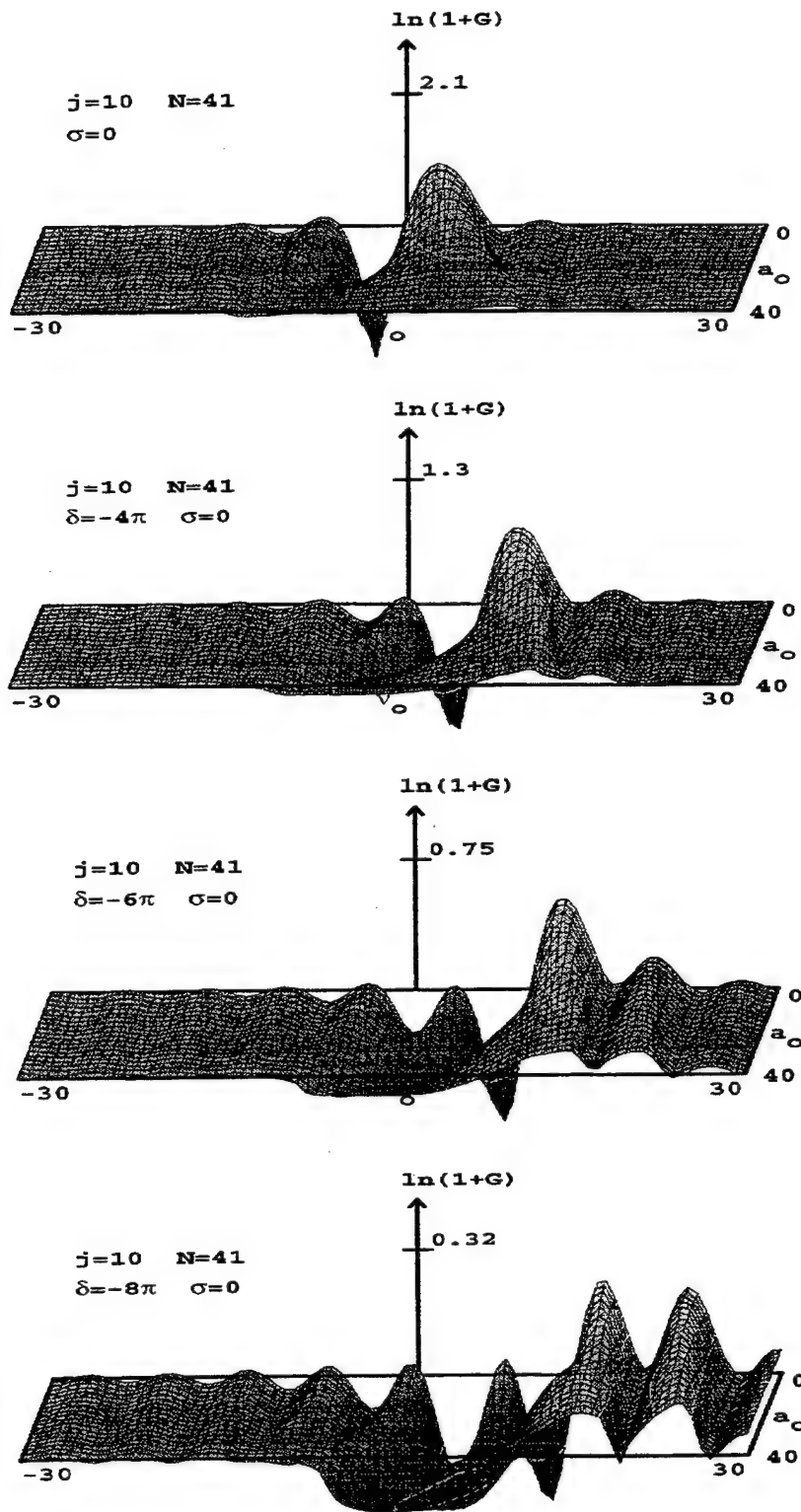


Figure 19. The FEL Gain Spectrum  $G(v_0, \alpha_0)$  for  $j=10$

### C. MULTIMODE SIMULATION RESULTS

My first task was to plot the final steady state power of the FEL as a function of desynchronism  $d$  for  $\delta = 0, -4\pi, -6\pi$  and  $-8\pi$ . In order to achieve this, we ran FEL pulse evolution simulations for various values of desynchronism  $d$  as described in Chapter II, Section E. The input parameters of the TJNAF FEL operation used in the simulations are provided in Table 2 for 34.5 MeV, and in Table 3 for 47.5 MeV energy electron pulses.

The second task was to plot the weak-field steady-state gain as a function of desynchronism  $d$  for  $\delta = 0, -4\pi, -6\pi$  and  $-8\pi$ . The same FEL pulse evolution simulations were run but gain  $G$  was plotted as a function of  $n$  instead of plotting the power  $P$ . The simulations were run long enough to reach steady state gain in weak optical fields ( $a \ll \pi$ ) with  $Q = 10^{10}$  in order to represent no losses.

The third task was to plot the induced electron energy spread  $\Delta\gamma/\gamma$  as a function of desynchronism  $d$  and taper phase acceleration  $\delta$ . This was accomplished using the formula  $\Delta\gamma/\gamma = \Delta v_e / 4\pi N$ , where  $\Delta v_e$  is the electron spectrum full width measured from the electron distribution  $f(v, n)$  on the FEL pulse evolution simulations, and  $N = 41$  is the number of the undulator periods.

Finally, the fourth task was to plot the optical spectrum width as a function of desynchronism  $d$  and taper phase acceleration  $\delta$ , measured from the power spectrum  $P(v, n)$  on the FEL pulse evolution simulations.

## 1. TJNAF FEL Simulation Results Using 34.5 MeV Energy Electron Pulses

Figure 20 shows the graph of the steady-state power as a function of desynchronism  $d$  and taper phase acceleration  $\delta$ . For  $\delta = 0$ , the laser operating range is from  $d = 0.0035$  to  $d = 0.385$ , and reaches maximum power at  $d = 0.004$  of  $P = 206$ . For  $\delta = -4\pi$ , the laser operating range is from  $d = 0.004$  to  $d = 0.29$ , and reaches the maximum at  $d = 0.006$  with  $P = 189$ . For  $\delta = -6\pi$ , the laser operating range is from  $d = 0.005$  to  $d = 0.19$ , and reaches the maximum at  $d = 0.012$  with  $P = 148$ . Finally for  $\delta = -8\pi$ , the laser operating range is from  $d = 0.0065$  to  $d = 0.053$ , and reaches the maximum at  $d = 0.0125$  with  $P = 90$ .

The operating range decreases as the value of  $\delta$  increases. It can be seen that a small change in  $d$  causes large difference in steady-state power for small values of  $d$ . The high power area for small  $d$  is an area of instability. Increasing the value of  $d$ , the FEL operation becomes more stable but the power decreases. For the largest values of  $d$ , the power becomes even smaller due to the reduced coupling between the optical and electron pulses.

The efficiency for the maximum values of the steady state power is  $\eta = 2.2\%$  for  $\delta = 0$ ,  $\eta = 1.9\%$  for  $\delta = -4\pi$ ,  $\eta = 1.5\%$  for  $\delta = -6\pi$  and  $\eta = 0.94\%$  for  $\delta = -8\pi$ . The highest power is achieved from  $d = 0.0035$  to  $d = 0.006$  and from  $d = 0.18$  to  $d = 0.385$  for  $\delta = 0$ ; from  $d = 0.006$  to  $d = 0.015$  and  $d = 0.04$  to  $d = 0.18$  for  $\delta = -4\pi$ ; and from  $d = 0.015$  to  $d = 0.04$  for  $\delta = -6\pi$ . Even though the maximum power is obtained for  $\delta = 0$ ,  $\delta = -4\pi$  provides higher power at desynchronism values where the operation is more stable.



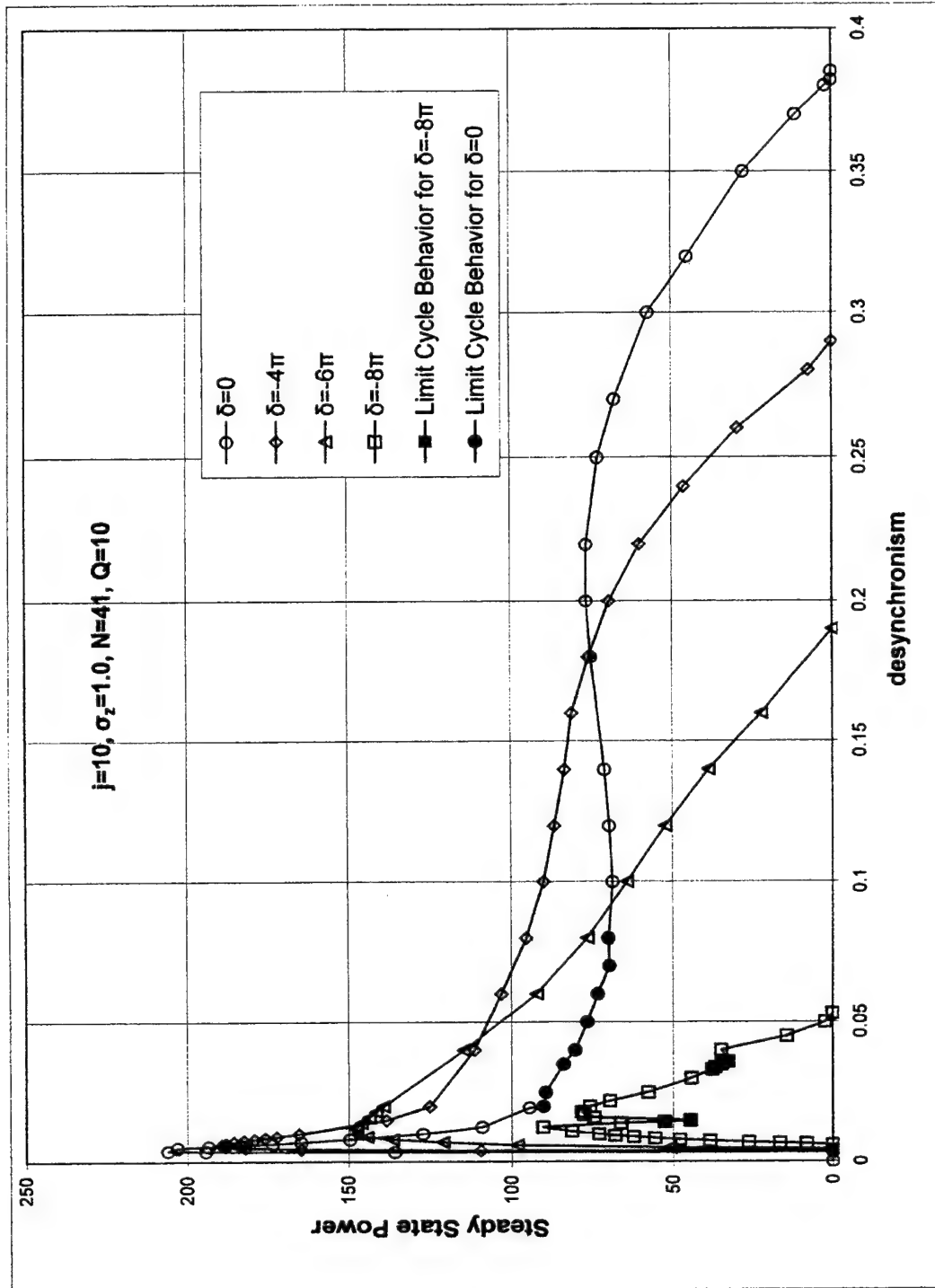


Figure 20. Steady-state Power vs. Desynchronism for 34.5 MeV Energy Electron Pulses.

For small values of  $d$  where the power is too high and the optical fields are too strong, electrons are trapped in deep potential wells and perform synchrotron oscillations causing the trapped particle instability is evident. For  $\delta = 0$ , this occurs between the values of  $d = 0.035$  and  $d = 0.07$ , for  $\delta = -4\pi$  between  $d = 0.004$  and  $d = 0.02$ , for  $\delta = -6\pi$  between  $d = 0.005$  and  $d = 0.018$ , and for  $\delta = -8\pi$  between  $d = 0.009$  and  $d = 0.022$ .

Figures 21 and 22 show the pulse evolution for  $d = 0.0055$  with the trapped-particle instability for  $\delta = 0$  and  $\delta = -4\pi$ . By tapering the undulator the sideband gain is reduced, the optical spectrum width  $P(v,n)$  becomes smaller and the steady state power is also reduced.

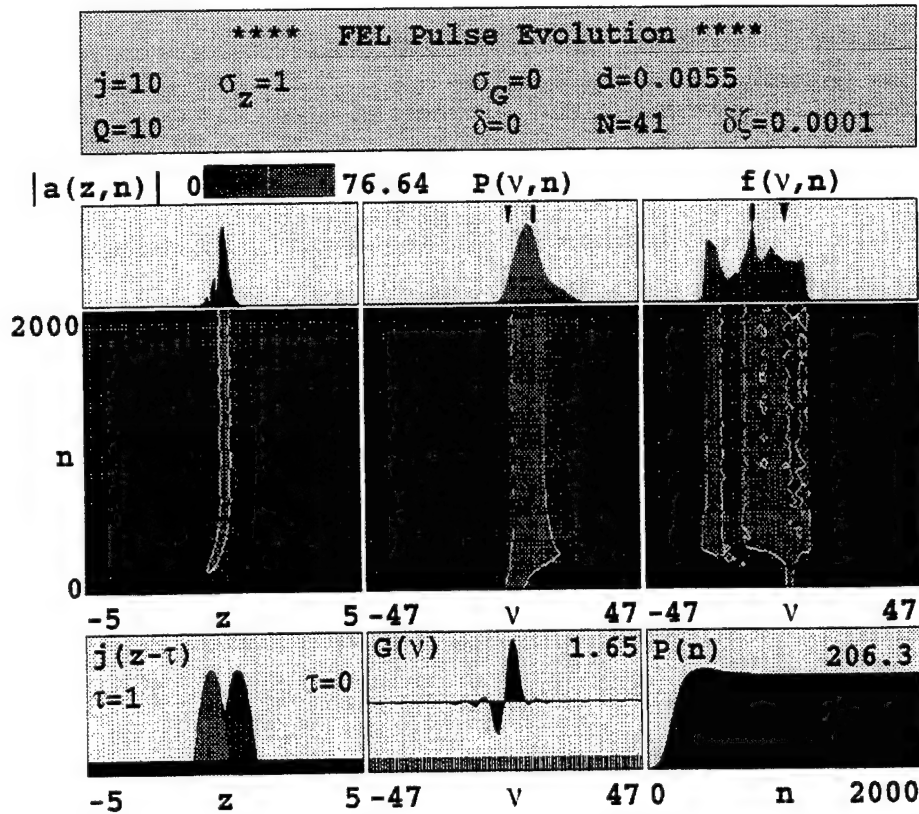
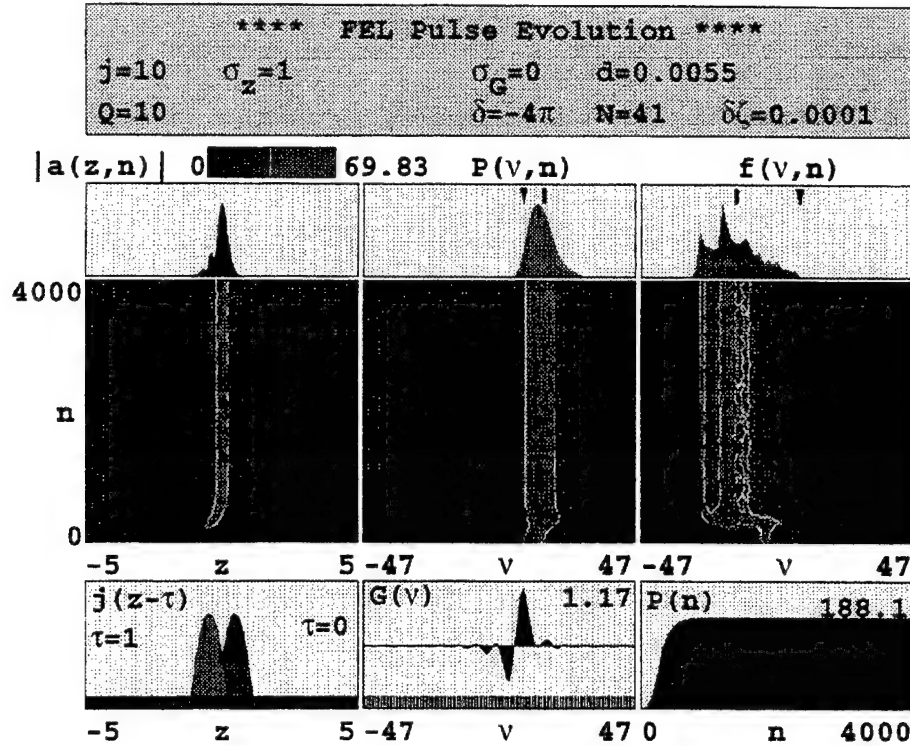


Figure 21. Trapped Particle Instability Example for  $\delta = 0$  and  $d = 0.0055$



**Figure 22. Trapped Particle Instability Example for  $\delta = -4\pi$  and  $d = 0.0055$**

For  $\delta = 0$  between the values of  $d = 0.02$  and  $d = 0.08$ , limit cycle behavior is observed. It is also evident for  $\delta = -8\pi$  between  $d = 0.0145$  and  $d = 0.015$ , and between  $d = 0.033$  and  $d = 0.034$ . Limit cycle behavior, as described in Chapter II Section G, in optical pulse structure and power occurs when trapped particles in strong optical fields combine with short optical pulses. For  $\delta = 0$  the maximum modulation is 9.5% of the average power at  $d = 0.04$  the minimum modulation is 1.5% at  $d = 0.08$ . For  $\delta = -8\pi$ , the maximum modulation is 6.6% of the average power at  $d = 0.015$ , and the minimum modulation is 1.2% at  $d = 0.033$ . Black circles and squares in Figure 20 indicate the average value of the power oscillation. Figures 23 and 24 show the limit cycle behavior

region for  $\delta = 0$  and  $\delta = -8\pi$  while Figure 25 shows the limit-cycle behavior pulse evolution for  $\delta = 0$  and  $d = 0.04$ .

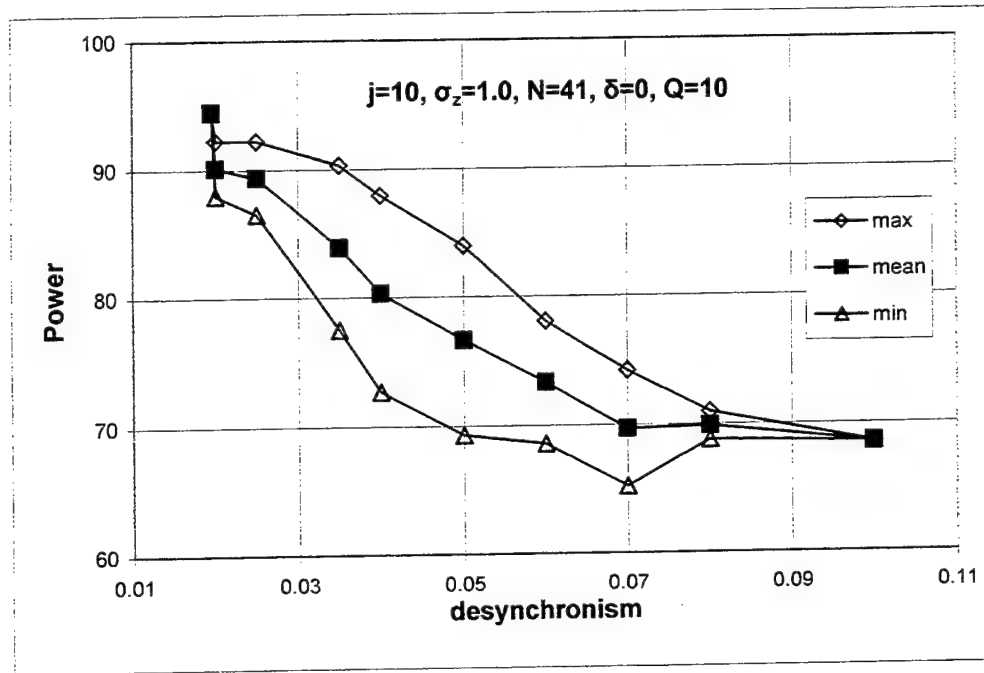


Figure 23. Limit Cycle Behavior Region for  $\delta = 0$

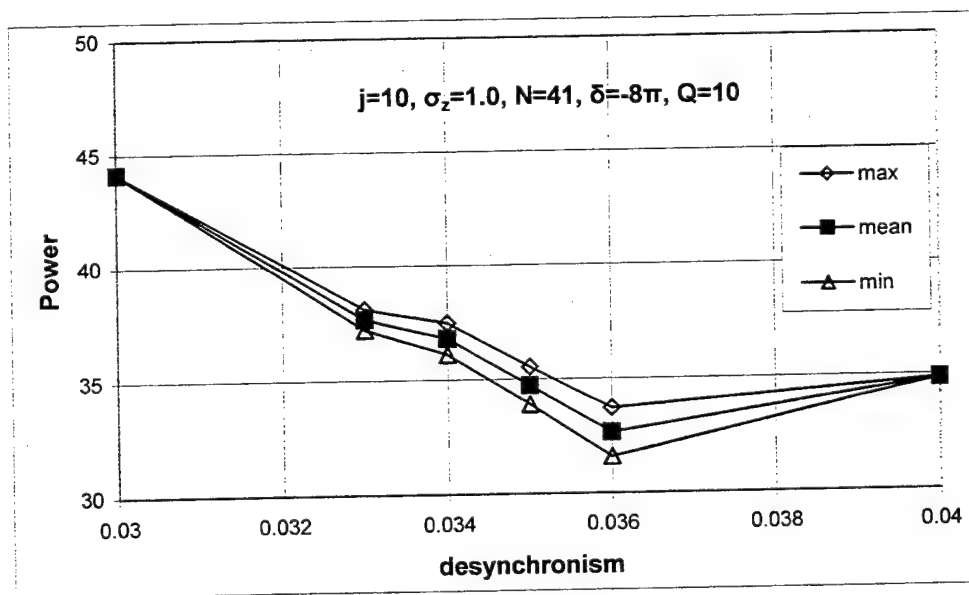
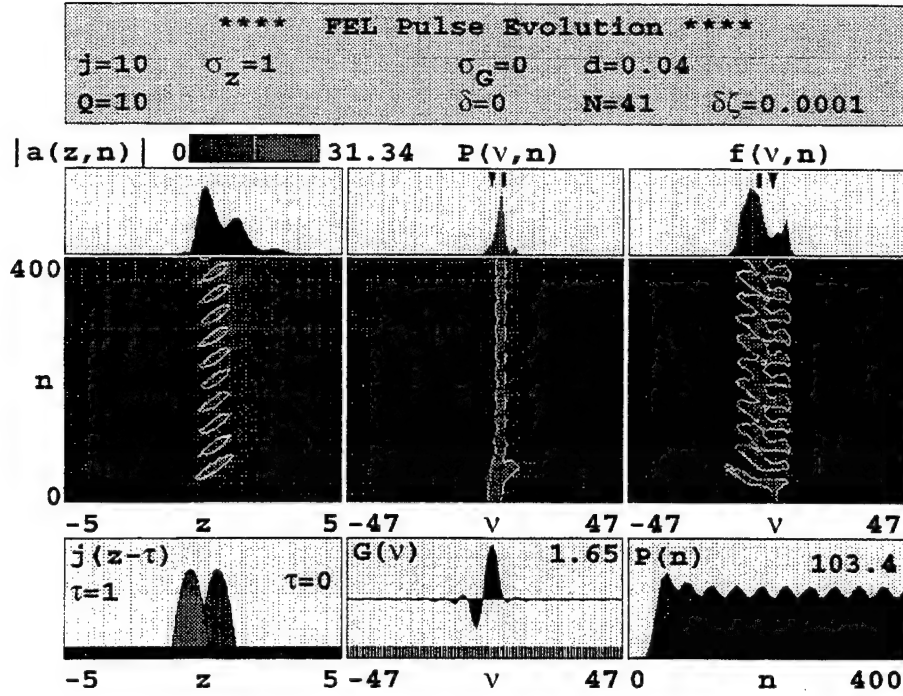


Figure 24. Limit Cycle Behavior Region for  $\delta = -8\pi$



**Figure 25. Limit Cycle Behavior Pulse Evolution for  $\delta = 0$**

At small values of desynchronism the optical pulse is short, only one slippage distance long, results in a broad optical spectrum. At large values of desynchronism, the optical pulse is advanced so far each pass that it decouples from the incoming electron pulse and the steady-state power is reduced. In this region, the optical pulse is longer than the electron pulse, sometimes five to six slippage distances long, and has a long exponential leading edge of the form  $|a(z)| \propto e^{-z/4Qd}$  [10]. The optical spectrum for large desynchronism and a long pulse is narrow. Figure 26 shows the pulse evolution for a small value of desynchronism  $d = 0.005$  and  $\delta = -6\pi$ , and Figure 27 shows the results for large value of desynchronism  $d = 0.16$  and taper  $\delta = -6\pi$ . Note that the optical pulse in Figure 26 is one slippage distance long ( $N\lambda$ ), and in Figure 27 is six slippages distances long.

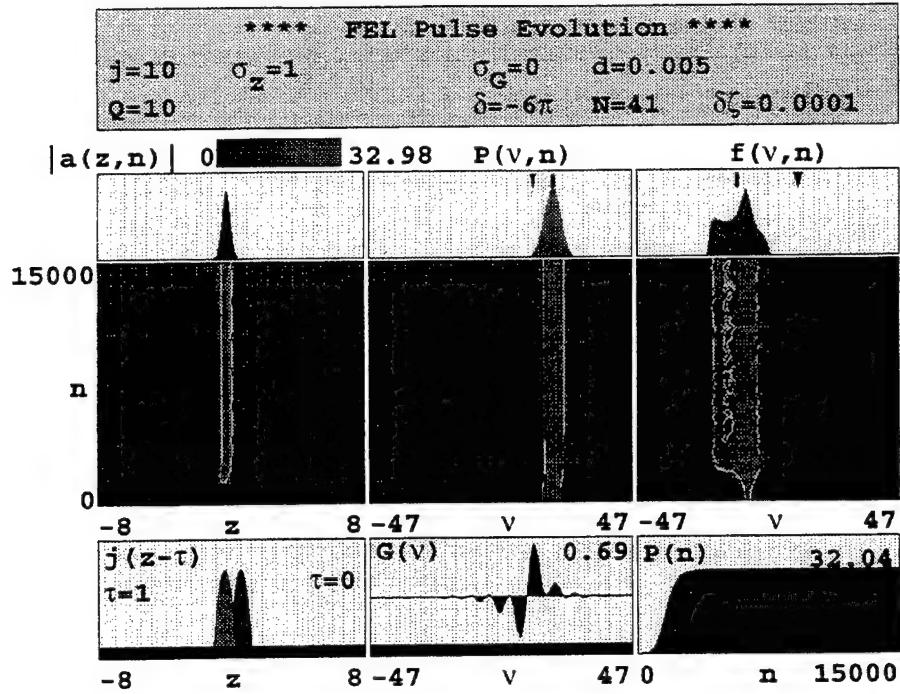


Figure 26. Pulse Evolution for  $\delta = -6\pi$  and  $d = 0.005$

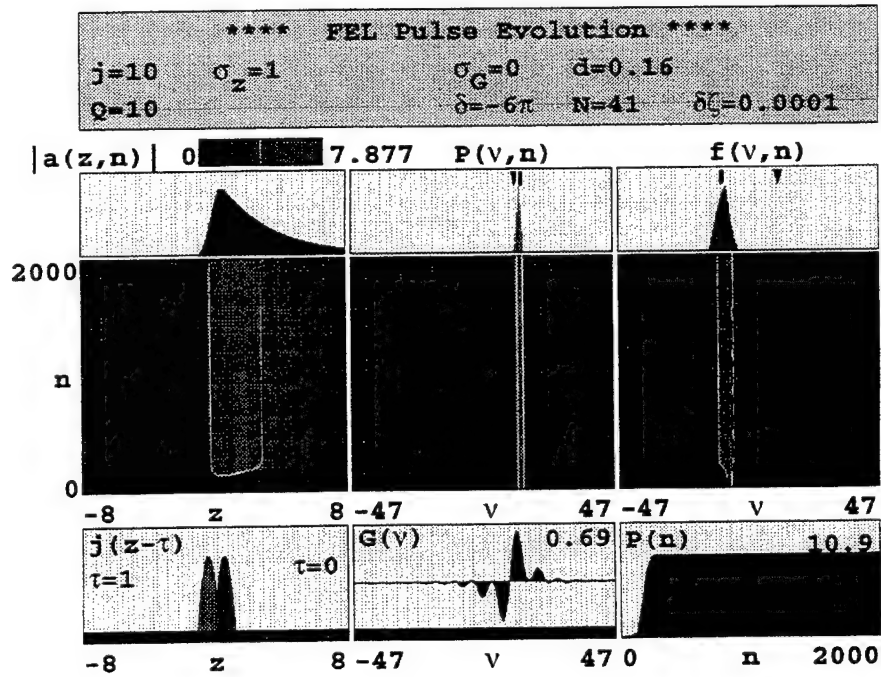
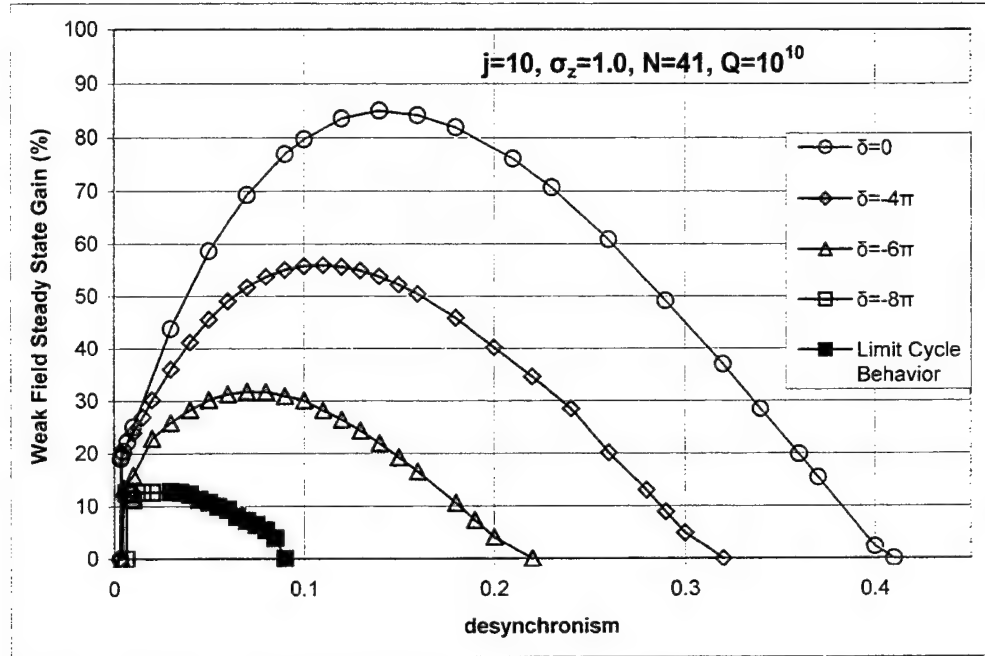


Figure 27. Pulse Evolution for  $\delta = -6\pi$  and  $d = 0.16$

Figure 28 shows the weak-field, steady-state gain as a function of desynchronism  $d$  and taper phase acceleration  $\delta$ . The gain is small for a small  $d$  and large  $d$  so that many passes are required to reach steady-state power. In the middle of  $d$  the gain is longer and simulations require a smaller number of passes. For  $\delta = 0$ , the maximum value of the weak-field, steady-state gain is  $G = 85\%$  at  $d = 0.14$ , for  $\delta = -4\pi$  is  $G = 56\%$  at  $d = 0.11$ , for  $\delta = -6\pi$  is  $G = 32\%$  at  $d = 0.07$  and for  $\delta = -8\pi$  is  $G = 13\%$  at  $d = 0.03$ .



**Figure 28. Weak Field Steady State Gain vs. Desynchronism for 34.5 MeV Energy Electron Pulses**

For  $\delta = -8\pi$  and for values of resonator losses factor above  $Q = 12$ , gain oscillations were observed between  $d = 0.03$  and  $d = 0.09$  with average modulation amplitude 13% of the average gain. The optical pulse becomes spatially modulated at the slippage distance, but there are no trapped electrons because the field is not strong. This is believed to be a new effect caused by the mode competition between the two

comparable peaks in the gain spectrum for  $\delta = -8\pi$ . The average values of the gain in limit cycle behavior region are indicated in Figure 28 with black squares. Figure 29 shows the oscillations in gain for  $\delta = -8\pi$  and  $d = 0.045$ .

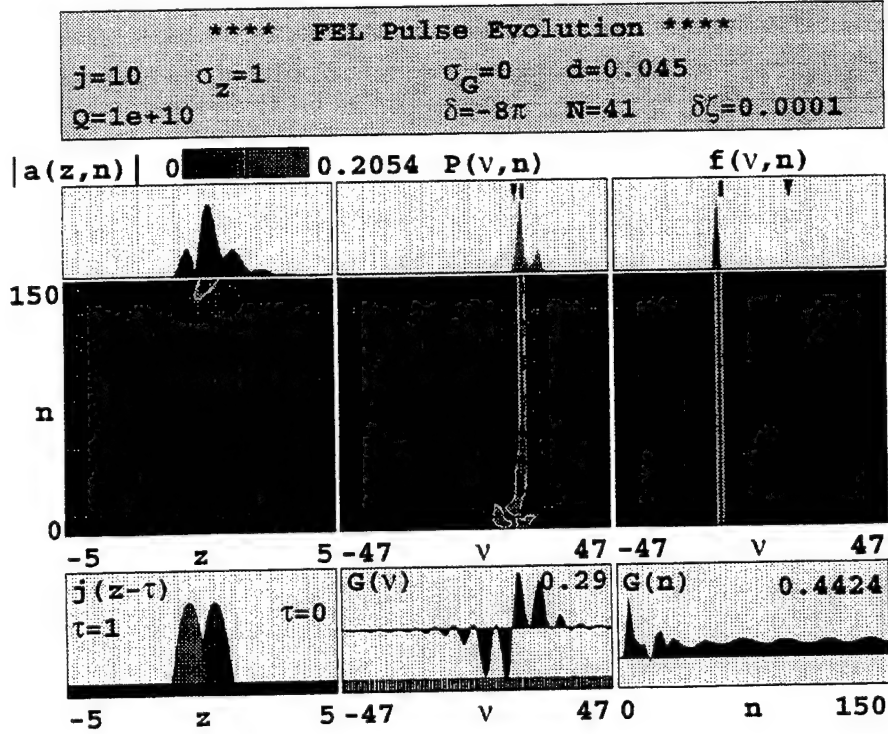


Figure 29. Weak Field Gain Oscillations for  $\delta = -8\pi$

Figures 31 and 32 show the induced electron energy spread  $\Delta\gamma/\gamma$ , as a function of desynchronism  $d$  and tapering rate  $\delta$ . The electron energy spread curves follow the trend of the power curves. For high power, there is a large energy spread. For  $\delta = 0$ , the maximum value is 8% at  $d = 0.004$ , for  $\delta = -4\pi$  the maximum value is 7.3% at  $d = 0.005$ , for  $\delta = -6\pi$  the maximum value is 6.3% at  $d = 0.008$ , and for  $\delta = -8\pi$  the maximum value is 4.8% at  $d = 0.0125$ . A goal of the TJNAF FEL is to keep  $\Delta\gamma/\gamma$  less than 6% in order to allow effective recirculation of the electron beam. The energy spread is less than 6% for



desynchronisms larger than  $d = 0.01$  for all the tapering rates  $\delta$ . The maximum power attained, with energy spread less than 6%, is  $P = 165$  for  $\delta = -4\pi$  at  $d = 0.01$ .

Figures 33 and 34 shows the optical spectrum width as a function of desynchronism  $d$  and tapering rate  $\delta$ . For  $\delta = 0$ , the maximum width is  $\Delta\nu = 35.02$  at  $d = 0.0038$ , for  $\delta = -4\pi$  the maximum width is  $\Delta\nu = 24.06$  at  $d = 0.006$ , for  $\delta = -6\pi$  the maximum width is  $\Delta\nu = 15.41$  at  $d = 0.008$ , and for  $\delta = -8\pi$  the maximum width is  $\Delta\nu = 16$  for  $d = 0.015$ . It can be seen that tapering reduces the optical spectrum width.

S. Benson, J. Gubeli, and G.R. Neil conducted experiments on TJNAF FEL oscillator with linear tapering using the same input data as our simulations. The results of their experimental study are described in Ref [12]. Figure 30 shows a comparison between the experimental and the simulation's FEL operating range in desynchronism as a function of the tapering rate  $\delta$ . The vertical axis plots the desynchronism curve width at taper  $\delta$  normalized to the desynchronism curve width at  $\delta = 0$ . As we see the results match experiment very well. This is an indication that the simulation results are valid.

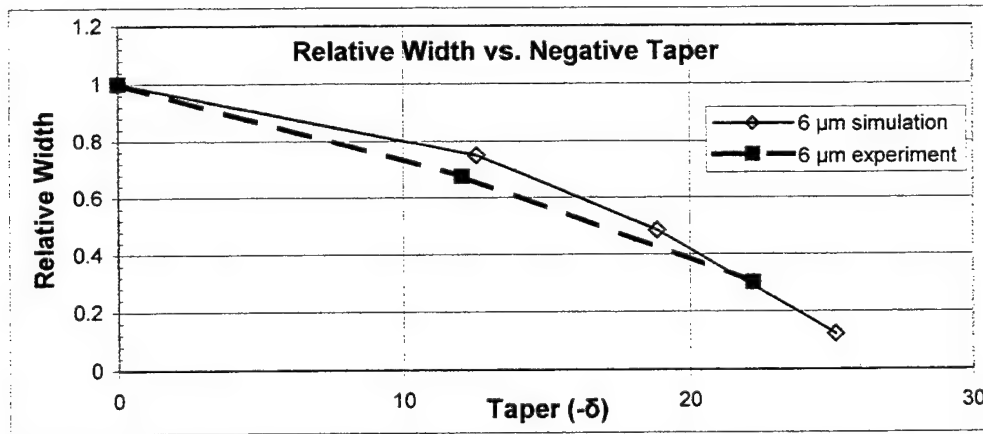


**Figure 30. Comparison Between Experimental and Simulation Operating Ranges**

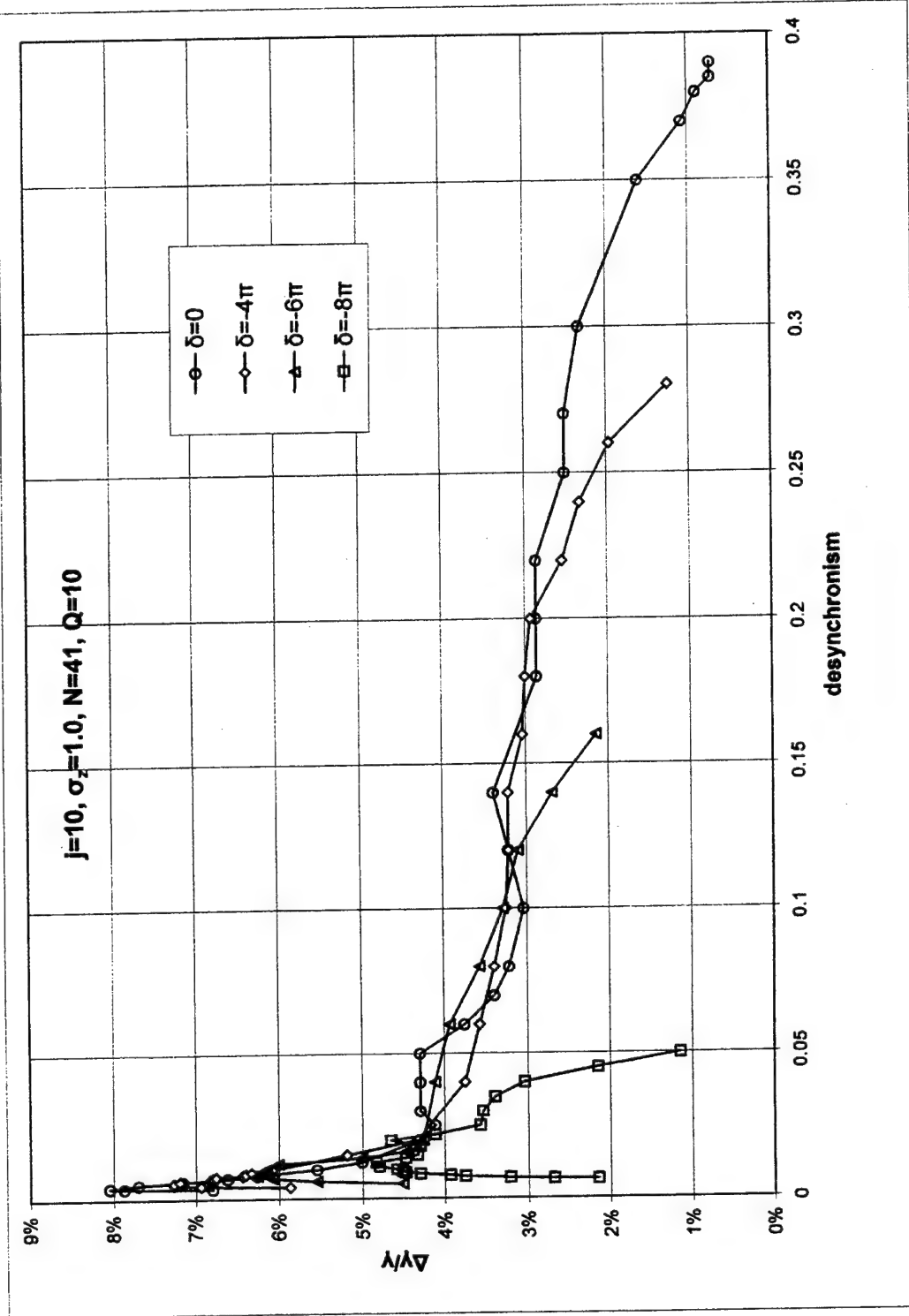
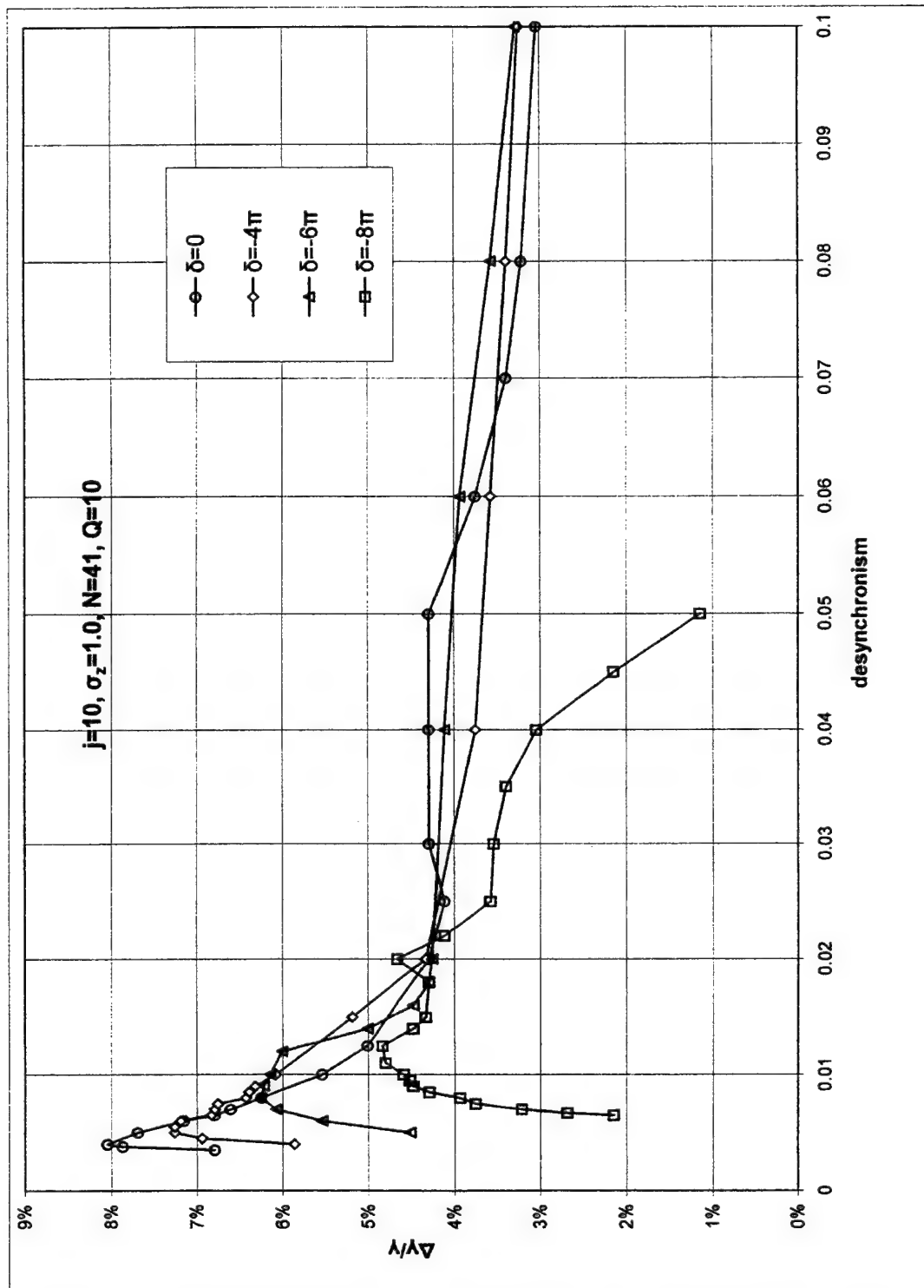


Figure 31. Electrons Energy Spread vs. Desynchronization for 34.5 MeV Energy Electron Pulses



**Figure 32. Close-up of Electrons Energy Spread vs. Desynchronism, from  $d = 0$  to  $d = 0.01$  for 34.5 MeV Energy Electron Pulses**

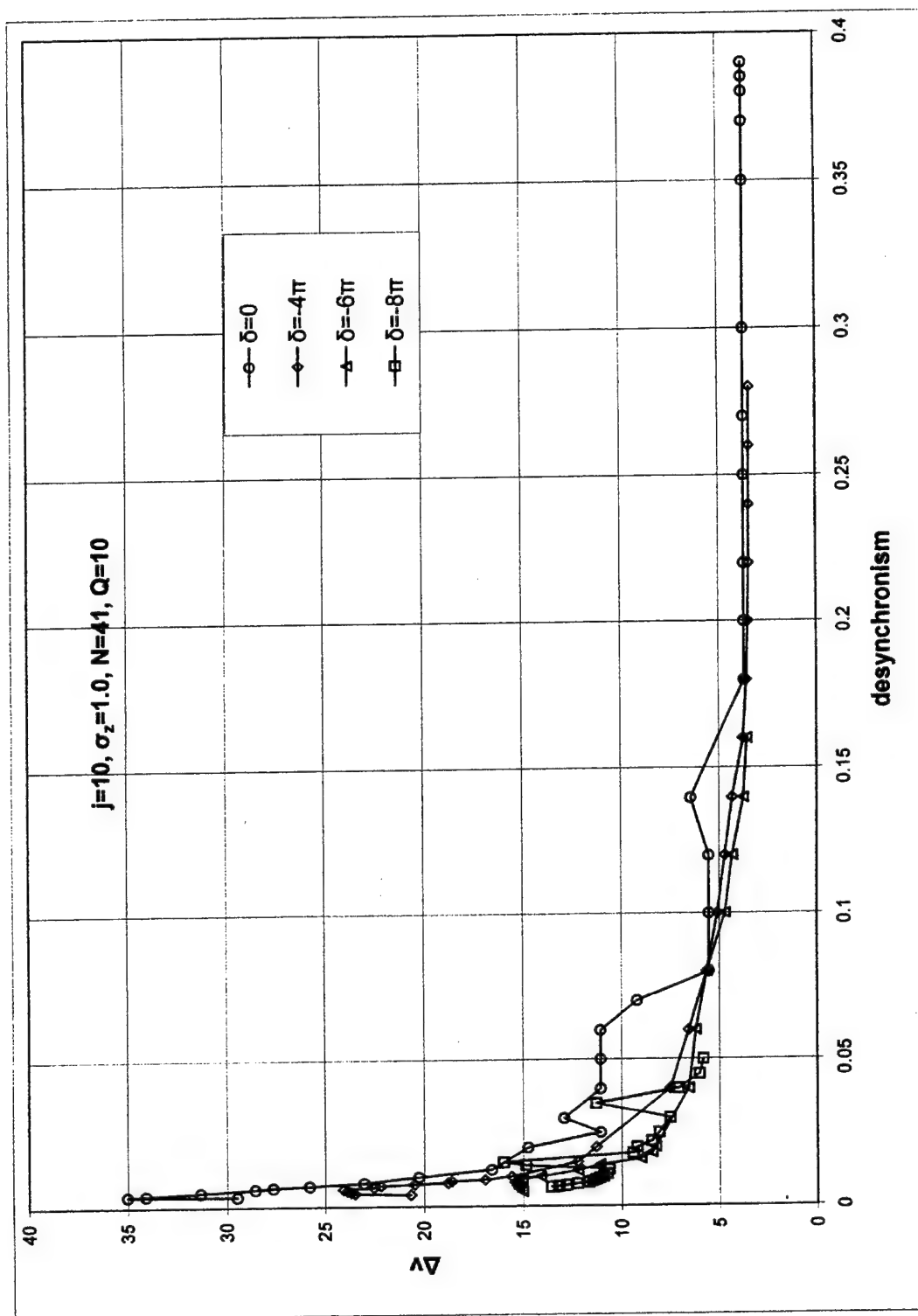


Figure 33. Optical Spectrum Width vs. Desynchronism for 34.5 MeV Energy Electron Pulses

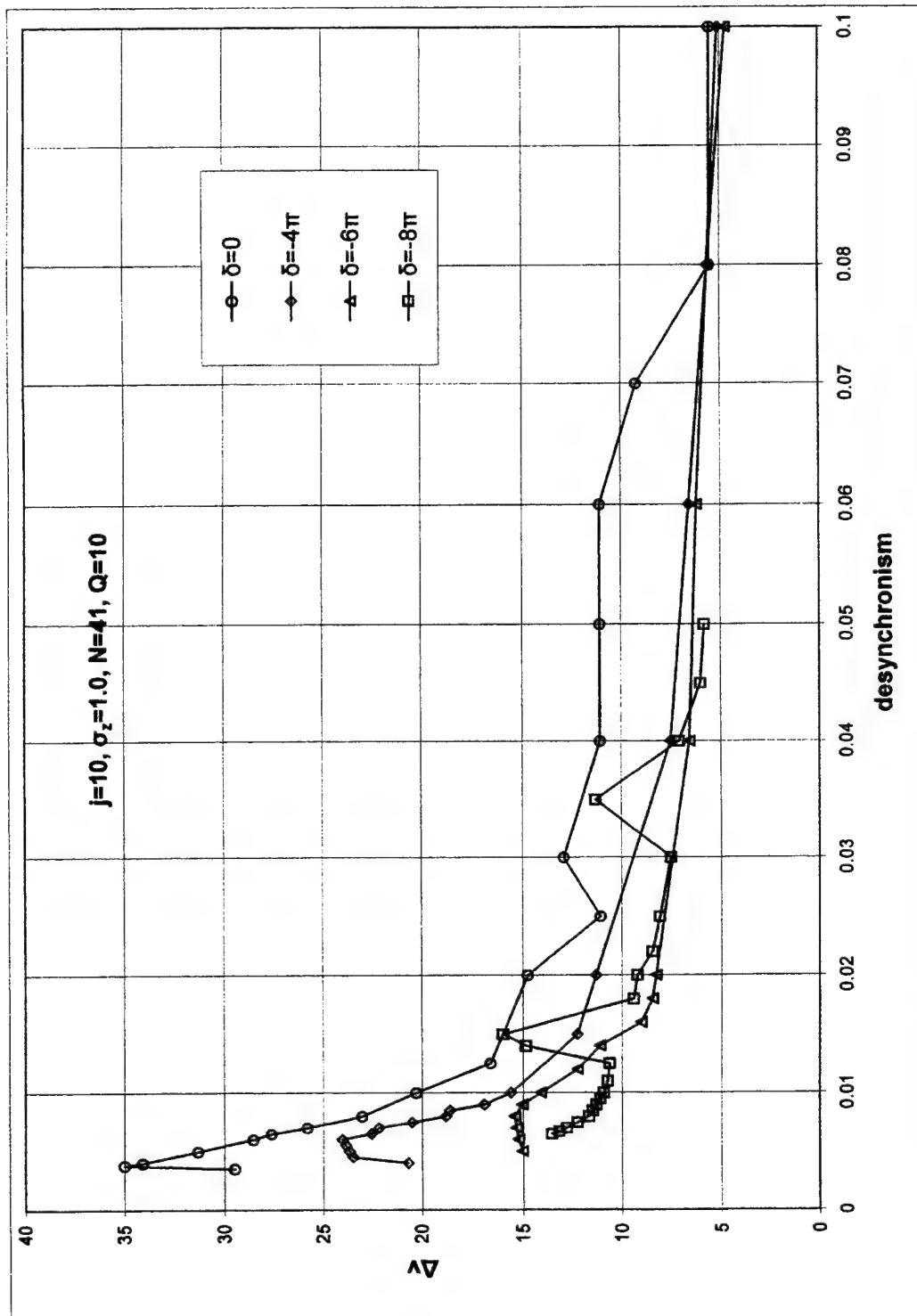


Figure 34. Close-up of Optical Spectrum Width vs. Desynchronism, from  $d = 0$  to  $d = 0.1$ , for 34.5 MeV Energy Electron Pulses

## 2. TJNAF FEL Simulation Results Using 47.5 MeV Energy Electron Pulses

Figure 35 shows the graph of the steady state power as a function of desynchronism  $d$  and taper phase acceleration  $\delta$ . For  $\delta = 0$ , the laser operating range is from  $d = 0.0038$  to  $d = 0.35$ , and reaches maximum power of  $P = 171$  at  $d = 0.0055$ . For  $\delta = -4\pi$  the laser operating range is from  $d = 0.0044$  to  $d = 0.27$ , and reaches maximum power of  $P = 180$  at  $d = 0.007$ . For  $\delta = -6\pi$ , the laser operating range is from  $d = 0.0055$  to  $d = 0.18$ , and reaches maximum power of  $P = 136$  at  $d = 0.025$ . Finally for  $\delta = -8\pi$ , the laser operating range is from  $d = 0.011$  to  $d = 0.055$ , and reaches maximum power of  $P = 78$  at  $d = 0.02$ .

The efficiency corresponding to the maximum values of steady state power are 1.39% for  $\delta = 0$ , 1.42% for  $\delta = -4\pi$ , 1.05% for  $\delta = -6\pi$ , and 0.64% for  $\delta = -8\pi$ . The untapered undulator gives the best performance, for large values of desynchronism  $d = 0.16$  to  $d = 0.35$ . A negative taper rate of  $\delta = -4\pi$  gives the highest power and stability in the rest of the operating range down to  $d = 0.16$ , which is a high power area.

The trapped-particle instability is evident again at high power. For  $\delta = 0$ , this occurs between the values of  $d = 0.038$  and  $d = 0.06$ , for  $\delta = -4\pi$  between  $d = 0.0044$  and  $d = 0.02$ , and for  $\delta = -6\pi$  between  $d = 0.0055$  and  $d = 0.02$ . For  $\delta = -8\pi$ , the maximum value of the optical field strength is  $a_0 = 24.8$  and there is no trapped-particle instability.

For  $\delta = 0$ , between the values of  $d = 0.0095$  and  $d = 0.065$ , limit cycle behavior is observed. The maximum modulation is 7.2% of the average power at  $d = 0.01$ , and the

minimum is 0.3% at  $d = 0.06$ . Black circles in Figure 35 indicate the average value of the power oscillation. Figure 36 shows the region of limit cycle behavior for  $\delta = 0$ .

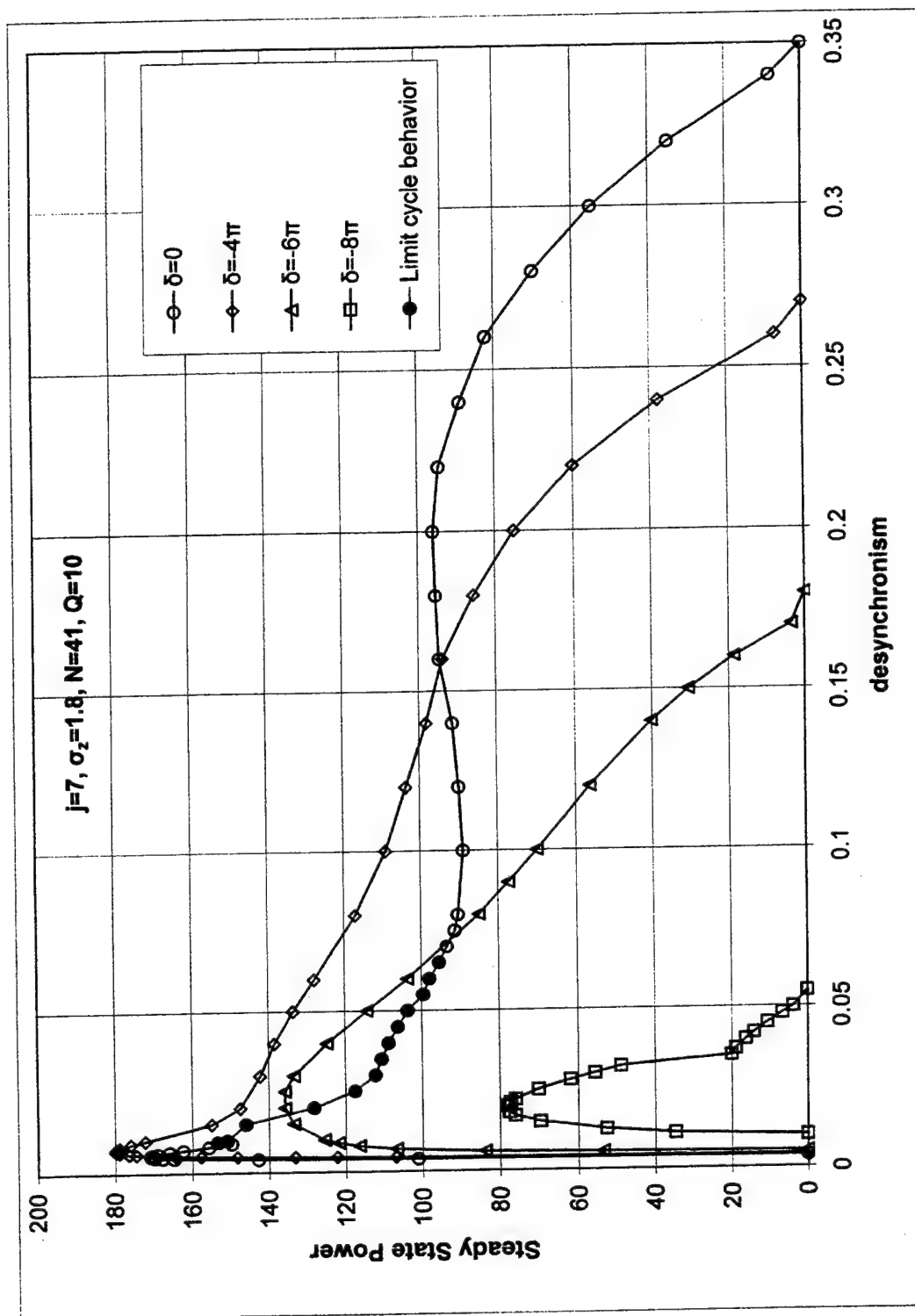
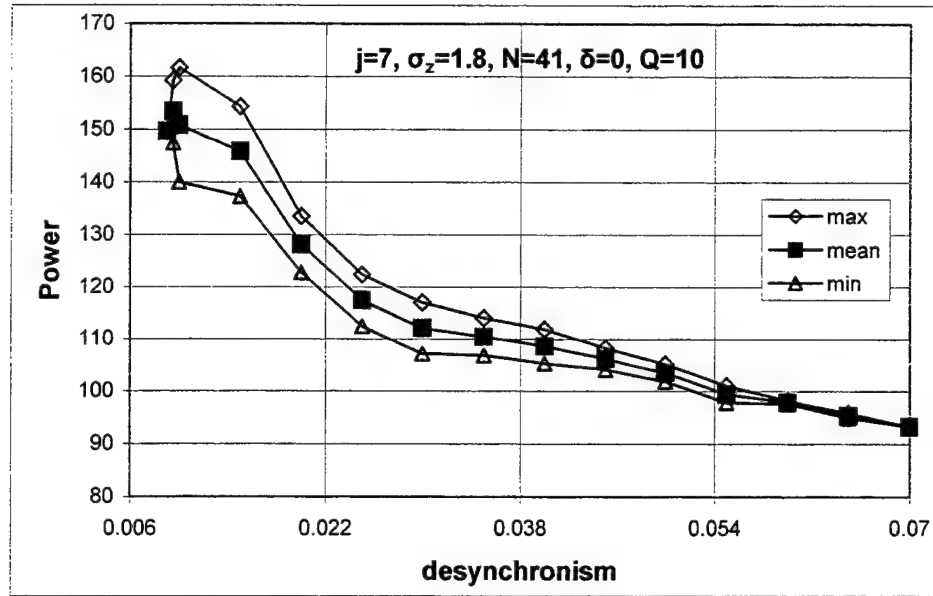


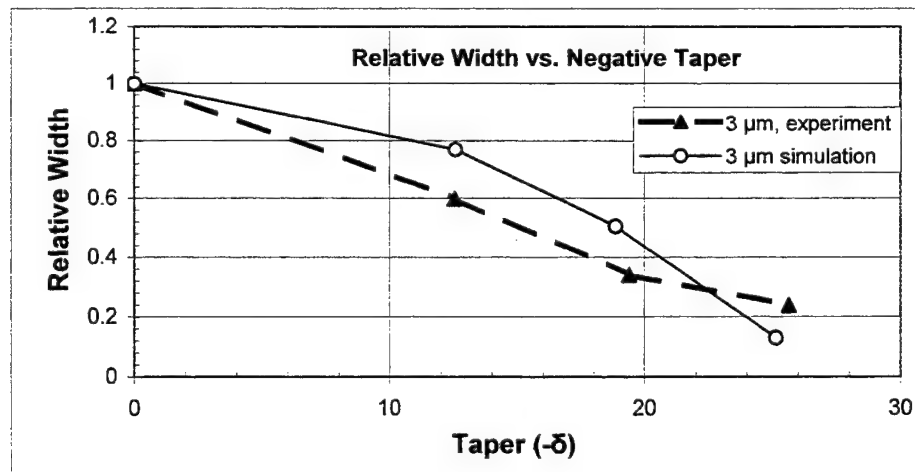
Figure 35. Steady-state Power vs. Desynchronism for 47.5 MeV Energy Electron Pulses





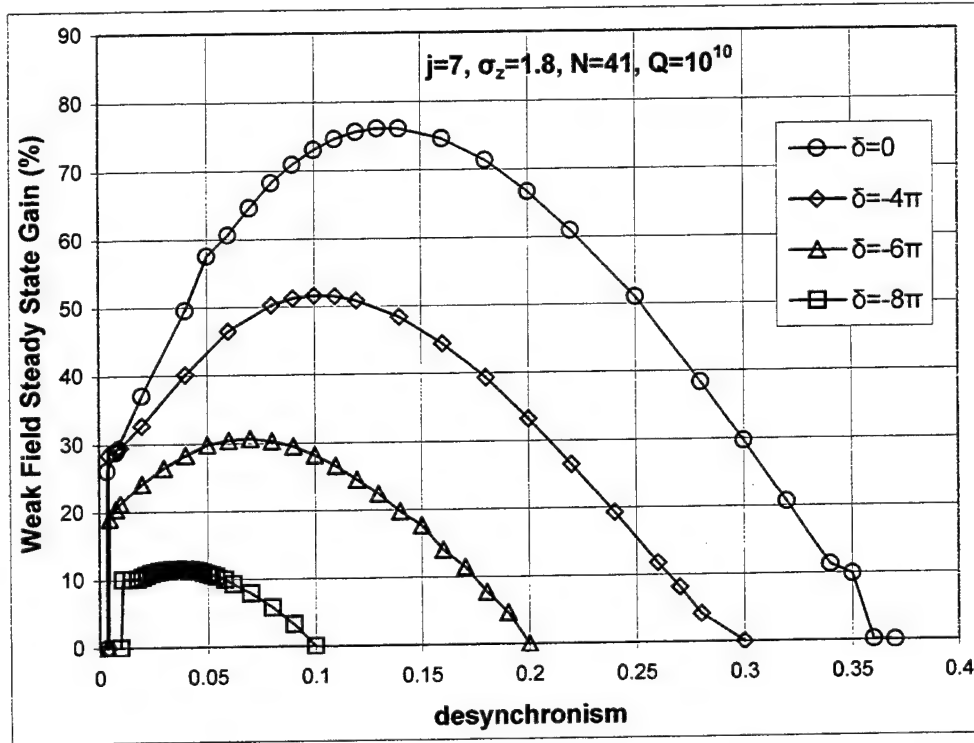
**Figure 36. Limit Cycle Behavior Region for  $\delta = 0$**

Figure 37 shows a comparison of relative width between the experiment and the simulation FEL operating ranges as a function of the tapering rate  $\delta$ . The experimental data came from Ref [12] and we see that again the results match, showing that experiments can be simulated leading to reliable conclusions.



**Figure 37. Comparison Between Experimental and Simulation Operating Ranges**

Figure 38 shows the weak-field, steady-state gain as a function of desynchronism  $d$  and taper phase acceleration  $\delta$ . For  $\delta = 0$ , the maximum value of the weak-field, steady-state gain is  $G = 76\%$  at  $d = 0.13$ , for  $\delta = -4\pi$  the maximum gain is  $G = 52\%$  at  $d = 0.1$ , for  $\delta = -6\pi$  the maximum gain is  $G = 31\%$  at  $d = 0.07$ , and for  $\delta = -8\pi$  the maximum gain is  $G = 12\%$  at  $d = 0.036$ .



**Figure 38. Weak-field, Steady-state Gain vs. Desynchronism for 47.5 MeV Energy Electron Pulses**

Figures 39 and 40 show the fractional electron beam energy spread,  $\Delta\gamma/\gamma$ , as a function of desynchronism  $d$  and tapering rate  $\delta$ . This energy spread is induced by the FEL interaction. For effective recirculation of the electron beam it is desirable to keep  $\Delta\gamma/\gamma$  less than 6%. The energy spread curves follow the same trend of the power curves. High optical power induces a larger energy spread. For  $\delta = 0$  the maximum value is 6.9%

at  $d = 0.0049$ , for  $\delta = -4\pi$  is 6.51% at  $d = 0.0052$ , for  $\delta = -6\pi$  is 5.5% at  $d = 0.007$ , and for  $\delta = -8\pi$  is 3.97% at  $d = 0.017$ . The energy spread is less than 6% for all values of  $d$  for  $\delta = -6\pi$  and  $\delta = -8\pi$ . For desynchronism larger than  $d = 0.007$  for  $\delta = 0$  and  $\delta = -4\pi$ , the energy spread is also less than 6%. The maximum power attained with less than 6% energy spread is  $P = 180$  for  $\delta = -4\pi$  at  $d = 0.0075$ .

Figures 41 and 42 show the optical spectrum width  $\Delta\nu$  as a function of desynchronism  $d$  and tapering rate  $\delta$ . For  $\delta = 0$ , the maximum width is  $\Delta\nu = 27$  at  $d = 0.004$ , for  $\delta = -4\pi$  the maximum width is  $\Delta\nu = 18$  at  $d = 0.0045$ , for  $\delta = -6\pi$  the maximum width is  $\Delta\nu = 13$  at  $d = 0.007$ , and for  $\delta = -8\pi$  the maximum width is  $\Delta\nu = 8.4$  for  $d = 0.011$ . It can be seen that tapering reduces the optical spectrum width, and high power increases the width.

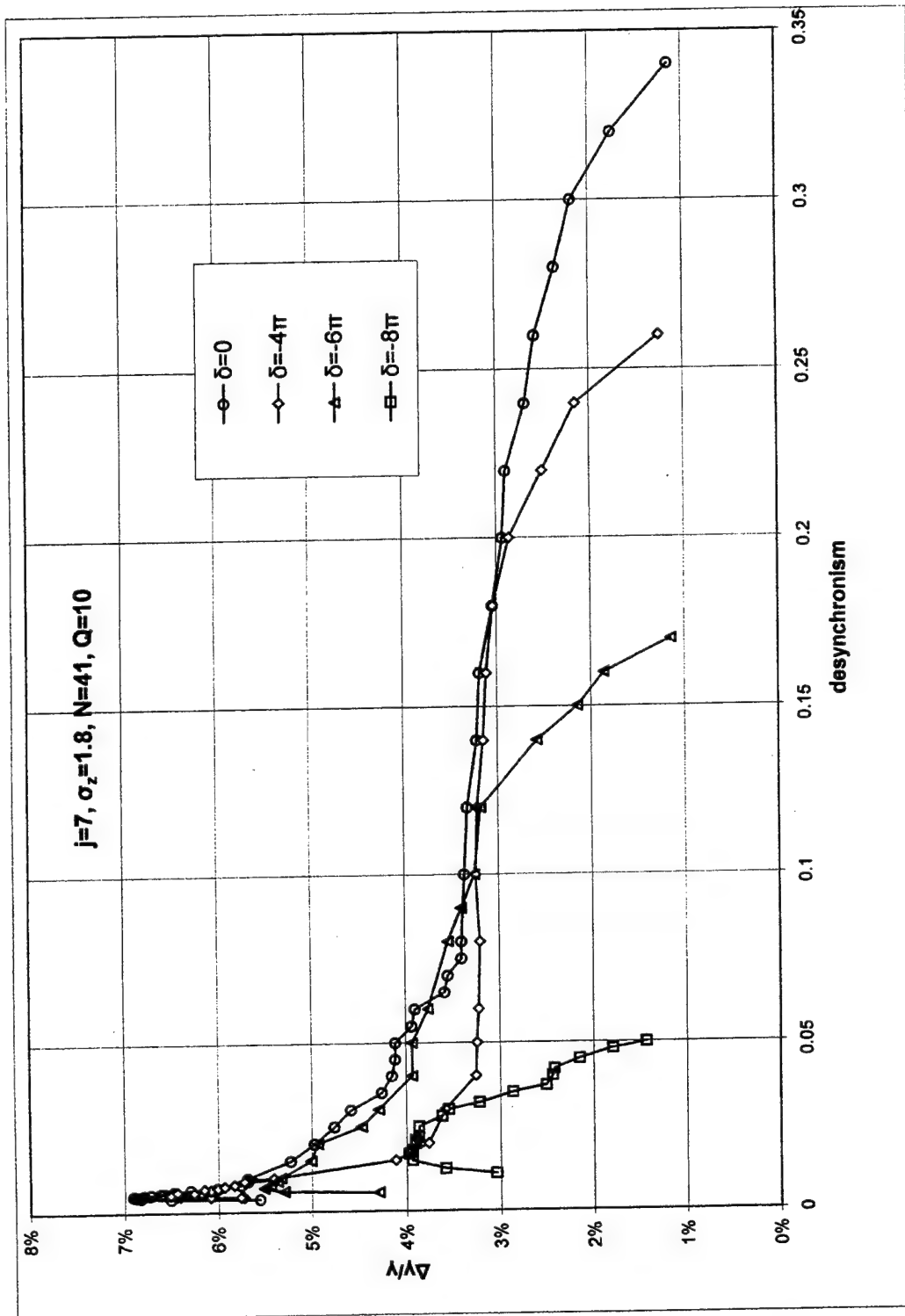


Figure 39. Electrons Energy Spread vs. Desynchronism for 47.5 MeV Energy Electron Pulses

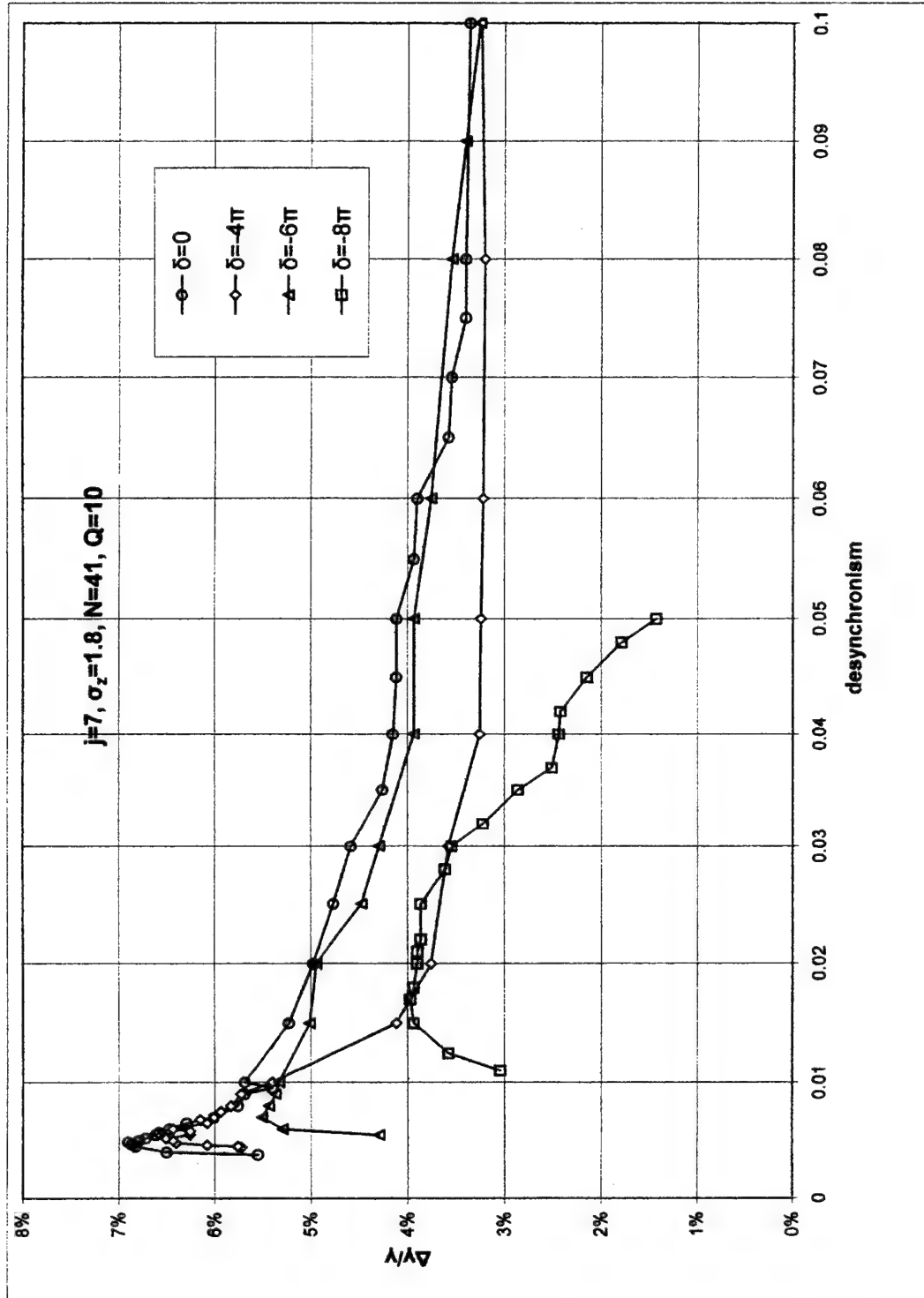


Figure 40. Close-up of Electrons Energy Spread vs. Desynchronism, from  $d = 0$  to  $d = 0.1$ , for 47.5 MeV Energy Electron Pulses

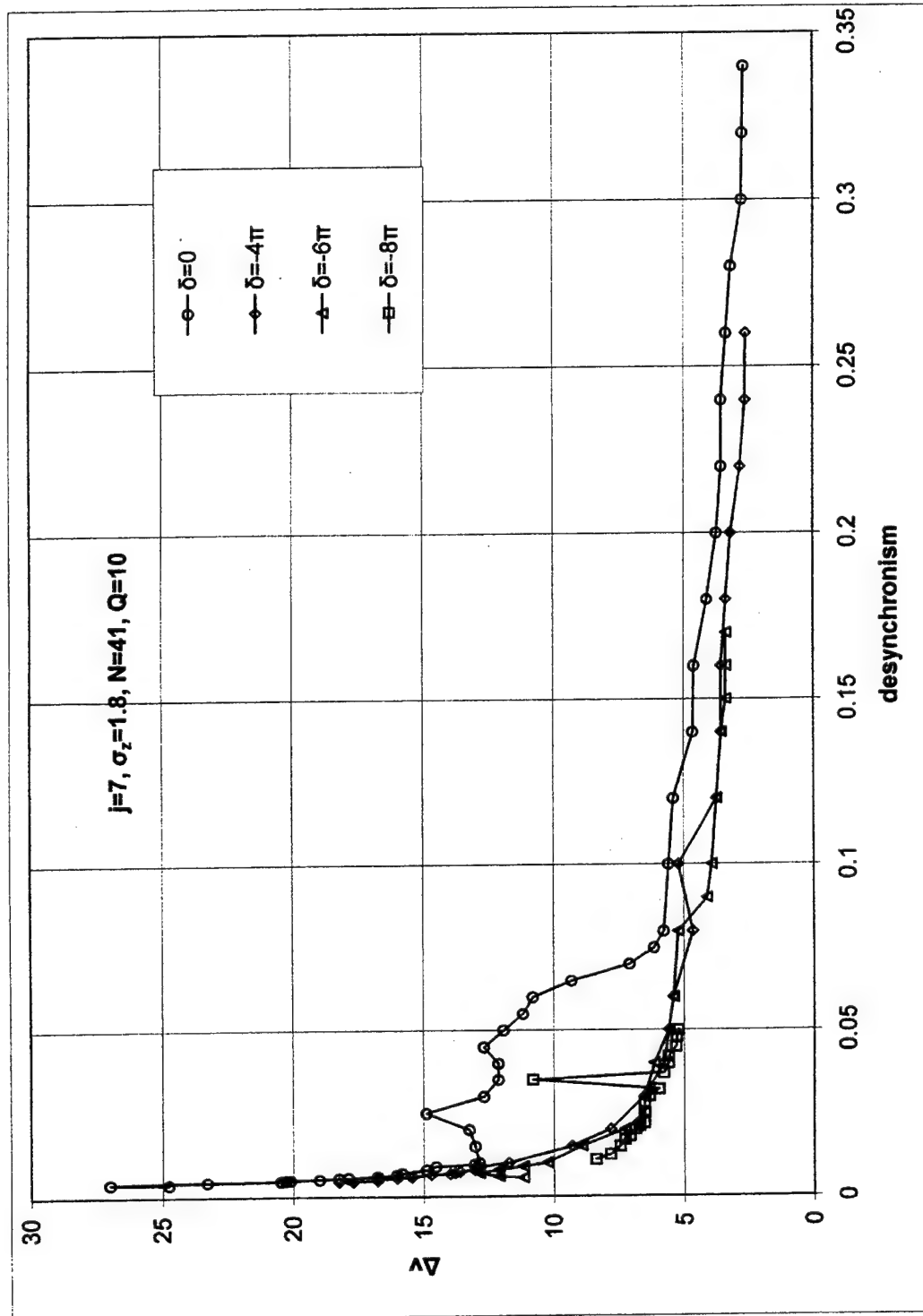


Figure 41. Optical Spectrum Width vs. Desynchronism for 47.5 MeV Energy Electron Pulses

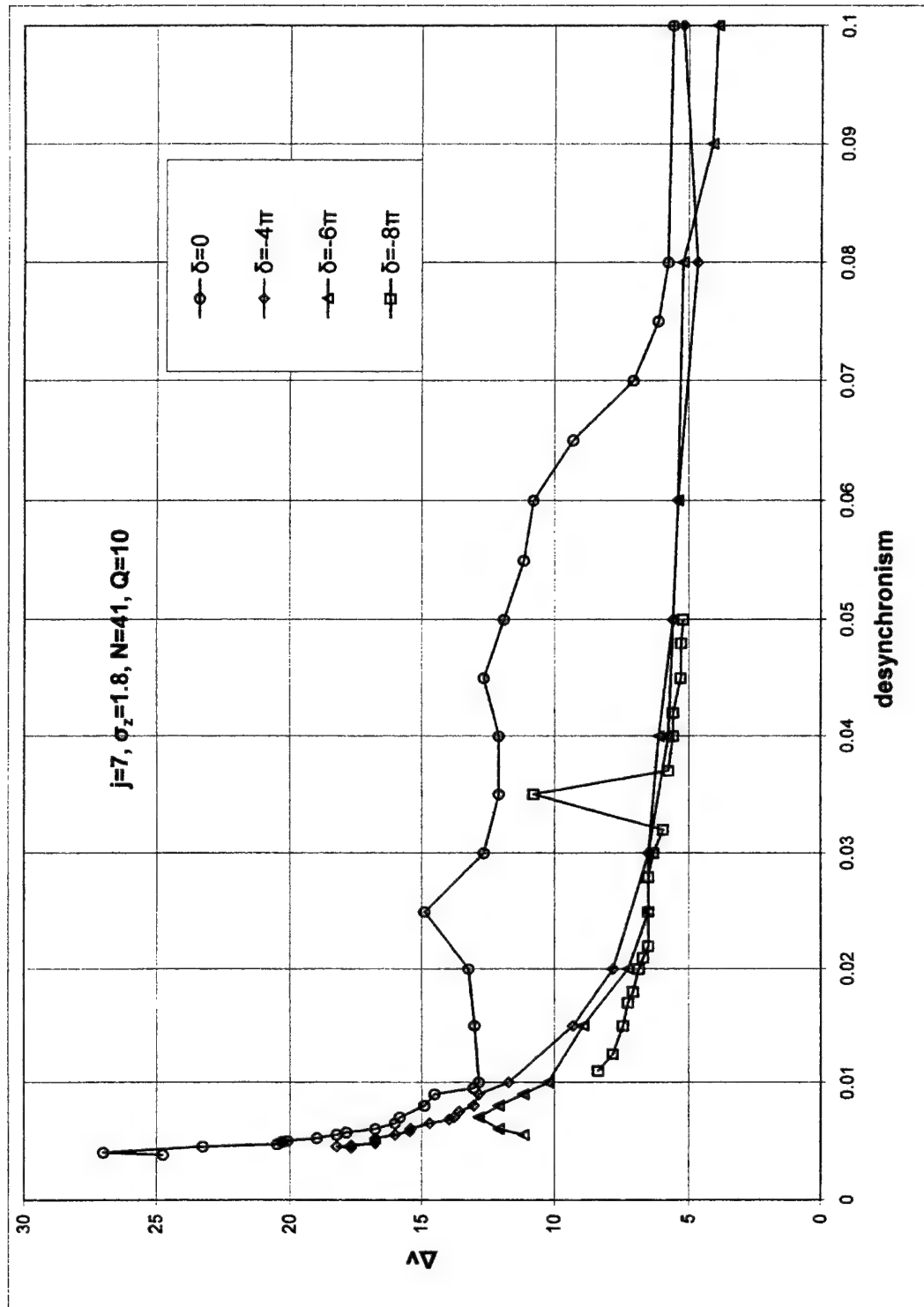


Figure 42. Close-up of Optical Spectrum Width vs. Desynchronism, from  $d = 0$  to  $d = 0.1$ , for 47.5 MeV Energy Electron Pulses

#### **IV. LASER PROPAGATION IN ATMOSPHERE AND INTERACTION WITH MATTER**

##### **A. ATMOSPHERIC COMPONENTS**

The atmosphere is gaseous and extends for several hundred kilometers above Earth. The gas of the atmosphere consists of elements and compounds. The exact composition varies with geographic location and altitude because both the atmospheric pressure and temperature change with the vertical structure of the atmosphere. The most common elements in the atmosphere are nitrogen and oxygen that constitute over 98% percent of the atmosphere by volume. Water vapor, carbon dioxide, nitrous oxide, carbon monoxide, and ozone are the major radiation absorbers. Water vapor has significant affect on absorption of infrared radiation. It is also the most variable because of the evaporation of water from bodies of water and condensation into clouds or dew. Carbon dioxide does not vary as much as does water vapor, but tends to be concentrated around large cities and heavy vegetation areas. Carbon dioxide is a strong absorber in the infrared wavelength range 3 to 5 $\mu$ m.

##### **B. ATMOSPHERIC TRANSMISSION**

In calculating the optical transmission of a laser radiation through the atmosphere, there are three primary processes that affect the radiation: absorption, scattering and refractive index fluctuations or turbulence. The atmospheric components discussed earlier are related to absorption and scattering, while the atmosphere's variations of



temperature, pressure and density contribute to turbulence. The effect of these factors is a reduction of the power of the laser irradiation that reaches the target.

Absorption and scattering are usually grouped together under the topic of extinction. Extinction is the attenuation in the amount of radiation passing through the atmosphere. Absorption is a process wherein a photon of radiation is absorbed by a gaseous molecule of the atmosphere, which translates to a temperature change. When radiation is scattered, the direction of the incident radiation is changed due to collision of a photon with an atmospheric molecule or particle. This process can be thought of as the atmospheric molecule captures the incident radiation momentarily and sends it unchanged in all directions.

To understand how the extinction affects transmission of radiation through the atmosphere, think of a single wavelength of incident radiation passing through an infinitesimal distance  $dx$ . The change in flux  $\Phi$  is

$$d\Phi = -\mu\Phi dx \quad (47)$$

where the incident radiation flux is represented by  $\Phi$  and  $\mu$  is the extinction coefficient.

The negative sign indicates the reduction of power from the absorption or scattering processes. In general, the extinction coefficient is made up of two components:

$$\mu = \varepsilon + \xi \quad (48)$$

where  $\varepsilon$  is the absorption coefficient and  $\xi$  is the scattering coefficient. Both the absorption and scattering coefficients depend on the incident wavelength. Because of the interaction of the incident radiation with the molecules of the atmosphere the radiation at

the output is changed to  $\Phi + d\Phi$ . After integrating Equation (1) it is found that the attenuation for a finite distance through a homogeneous medium is

$$\Phi = \Phi_0 e^{-\mu x} = \Phi_0 T$$

(49) where  $T = e^{-\mu x}$  is the transmittance of the atmosphere over a distance  $x$ . This principle is known as Beer-Lambert law. As it was mentioned above, the extinction coefficient is highly dependent on wavelength, so Beer's law is usually written as

$$T(\lambda) = e^{-\mu(\lambda)x} \quad (50)$$

Figure 43 shows the transmittance as a function of the wavelength for a horizontal path of 6000 ft at sea level and typical humidity. As we see the maximum transmittance occurs in the region 3 to 4.2  $\mu\text{m}$ . This explains why in the next chapter the irradiations were done at  $\lambda = 3.1 \mu\text{m}$  where the corresponding transmittance is  $T \cong 62\%$ .

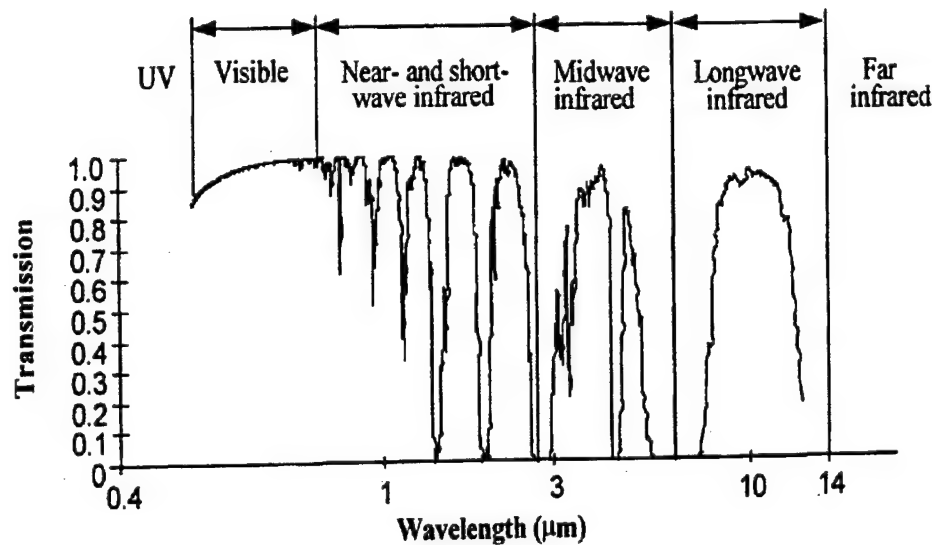


**Figure 43. Atmospheric Transmittance for a Horizontal Path of 6000 ft at Sea Level and Typical Humidity, From Ref. [5]**

### C. THERMAL DIFFUSION LENGTH

Suppose that a powerful laser that delivers sufficient amount of energy to the target has been built. Another parameter that has to be considered is the laser's spot size at the target. If this diameter of the spot is smaller than the thermal diffusion length of the material of the target, the material is able to diffuse the laser beam's incident energy away faster than the incoming energy can melt the material. The thermal diffusion length is characteristic for each material and determines its ability to absorb and transport heat for a given spot size.

Schriempf gives a detailed derivation of the thermal diffusion length [6]. He gives the definition of the thermal diffusion length,  $D$ , as the distance required for the temperature to drop to  $1/e$  of the initial value. The formula that gives the thermal diffusion length is

$$D = 2\sqrt{\kappa \cdot t_D}, \quad (51)$$

where

$$t_D = \frac{\pi F^2 \Delta T^2}{4\Phi_0^2 \kappa}.$$

(52) is the time required to raise the material's temperature from ambient to melting ( $\Delta T$ ),  $F$  is the thermal conductivity,  $\Phi_0$  is the initial radiative flux and  $\kappa = F / \rho_{FS} C$  is a constant where  $\rho_{FS}$  is density and  $C$  is the specific heat.

In the next chapter, we are going to describe the damage produced on Slip-cast Fused Silica samples, so we calculate the thermal diffusion length for this material. The

material density is  $\rho_{FS} = 2200 \text{ Kg/m}^3$ , the specific heat is  $C = 920 \text{ J/Kg-K}$ , the thermal conductivity is  $F = 1.26 \text{ W/m-K}$ , the initial power density is  $\Phi_0 = 10^8 \text{ W/m}^2$  and the melting temperature of the material is  $T_m = 1980 \text{ K}$ . Using these values in Equation (5) it is found that the thermal diffusion length for Slip-cast fused Silica is  $D = 0.021 \text{ mm}$ . In order to minimize thermal diffusion and melt the material, the laser spot size on the target must have diameter larger than the thermal diffusion length calculated above. This was attained in all the irradiations that were done on the samples.

#### D. SCALING

Experiments indicate that the typical average power density required to kill an incoming missile is about  $10 \text{ kW/cm}^2$  over a spot area of  $100 \text{ cm}^2$ . That means that the energy that must reach the missile is about  $P = (10 \text{ kW/cm}^2) \cdot 100 \text{ cm}^2 = 1 \text{ MW}$ . Considering atmospheric extinction, more energy is necessary at the laser to obtain the required energy at the target. However the cost of creating such a powerful laser is extremely high, and in order to come to safe conclusions about its effectiveness, we must do several experiments using the existing lower power FEL.

The TJNAF FEL is capable of several hundred watts average power and developments are being made to be upgraded to operate at  $10 \text{ kW}$  average power in the near future. Using the existing power, we can simulate the power density of  $10 \text{ kW/cm}^2$  by focusing the beam to smaller spot sizes, and evaluating the damage to different sample materials. Thus in the future, we are going to be able to develop scaling rules that will

allow us to estimate the damage that a large laser produces without spending enormous amount of money building the laser first.

## V. FEL DAMAGE EXPERIMENTS

### A. EXPERIMENTAL PROCEDURE

Two experiments took place at TJNAF on slip-cast fused silica samples on August 9, 1999 and March 14, 2000 by the TJNAF personnel [1],[2]. In the next few paragraphs, the experimental procedures are described the irradiation results are analyzed.

In the experiment of August 9, 1999 two samples were irradiated through a calcium fluoride lens with a measured back length of 137.6 mm. The laser beam wavelength was  $\lambda=3.10\text{ }\mu\text{m}$ , the pulse repetition frequency (PRF) was 18.7 MHz and the power meter in the optics control room indicated a power of  $105 \pm 5\text{ W}$ . The first sample was placed 20.7 cm from the back surface of the lens. At this position, the calculated waist radius of the beam was 0.25 cm, with a corresponding average intensity of  $490\text{ W/cm}^2$ . Three irradiations with no airflow were done, and then the sample was moved to irradiate fresh areas, the airflow was turned on, and three more irradiations were done. The airflow was blowing across the front face of the sample at an angle of  $\theta = 90^\circ$  with respect to the irradiation line. An Oregon Scientific anemometer was used, which indicated a wind speed of 60 mph. The irradiation exposure time was 5 seconds.

After finishing the above irradiations, a new sample was used. The sample was moved in a new position in order to achieve a beam waist radius of 0.087 cm, which yields to an average intensity of  $10\text{ kW/cm}^2$ . The same irradiation schedule was followed. The irradiation exposure time was again 5 seconds.

In the experiment of March 14, 2000, another sample was irradiated through a calcium fluoride lens with a measured back length of 235.7. The laser beam wavelength was  $\lambda = 3.10 \mu\text{m}$ , the PRF was 37.4 MHz and the power meter in the optics control room indicated a power of  $500 \pm 10 \text{ W}$ . The sample was placed 217.0 mm from the back surface of the lens. At this position, the calculated waist radius of the beam was 0.12 cm, with a corresponding average intensity of  $10 \text{ kW/cm}^2$ . One irradiation with no airflow was done, and then the sample was moved to fresh areas, the air was turned on, and one more irradiation was done. The air was blowing across the front face of the sample at an angle of  $\theta = 90^\circ$  with respect to the irradiation line. An Oregon Scientific anemometer was used, which indicated a wind speed of 83 to 86 mph. The irradiation exposure time was 5 seconds.

## **B. DESCRIPTION OF RESULTS**

The Naval Research Laboratory (NRL) provided the Slip-cast Fused Silica samples. The samples #1 and #2 were new and were used in experiments for the first time. The sample #3 had been used in the past, and carried eight irradiations from a previous experiment.

### **1. Slip-cast Fused Silica Sample #1**

The sample is 2.2 cm by 7.4 cm and has a variation in thickness from 0.9 to 1.9 cm. It was used for the experiments conducted on August 9, 1999. Figure 44 shows two sets of three irradiations done on the front face of the sample. The lower set of irradiations was done while air was blowing across the front surface of the sample, and

the upper set without air. Table 4 shows the data and the results of these irradiations.

Run number 1,2 and 3 refer to the upper set of irradiations, and 4,5 and 6 to the lower set from left to right.

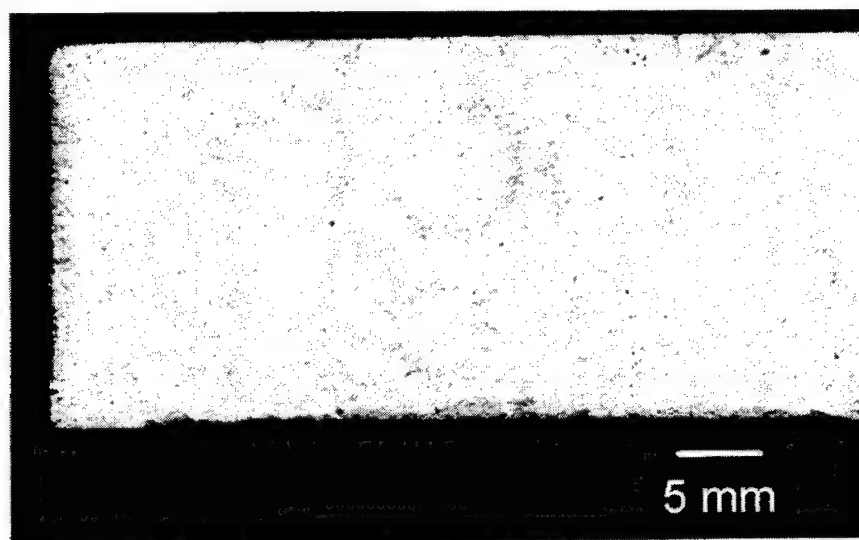


**Figure 44. Slip-cast Fused Silica Sample #1**

Run Number	Wavelength ( $\mu\text{m}$ )	PRF (MHz)	Airflow (mph)	Average Power (Watts)	Average Intensity ( $\text{W}/\text{cm}^2$ )	Laser Beam Diameter (mm)	Damage Diameter (mm)
1	3.10	18.7	No	105	490	5	6.2
2	3.10	18.7	No	105	490	5	6.5
3	3.10	18.7	No	105	490	5	6.0
4	3.10	18.7	60	105	490	5	5.0
5	3.10	18.7	60	105	490	5	5.0
6	3.10	18.7	60	105	490	5	5.5

**Table 4. Irradiation Data of Slip-cast Fused Silica Sample #1, After Ref. [1]**



The exposure time of the above irradiations was 5 seconds and as we can see from the PRF, the energy per pulse was twice that of the measurements made in March 99. The damage diameters were measured using an optical microscope. Due to the low average intensity ( $490\text{W}/\text{cm}^2$ ), we observed only faint circular profiles on the sample material after the irradiations, whose diameters matched the calculated beam diameter reasonably. The damage was just superficial. The effect of the airflow was to decrease the diameter of the damage area. Figure 45 shows a close up of damage in Run 2.

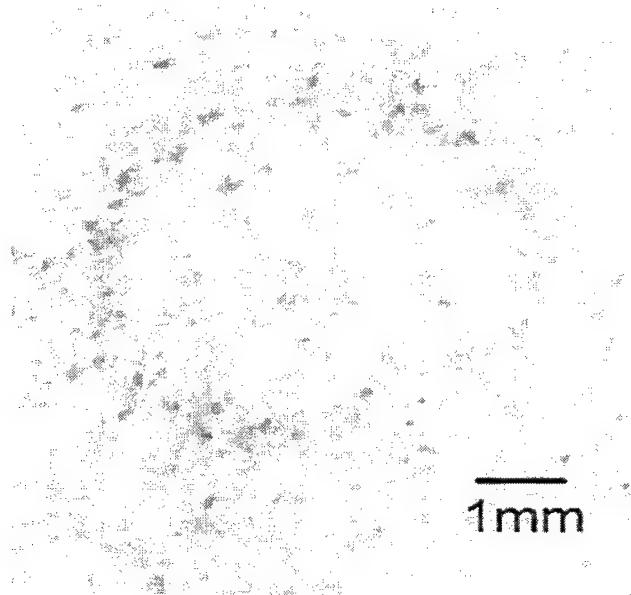


**Figure 45. Close-up Damage to Slip-cast Fused Silica in Run 2**

## **2. Slip-cast Fused Silica Sample #2**

The sample is 2.2 cm by 7.4 cm and has a variation in thickness from 0.9 to 1.9 cm. It was used for the experiments conducted on August 9, 1999. Figure 46 shows the irradiations done on the front face of the sample and Table 5 the corresponding data.

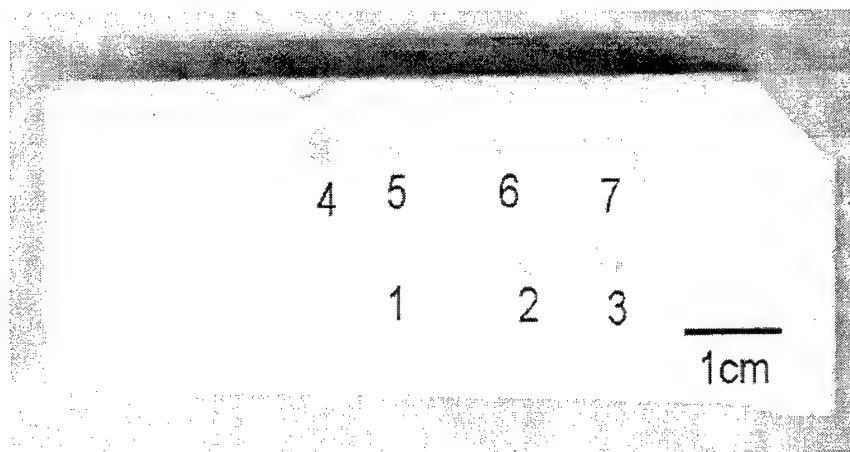


**Figure 46. Slip-cast Fused Silica Sample #2**

Run Number	Wavelength ( $\mu\text{m}$ )	PRF (MHz)	Airflow (mph)	Average Intensity ( $\text{kW}/\text{cm}^2$ )	Laser Beam Diameter (mm)	Damage Diameter (mm)	Penetration Rate (mm/s)
1	3.10	18.7	No	10	1.76	3.8	0.29
2	3.10	18.7	No	10	1.76	3.5	0.30
3	3.10	18.7	No	10	1.76	3.5	0.32
4	3.10	18.7	60	10	1.76	3	0.34
5	3.10	18.7	60	10	1.76	3	0.33
6	3.10	18.7	60	10	1.76	2.5	0.31
7	3.10	18.7	No	10	1.76	3.9	0.29

**Table 5. Irradiation Data of Slip-cast Fused Silica Sample #2, After Ref. [1]**

The exposure time for the above irradiations was 5 seconds and the average power was 105 Watts. The average damage diameter, for the irradiations done in the presence

of airflow, was 2.83 mm and for those without airflow was 3.67 mm. Thus, it can be seen that again the damage diameters matched the calculated beam diameters reasonably, and the effect of the presence of air was to decrease the diameter of the damaged area. No burn-through occurred during the irradiations. The damage produced on the sample had the shape of small circular crater. The areas around the craters were clean of debris. Part of the melted material was evaporated during the irradiation, and the rest of it remained inside the crater.

The average penetration rate, for the irradiations done in the presence of airflow, was 0.326 mm/s and for those without airflow was 0.3 mm/s. The presence of airflow slightly increased the penetration rate.

Figure 47 shows the effects of the exposure time on penetration depth rate, of an older experiment conducted on a sample of Slip-cast Fused Silica.

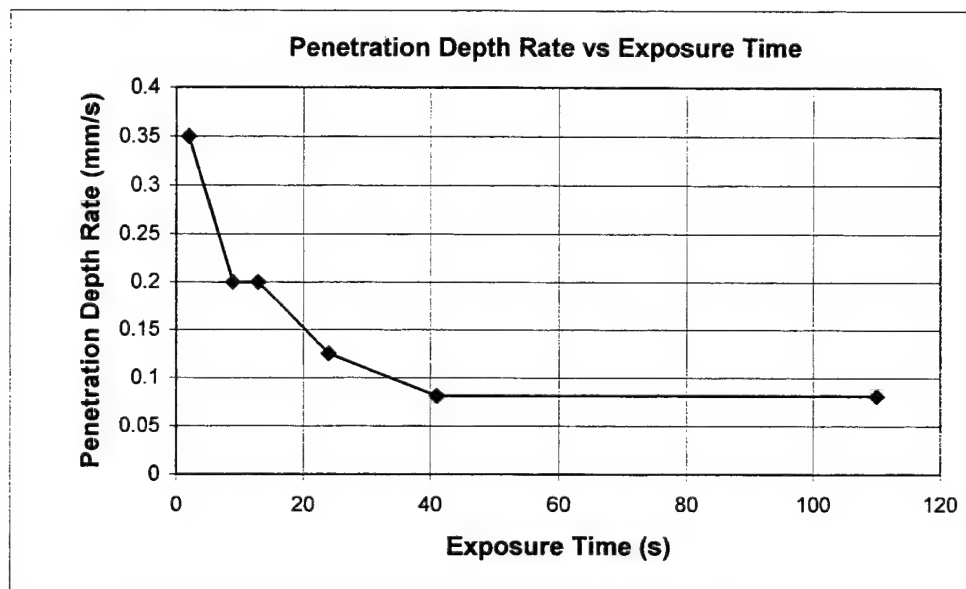


**Figure 47. Exposure Time vs. Penetration Rate for Fused Silica, From Ref. [3]**

The average power of that experiment was  $100 \text{ to } 103 \text{ W} \pm 5 \text{ W}$ , the wavelength  $\lambda = 4.825 \text{ } \mu\text{m}$ , the average intensity  $10 \text{ kW/cm}^2$  and the PRF  $37.4 \text{ MHz}$ . As it can be seen from Figure 4, the penetration depth rate that corresponds to exposure time 5 seconds is  $0.26 \text{ mm/s}$ . Therefore when the PRF is  $18.7 \text{ MHz}$  and the wavelength is  $\lambda = 3.10 \text{ } \mu\text{m}$ , the penetration rate is bigger either with the presence of airflow or without it. It is true that when the PRF is lower there is higher fluence per pulse and thus intensity per micropulse, but we can't tell for sure if this improvement in the penetration rate is due to the different wavelength or the PRF.

In the future, it might be interesting to conduct experiments changing just one parameter in each experiment so that we can evaluate better the effect of each of them. It would also help in scaling, if in each experiment we plot curves of exposure time vs. penetration depth rate. Figure 48 shows a close-up of damage in Run 4.

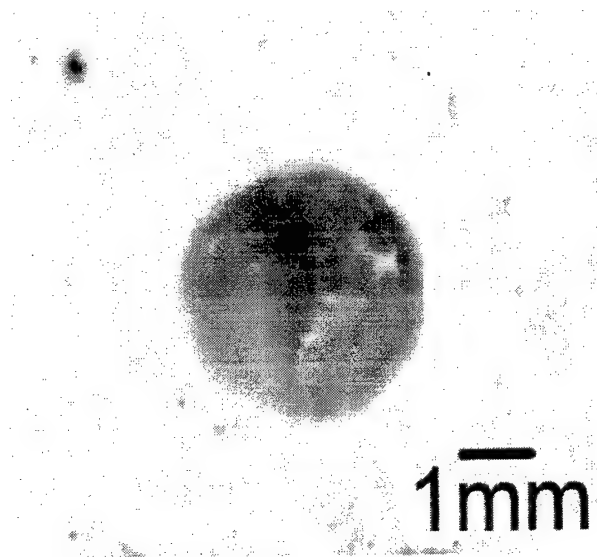


**Figure 48. Close-up of Damage of Slip-cast Fused Silica in Run 4**

### 3. Slip-cast Fused Silica Sample #3

The sample is 6.9 cm by 7.4 cm and has a variation in thickness from 0.9 to 1.9 cm. It was used for the experiments conducted on March 14, 2000. Figure 49 shows the irradiations done on the front face of the sample and Table 6 the corresponding data.

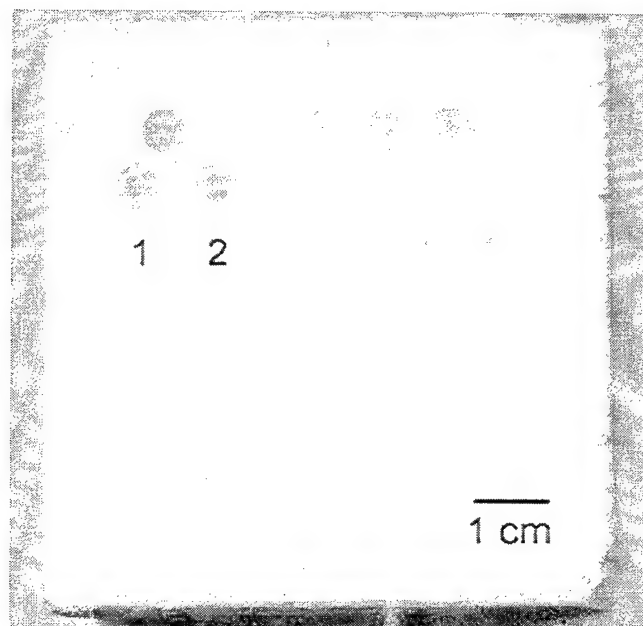


**Figure 49. Slip-cast Fused Silica Sample #3**

Run Number	Wavelength ( $\mu\text{m}$ )	P.R.F. (MHz)	Airflow (mph)	Average Intensity ( $\text{kW}/\text{cm}^2$ )	Laser Beam Diameter (mm)	Damage Diameter (mm)	Penetration Rate (mm/s)
1	3.10	37.425	83-86	10	2.4	4.4	1.32
2	3.10	37.425	No	10	2.4	5.6	7.5

**Table 6. Irradiation Data of Slip-cast Fused Silica Sample #3, After Ref. [2]**

The average power was 500 Watts and burn-through of the material occurred during the above irradiations. The burn-through time for Run 1 was 6.8 seconds and for Run 2 was 1.2 seconds. In Run 1, the damage diameter on the front face of the material sample was 4.4 mm, and on the back face was 3.1 mm. In Run 2, the damage diameter on the front face was 5.6 mm and on the back face 1.8 mm. It can be seen that the effect of airflow was to reduce the front face damage diameter and to increase the burn-through time.

It can also be seen that the back face damage diameters of the material sample are smaller than the front face. There are three reasons that explain why this happens. The first reason is that the beam profile follows the Gaussian distribution, with the highest intensity in the center of the beam and intensity down by  $1/e$  at the beam radius. The second reason is the position of the sample. The sample is 9 mm thick and was located during the irradiations 217.0 mm from the back surface of the lens while the back focal length of the lens was 235.7 mm. It was 18.7 mm from the focus, so the beam size is decreasing as it proceeds through the material. The third reason is that the front surface is exposed to irradiation for longer time than the back.

Since burn through occurred, we have the opportunity to have a better view of the damage and extract some extra data about it. The volume of the total damaged region in Run 1 (labeled  $IT$ ) is estimated by

$$V_{IT} = \int_0^{9mm} \pi \cdot R_{IT}^2(z) \cdot dz, \quad (53)$$

where  $z$  is the material thickness and the radius changes approximately linearly as

$$R_{1T}(z) = 2.2\text{mm} - 0.072 \cdot z[\text{mm}]. \quad (54)$$

The volume of the total damaged region in Run 2 (labeled 2T) is estimated by

$$V_{2T} = \int_0^{9\text{mm}} \pi \cdot R_{2T}^2(z) \cdot dz, \quad (55)$$

where the radius changes approximately linearly as

$$R_{2T}(z) = 2.8\text{mm} - 0.211 \cdot z[\text{mm}]. \quad (56)$$

When we say entire damaged region, we mean both the hole and the melted and rehardened portion. After doing the above calculations the volume of the entire damage region in Run 1 is  $V_{1T} = 100 \text{ mm}^3$  and in Run 2 is  $V_{2T} = 105 \text{ mm}^3$ . Knowing that the density of the fused silica is  $\rho_{FS} = 2.2 \text{ gm/cm}^3$ , the mass of the entire damaged region in Run 1 is  $m_{1T} = 0.221 \text{ gm}$  and in Run 2 is  $m_{2T} = 0.232 \text{ gm}$ .

The volume of the hole in Run 1 (labeled 1H) is estimated by

$$V_{1H} = \int_0^{9\text{mm}} \pi \cdot R_{1H}^2(z) \cdot dz, \quad (57)$$

where the radius changes approximately linearly as

$$R_{1H}(z) = 1.6\text{mm} - 0.1167 \cdot z[\text{mm}]. \quad (58)$$

The volume of the hole in Run 2 (labeled 2H) is estimated by

$$V_{2H} = \int_0^{9\text{mm}} \pi \cdot R_{2H}^2(z) \cdot dz, \quad (59)$$

where the radius changes approximately linearly as

$$R_{2H}(z) = 0.75\text{mm} - 0.0444 \cdot z[\text{mm}]. \quad (60)$$

From the above calculations the volume of the hole in Run 1 is  $V_{1H} = 35 \text{ mm}^3$  and

in Run 2 is  $V_{2H} = 8.9 \text{ mm}^3$ . The density of the fused silica is  $\rho_{FS} = 2.2 \text{ gm/cm}^3$ , so the mass of the material removed creating a hole in Run 1 is  $m_{1H} = 0.078 \text{ gm}$  and in Run 2 is  $m_{2H} = 0.020 \text{ gm}$ .

What it is seen from these calculations is that the damaged regions, either with or without the presence of airflow, have approximately the same volume ( $V_{1T} = 100 \text{ mm}^3$  and  $V_{2T} = 105 \text{ mm}^3$ ). The basic effect of the airflow is that it increases the volume of the hole of the damaged region ( $V_{1H} = 35 \text{ mm}^3$  and  $V_{2H} = 8.9 \text{ mm}^3$ ).

Table 7 shows the burn-through irradiation data of an older experiment conducted on the same sample of fused silica without the presence of air and analyzed in Ref [3].

Run Number	Wavelength ( $\mu\text{m}$ )	PRF (MHz)	Average Power (Watts)	Average Intensity ( $\text{kW/cm}^2$ )	Volume of entire damaged region ( $\text{mm}^3$ )	Volume of the hole ( $\text{mm}^3$ )	Penetration Rate (mm/s)
2	4.825	37.4	100	10	92	5.6	0.081

**Table 7. Irradiation Data of Slip-cast Fused Silica Sample #3, After Ref. [3]**

Comparing our irradiation results with those on Table 7, we see that shifting the wavelength from  $\lambda = 4.825 \mu\text{m}$  to  $\lambda = 3.1 \mu\text{m}$  and increasing the average power from 100 Watts to 500 Watts, the penetration rate increases from 0.081 mm/s to 1.32 mm/s with the presence of airflow and to 7.5 mm/s without it. The volume of the entire damaged region increases from  $92 \text{ mm}^3$  to  $100 \text{ mm}^3$  with the presence of airflow and to  $105 \text{ mm}^3$  without



it. Finally the volume of the hole increases from  $5.6 \text{ mm}^3$  to  $35 \text{ mm}^3$  with the presence of airflow and  $8.9 \text{ mm}^3$  without it.

Figure 50 shows a close-up of damage in Run 1 and Figure 51 in Run 2. Figure 52 shows the view of those irradiations on the back face of the sample.

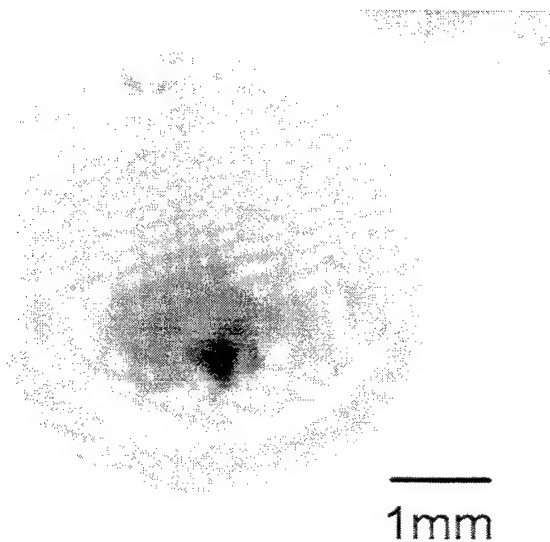


**Figure 50. Close-up of Damage of Slip-cast Fused Silica in Run 1**

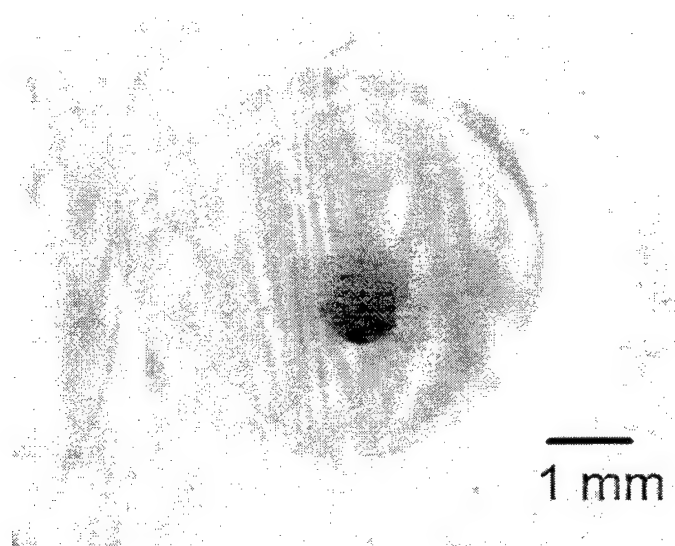


**Figure 51. Close-up of Damage of Slip-cast Fused Silica in Run 2**

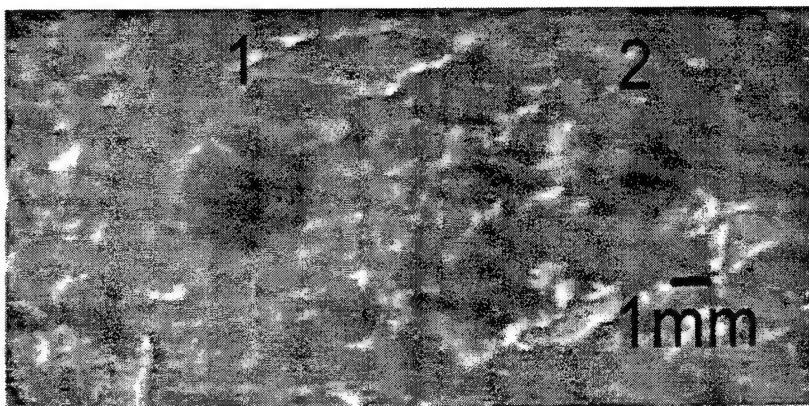


**Figure 52. Damage Back View of Slip-cast Fused Silica in Run 1 and 2**

**THIS PAGE INTENTIONALLY LEFT BLANK**

## VI. CONCLUSIONS

Anti-ship missiles (ASM) constitute a major threat to warships. Advanced technology is used in the missile production, making them variously faster, stealthier, lower flying, less susceptible to countermeasures and more agile in the terminal phase. As a result, a highly sophisticated close in weapon systems (CIWS) is needed. The Phalanx gun is the most widely deployed CIWS. Through a series of Phalanx simulations we showed that it is inadequate; under ideal conditions, the distance where a hard-kill is achieved is too close to the ship. Even though the ship may not be hit by an intact missile, it cannot avoid damage by the missile debris.

High-energy lasers (HEL) might be an answer to the highly sophisticated ASM, and the FEL is a candidate for CIWS. The advantages that it provides are almost instantaneous reaction at the speed of light, a large missile destruction range, rapid re-engagement, a large and renewable magazine, line of sight accuracy, precision aim pointing, high single shot cost-effectiveness, and tunability to specific optimal wavelengths. The tunability is the main advantage over other HELs, because a wavelength can be selected that would give good atmospheric transmission or is appropriate to the specific target absorption characteristics.

The Navy's Directed Energy Office is currently funding TJNAF to study the FEL as a possible ship-defense weapon. The TJNAF FEL is capable of several hundred watts average power and new developments are being made to upgrade to operate 10 kW average power in the near future. This thesis also studied the laser damage produced by

TJNAF FEL on Slip-cast Fused Silica samples; a typical material for missile construction. Using the existing FEL, we estimated the damage from a MW-class weapon by focusing a lower power beam to a smaller spot size. Comparing our experimental results with previous experiments on the same materials, we found that a change in wavelength from  $\lambda = 4.825 \mu\text{m}$  to  $\lambda = 3.10 \mu\text{m}$  and changing the pulse repetition frequency (PRF) from 37.4 MHz to 18.7 MHz gave an improvement in penetration rate of 15.4% without airflow and 25.4% with airflow. In both experiments, the average power was 100Watts focused to an intensity of the irradiation was  $10 \text{ kW/cm}^2$ . Changing the wavelength from  $\lambda = 4.825 \mu\text{m}$  to  $\lambda = 3.10 \mu\text{m}$ , increasing the power from 100 Watts to 500 Watts, and keeping the PRF constant at 37.4 MHz with  $10 \text{ kW/cm}^2$  irradiation intensity, the improvement in the penetration rate was 1530% with the presence of airflow and 9200% without airflow. The volume of total damage increases by 8.7% with the presence of airflow and by 14.1% without it, and the volume of the damage hole is increased by 525% with the presence of airflow and by 59% without it.

In the future, it might be interesting to conduct experiments changing just one parameter in each experiment so that we can better evaluate the effect of each of them. The eventual goal of the damage experiments is to develop scaling rules that will reliably predict the damage from a larger laser without spending enormous amount of money building that laser first.

Experiments using the TJNAF FEL have explored the operation with inversely tapered undulators. In this thesis, we also described the single mode and multimode simulation results, using the TJNAF FEL experimental parameters. Steady-state power,

weak-field steady-state gain, induced electron energy spread, and optical spectrum width behaviors were explored as a function of desynchronism  $d$  and tapering rate  $\delta$ , using FEL pulse evolution simulations including short pulse effects.

For FEL operation driven by the 34.5 MeV energy electron pulses, it was found that even though the maximum power is obtained for  $\delta = 0$ , a negative taper of  $\delta = -4\pi$  provides higher power that is more stable. The maximum power attainable while keeping induced energy spread less than 6% is  $P = 165$  for negative taper of  $\delta = -4\pi$  at  $d = 0.01$ .

For the FEL operation driven by the 47.5 MeV energy electron pulses, it was found that negative tapering with tapering rate  $\delta = -4\pi$  gives the highest power and stability up to  $d = 0.16$ . The maximum power attainable while keeping the induced energy spread less than 6% is  $P = 177$  for  $\delta = -4\pi$  at  $d = 0.0075$ . Keeping  $\Delta\gamma/\gamma$  less than 6% is the requirement for effective recirculation of the electron beam.

**THIS PAGE INTENTIONALLY LEFT BLANK**

## LIST OF REFERENCES

1. Shinn, M. D., personal letter, November 30, 1999.
2. Shinn, M. D., personal letter, May 7, 2000.
3. Thompson, R., "Experimental Damage Studies for a FEL Laser Weapon," Master's Thesis, Naval Postgraduate School, June 1999.
4. Cooper, A.W., and Crittenden, E.C., "Electro-optics Sensors and Systems," Naval Postgraduate School, September 1988.
5. Driggers, R.G., Cox, P., and Edwards, T., "Introduction to Infrared and Electro-optical Systems," Artech House Publishers, 1999.
6. Schriempf, J.T., "Response of Materials to Laser Radiation: A Short Course," Naval Research Laboratory, Washington, DC, July 1974.
7. Colson, W.B., Physics 4911 Course Notes, Naval Postgraduate School, 2000.
8. Colson, W.B., in Laser Handbook , Vol 6, Chapter 5, editors W.B. Colson, C. Pellegrini, and A. Renieri, North-Holland, 1990, pp.134-140.
9. Colson, W.B., in Laser Handbook , Vol 6, Chapter 5, editors W.B. Colson, C. Pellegrini, and A. Renieri, North-Holland, 1990, pp.156-160.
10. Colson, W.B., in Laser Handbook , Vol 6, Chapter 5, editors W.B. Colson, C. Pellegrini, and A. Renieri, North-Holland, 1990, pp.176-180.
11. Colson, W.B., in Laser Handbook , Vol 6, Chapter 5, editors W.B. Colson, C. Pellegrini, and A. Renieri, North-Holland, 1990, pp.168-175.
12. Benson, S., Gubeli, J., and Neil, G. R., "An Experimental Study of an FEL Oscillator with a Linear Taper," TJNAF, Newport News, VA, 2000.



**THIS PAGE INTENTIONALLY LEFT BLANK**

## INITIAL DISTRIBUTION LIST

1. Defense Technical Information Center.....2  
 8275 John J. Kingman Rd., STE 0944  
 Ft. Belvoir, VA 22060-6218
  
2. Dudley Knox Library.....2  
 Naval Postgraduate School  
 411 Dyer Rd.  
 Monterey, CA 93943-5101
  
3. Professor William B. Colson, Code PH/Cw.....2  
 Department of Physics  
 Naval Postgraduate School  
 Monterey, CA 93943-5000
  
4. Professor Robert L. Armstead, Code PH/Ar.....1  
 Department of Physics  
 Naval Postgraduate School  
 Monterey, CA 93943-5000
  
5. Steve Benson.....1  
 TJNAF  
 1200 Jefferson Ave.  
 Newport News, VA 23606
  
6. George Neil.....1  
 TJNAF  
 1200 Jefferson Ave.  
 Newport News, VA 23606
  
7. Michele Shinn.....1  
 TJNAF  
 1200 Jefferson Ave.  
 Newport News, VA 23606
  
8. Lieutenant Adamantios Christodoulou.....3  
 12 Valtetsiou St.  
 Kaminia-Piraeus 18540  
 Greece

9. Engineering & Technology Curricular Office (Code 34).....1  
Naval Postgraduate School  
Monterey, CA 93943-5000